

## **Abstract**

ATWATER, MARK ANDREW. Stabilizing Nanocrystalline Copper and Brass by Solute Addition. (Under the direction of Dr. Carl C. Koch).

Metals commonly show increased strength as the grain size is reduced, and as the grain size reaches nanoscale dimensions the increase can be quite dramatic. With this improvement in strength comes a more insidious side effect: microstructural instability. The same grain size dependent strengthening carries an energy penalty. The large percentage of grain boundaries have an energy associated with them and this energy can be reduced to a more favorable state by grain growth. The driving force for this process is proportional to the boundary energy and area, and in nanocrystalline metals it is quite large. This causes grain growth to occur at temperatures that are only a small fraction of the melting temperature of the metal. If not addressed, this instability at elevated temperature makes a nanocrystalline material unsuitable for service. The basis of this work is that it can be addressed. Indeed, grain growth can be significantly suppressed even at elevated temperatures by judicious addition of minor alloying elements.

To reduce the grain size to this degree requires unique processing. The method used for this study was severe plastic deformation by high-energy ball milling. Not only can the grain size be reduced by this method, but nonequilibrium alloys can be created by mechanical alloying. To study the grain size stabilization of nanocrystalline copper and brass, they were milled in pure form and small additions of other elements were systematically added to determine the effects. The elements chosen were zirconium (Zr), antimony (Sb), and tungsten (W). The

general recipe for stabilizing nanocrystalline metals is to add an element which has a large atomic size difference and low solubility in the parent phase to encourage segregation to the grain boundaries. The purpose it serves toward grain boundary stabilization can be either to reduce the grain boundary energy or mobility. The former is known as the thermodynamic mechanism and the latter is the kinetic mechanism.

Copper and brass both saw an increase in grain size stabilization by the addition of just 1 at% Zr. Copper benefited significantly seeing an increase in growth onset from approximately 300 °C to 1000 °C. Brass proved to be more stable when pure, maintaining a nanoscale grain size to 600 °C, but did so to 800 °C with the Zr addition. Antimony proved to be a poor stabilizer as neither copper nor brass saw any appreciable increase in growth onset temperature. Brass actually proved to be somewhat less stable when Sb was added. This poor performance is attributed to the appreciable solubility of Sb in copper throughout the annealing range. Tungsten was added to copper, but it was difficult to reduce the tungsten particle size even with longer milling times, and this manifested in a very large size distribution of W particles (~10-5000 nm). As W and copper are completely immiscible even as liquids, the W remains as discreet particles and acts in kinetic manner. This method toward stabilization requires particle sizes be appreciably smaller than the grain size, and with such a broad size distribution only a fraction of the W added was reduced to useful dimensions. The stability was extended to 600 °C by adding 10 at % W.

Nanocrystalline materials carry a promise of a new application for current materials and the processing techniques can be used to produce new alloys unattainable through traditional, equilibrium processes. There are still barriers to overcome before utilizing the unique properties these materials possess, however, one of the most foreboding, low temperature grain growth, can be successfully addressed through solute stabilization.

© Copyright 2012 by Mark A. Atwater

All Rights Reserved

Stabilizing Nanocrystalline Copper and Brass by Solute Addition

by  
Mark Andrew Atwater

A dissertation submitted to the Graduate Faculty of  
North Carolina State University  
in partial fulfillment of the  
requirements for the degree of  
Doctor of Philosophy

Materials Science and Engineering

Raleigh, North Carolina

2012

APPROVED BY:

---

Dr. Carl Koch  
Committee Chair

---

Dr. Ronald Scattergood

---

Dr. Donald Brenner

---

Dr. Yuntian Zhu

## ***Dedication***

In loving memory of my brother, Bryan, who taught me more  
about life than these years of education ever could.

## ***Biography***

Mark was born in Warren Pennsylvania to Dennis and Judith Atwater in the fall of 1984. He attended Warren Area High School until earning his diploma in 2003. He continued his education by attending Pennsylvania College of Technology as a Manufacturing Engineering Technology major. He graduated *magna cum laude* with a B.S. in that discipline in the spring of 2007 along with associate degrees in Automated Manufacturing and Toolmaking Technology in addition to certificates in Machinist General and Nanofabrication Manufacturing Technology. He decided to further his education still by attending the University of New Mexico as a Mechanical Engineering major. During this time he married his college sweetheart, Cammie, whom he met in his sophomore year in Pennsylvania. While enrolled as a master's degree student under the direction of Dr. Zayd Leseman, he researched the catalytic formation of carbon nanofibers and methods for generating foam-like macrostructures from these subunits. He graduated with distinction in the fall of 2009 and decided to pursue his growing interest in materials science. This was accomplished by enrolling at North Carolina State University in the spring of 2010 in the Materials Science and Engineering doctorate program. Under the direction of Dr. Carl Koch he worked on stabilizing nanocrystalline copper and brass by adding dilute quantities of solute materials.

## ***Acknowledgements***

There are many people who have helped me during this educational process, and I'm grateful to each one. First, I'd like to thank Dr. Carl Koch for taking me on as a research assistant and funding this work. Also, his expertise and advice were and are greatly appreciated and invaluable to forming this work. Dr. Ron Scattergood was also instrumental in guiding this work. His guidance with the thermodynamic evaluations was especially useful and our conversations were of great benefit. I would like to thank my Committee, also including Dr. Donald Brenner and Dr. Yuntian Zhu, for agreeing to oversee this work and for helping to improve its quality. To all of my professors who have taken the time to help me understand the material and who have painstakingly prepared and presented it, I am deeply indebted. To the other students in the research group and in my classes, thank you for helping me get started and supporting me along the way.

I would also like to acknowledge the help I received from Dr. Tom Rawdanowicz in TEM sample preparation and use, as well as other various other topics on which we spoke. I am grateful to the folks at the Analytical Instrumentation Facility (AIF), specifically Roberto Garcia, Dale Batchelor and Chuck Mooney for assistance with SEM, TEM and FIB work. Also, Roger Russell was instrumental in helping me with laboratory organization and assisting in maintaining a safe and productive work environment.

Important recognition is owed to my family who has encouraged me through the various levels of my schooling and continually checked up on me to “make sure I was still alive.” It has been heartening to know you are behind me. Specifically, I would like to thank Len and Cindy who can only imagine the truly positive impact their support has had on my school work and me. It is difficult to describe the depth of appreciation I have for my wife, Cammie, as she has stood by me through all of the cross-country moves, nights filled with homework and studying, and the continual hope of what someday will be. I hope to utilize all I have gained from this experience and to provide a better future (now that it is time for a “real job!”).

## **Table of Contents**

<b>1</b>	<b>LIST OF TABLES .....</b>	viii
<b>2</b>	<b>LIST OF FIGURES.....</b>	ix
<b>3</b>	<b>INTRODUCTION .....</b>	1
<b>4</b>	<b>LITERATURE REVIEW.....</b>	8
4.1	THE STRENGTH OF NANOCRYSTALLINE MATERIALS.....	9
4.2	PRODUCING NANOCRYSTALLINE MATERIALS .....	12
4.3	STABILIZATION EFFORTS.....	15
4.3.1	<i>Kinetic Stabilization.....</i>	17
4.3.2	<i>Thermodynamic Stabilization.....</i>	20
<b>5</b>	<b>EXPERIMENTAL METHODS.....</b>	30
5.1	MILLING EQUIPMENT AND CONDITIONS .....	31
5.1.1	<i>Cold welding during milling and techniques for alleviation.....</i>	32
5.2	ANNEALING EQUIPMENT AND CONDITIONS.....	36
5.3	CHARACTERIZATION METHODS .....	37
5.3.1	<i>Vickers Microhardness .....</i>	38
5.3.2	<i>X-ray diffraction.....</i>	42
5.3.3	<i>Optical microscopy .....</i>	45
5.3.4	<i>Scanning electron microscopy .....</i>	45
5.3.5	<i>Transmission electron microscopy.....</i>	47
<b>6</b>	<b>STABILIZATION OF COPPER BY ZIRCONIUM .....</b>	51
6.1	INTRODUCTION.....	52
6.2	EXPERIMENTAL DETAILS .....	54
6.3	RESULTS.....	55
6.4	DISCUSSION.....	67
6.5	CONCLUSIONS .....	74
<b>7</b>	<b>STABILIZATION OF BRASS BY ZIRCONIUM .....</b>	76
7.1	INTRODUCTION.....	77
7.2	EXPERIMENTAL .....	78
7.3	RESULTS.....	80
7.4	DISCUSSION.....	87
7.4.1	<i>Pure Brass.....</i>	87
7.4.2	<i>Brass-Zirconium .....</i>	89
7.5	CONCLUSIONS .....	95
<b>8</b>	<b>STABILIZATION OF COPPER &amp; BRASS BY ANTIMONY .....</b>	96
8.1	INTRODUCTION.....	96
8.2	EXPERIMENTAL .....	97
8.3	RESULTS.....	99

8.4	DISCUSSION.....	107
8.5	CONCLUSIONS .....	111
<b>9</b>	<b><i>STABILIZATION OF COPPER BY TUNGSTEN</i></b> .....	<b>113</b>
9.1	INTRODUCTION.....	113
9.2	EXPERIMENTAL .....	115
9.3	RESULTS.....	117
9.4	DISCUSSION.....	129
9.5	CONCLUSIONS .....	132
<b>10</b>	<b><i>CONCLUSIONS</i></b> .....	<b>133</b>
<b>11</b>	<b><i>REFERENCES</i></b> .....	<b>138</b>

## ***List of Tables***

Table 4.1 - Constants used in calculating grain boundary energies.....	69
Table 5.1 - Dark field grain size results for pure brass and 1% Zr alloy (B1Zr CRT) .....	86
Table 5.2 - Material constants used in thermodynamic calculations. Values for brass were a weighted average of Cu and Zn values.....	93
Table 7.1 - W particle size distribution and area fraction from SEM analysis for W particles observable with SEM resolution (the smallest particles not included).....	123

## List of Figures

Figure 2.1 - Hall-Petch relation between grain size and yield stress for Cu.....	11
Figure 2.2 -Influence of global solute content and temperature on (a) segregation energy, (b) equilibrium grain size, and (c) interfacial excess.....	28
Figure 3.1 - SPEX 8000M mixer/mill used for mechanical milling and alloying (image from <a href="http://www.directindustry.com">www.directindustry.com</a> ) .....	32
Figure 3.2 – Equipment preparation for cryomilling.....	35
Figure 4.1 – XRD comparison of the as-milled Cu-Zr alloys.....	56
Figure 4.2 - Cu <sub>1</sub> Zr-C X-ray spectra after annealing for 1 hr at increments of 100 °C .....	57
Figure 4.3 - XRD grain size estimations for Cu-Zr alloys and pure Cu equivalently processed.....	58
Figure 4.4 - Selected area diffraction patterns for the 5% Zr alloys in the as-milled condition a) Cu <sub>5</sub> Zr-RT with intermetallic rings indicated by arrows, b) Cu <sub>5</sub> Zr-C without intermetallic rings. The innermost ring is attributed to ZrO <sub>2</sub> . .....	60
Figure 4.5 - Hardness values for Cu-Zr alloys and pure Cu equivalently processed.....	61
Figure 4.6 - Cu <sub>1</sub> Zr-C in the as-milled condition a) bright field image with SAD pattern inset top-right and (b) corresponding dark field image with volume fraction grain size distribution inset bottom left.....	63
Figure 4.7 - Cu <sub>1</sub> Zr-C annealed for 1 hr at 900°C a) SAD pattern, (b) Bright field image (c) dark field image generated by the 110 and 200 diffraction rings with volume fraction grain size distribution inset bottom left (c) dark field image using innermost rings of SAD pattern shown in (a).....	64
Figure 4.8 - FIB grain size image of Cu <sub>1</sub> Zr-C annealed at 900 °C by ion channeling contrast at magnifications of (a) 40,000X and (b) 80,000X.....	66
Figure 4.9 - Normalized grain boundary energy for (a) varying bulk Zr concentrations ( $X_{Zr} = 0.01,$ $0.02, 0.05$ ) at 273K and (b) for variation in temperature with $X_{Zr} = 0.01$ .....	69
Figure 4.10 - Comparison of normalized grain energies for various alloy systems .....	71
Figure 5.1 – XRD comparisons for pure brass milled in (a) Ar and (b) vacuum. Annealing temperatures are listed in °C, except for the unannealed (as-milled) condition labeled “A-M”...80	
Figure 5.2 - Post annealing XRD spectra of brass with 1% Zr and 5% Zr additions. Annealing temperatures are listed in °C, except for the unannealed (as-milled) condition labeled “A-M”...81	

Figure 5.3 - Comparison of XRD grain size estimates. Cu-Zr data is added from [102]. .....	83
Figure 5.4 – Measured hardness values for the brass and brass-Zr alloys.....	84
Figure 5.5 – B1Zr CRT after annealing for 1 hr at 800 °C (a) SAD pattern with objective aperture positions indicated for inner rings (position 1) and 111 and 200 brass rings (position 2). Bright field image is shown in (b) and dark field images are shown corresponding to (c) objective aperture position 1 and (d) objective aperture position 2 with volume fraction grain size inset lower-left. Scale bar equivalent for bright and dark field images.....	85
Figure 5.6 – TEM results for pure brass milled in Ar and annealed at 600 °C for 1 hr (a) bright field with SAD pattern inset at upper-left and (b) corresponding dark field image with volume fraction grain size inset lower left. Scale bar in bright field image valid for both images.....	86
Figure 5.7 - Comparison of experimental XRD pattern for B5Zr after 800 °C anneal and the calculated pattern for $Zn_3Zr_3O$ . Dashed lines are associated with the calculated pattern peaks. Brass peaks are labeled with corresponding reflections. ....	92
Figure 5.8 - Thermodynamic model of (a) concentration effect of Zr in brass, and (b) brass and Cu with 1 Zr .....	94
Figure 6.1 - XRD spectra for 5% Sb alloys of (a) copper and (b) brass .....	99
Figure 6.2 - XRD grain size estimation using the Scherrer equation for (a) Cu-Sb alloys and (b) brass-Sb alloys.....	100
Figure 6.3 - Optical images of (a) Cu5Sb and (b) B5Sb after being compacted, annealed at 600 °C for 1hr and polished. Arrows indicate a possible second phase between particles. ....	102
Figure 6.4 – Backscattered electron image of B5Sb alloy compacted then annealed at 600 °C for 1 hr with compositional results based on EDS data collected at the points indicated inset top-left. 103	
Figure 6.5 - Hardness values for (a) Cu-Sb alloys and (b) brass-Sb alloys .....	105
Figure 6.6 - TEM images of Cu0.5Sb annealed at 400 °C using (a) bright field with inset SAD pattern, and (b) corresponding dark field with inset grain size histogram.....	106
Figure 6.7 - TEM images of B0.5Sb annealed at 600 °C using (a) bright field with inset SAD pattern, and (b) corresponding dark field with inset grain size histogram.....	107
Figure 7.1 - XRD grain size estimate for various alloys and annealing conditions.....	118
Figure 7.2 – XRD spectra after annealing at labeled annealing temperatures for (a) Cu10W milled for 8 hr and (b) Cu10nW milled for 4 hr. ○ - indicates (with increasing angle) W peaks for 110, 200, 211, and 220 reflections. ● - indicates (with increasing angle) Cu peaks for 111, 200, 220, 311	

and 222 reflections. The insets at the top-right of the images highlight the W 110 and Cu 111 peaks.....	119
Figure 7.3 - Hardness results for annealed Cu-W alloys .....	120
Figure 7.4 - SEM images of as-milled Cu1W milled for (a) 4 hr and (b) 8 hr. EDS maps of (c) W corresponding to the sample milled for 4 hr shown in (a) and (d) W corresponding to the sample milled for 8 hr shown in (b). ....	121
Figure 7.5 - SEM images of as-milled Cu10W 8hr and Cu10nW milled for 4 hr .....	122
Figure 7.6 - Cu10W alloy milled for 8hr and annealed at 600 °C for 1 hr. (a) bright field image with SAD pattern inset top-left (b) dark field image using 111 and 200 Cu rings (c) dark field image using 110 W ring and (d) Cu grain size and W particle size distribution .....	125
Figure 7.7 - Cu10W alloy milled for 8hr and annealed at 800 °C for 1 hr. (a) bright field image with SAD pattern inset top-left (b) dark field image using 111 and 200 Cu rings ring (c) dark field image using 110 W and (d) Cu grain size and W particle size distribution.....	127
Figure 7.8 – TEM images of Cu10W milled for 8 hr and annealed at 600 °C for 1 hr. (a) Arrows indicate some of the tungsten particles (b) magnified view of boxed area in (a) with longitudinal axes of oblong grains labeled with arrows.....	129

# **1 *Introduction***

---

---

A material's properties are directly related to its microstructure. Therefore, one material may behave quite differently when processed in different ways. The processing variables include categories such as physical deformation and thermal treatment. The rate and sequence of processing steps also have a profound impact for the final characteristics. There is a two-fold implication for having a long list of processing variables such as pressure, temperature, atmosphere, duration, rate, etc. The first aspect to consider is the challenge presented. With so many variable details, how well can we expect repeatability? The second aspect is the opportunity presented. With so many variables, how can they be exploited to yield unique results? The area of nanocrystalline material production and characterization is a balance of these two aspects. Severe plastic deformation (SPD), the technique used in this work, can be described as difficult to precisely control, but capable of producing unique, nonequilibrium structures, unattainable by conventional techniques. The many variables encountered in producing novel materials by SPD can be challenging to direct since the processing occurs under extreme conditions with respect to total strain and strain rate. Despite lacking the ability to precisely tailor the process, many steps can be taken to achieve the desired result in a repeatable way.

The nonequilibrium nature of many nanocrystalline structures creates new opportunities but also new obstacles. Being that they are metastable, their natural inclination is toward a stable state that is typically less useful than the as-processed condition. Though a variety of unique structural characteristics may be achieved by nonequilibrium processing (e.g. solid solubility extension, amorphous phases, etc.), the main considerations herein are grain size reduction and the stabilization of a nanoscale grain structure. In the nanocrystalline condition, grain boundary area and the associated energy are much higher than in conventional, coarse-grained materials which leads to useful properties and important considerations during processing and annealing.

The benefit of reducing the grain size in metals is due to an increase in strength and hardness. This behavior is described by the Hall-Petch relation [1, 2] which will be further elaborated on in Section 2.1. The relation does have limited applicability at the smallest grain sizes, but as a generalization, predicts a rise in material strength that is proportional to the inverse square root of the grain size. This produces a very rapid, asymptotic rise in strength as grain size is reduced, and if strictly accurate to the smallest dimensions, would indicate a nearly infinite strength when the grain size is sufficiently reduced. Although the increase in strength can be significant [3-5], the smallest grain sizes deviate from this behavior by reaching a strength plateau or undergoing grain size softening [6, 7].

The methods for producing nanocrystalline materials can vary greatly, but typically involve a large amount permanent deformation, extremely rapid cooling of a material from the liquid

phase, and gas phase condensation among others. The method chosen for this work was high-energy ball milling. A subcategory of SPD, ball milling employs repeated impact of a milling media (balls) with the material being processed (typically powder). The repetitive stress and strain of the impacts causes the grain size to be reduced. The particular method used here involves placing powder(s) and balls into a sealed vial which is rapidly shaken to drive the alloying and/or grain size reduction process. The mill of choice, designed and manufactured by SPEX SamplePrep, is a “shaker” mill which requires less time than similar techniques but with a smaller powder throughput appropriate for alloying screening [8] and not industrial production. The details of the apparatus and milling conditions will be elaborated on in Section 3.1.

Once the powder has been milled and the grain size sufficiently reduced, the microstructure is in a high energy state and therefore prone to return to a more stable, coarse-grained state. In pure form, metals have been found to undergo grain growth at room temperature [9] indicating a serious susceptibility toward grain growth even at low homologous temperatures. To prevent this from occurring, other materials can be added in small quantities (typically < 5 at%) to stabilize the principal material at a small grain size. Ideally, the stabilizer will prevent grain growth without negatively affecting other material properties.

There are two major classifications of stabilization used to mitigate the low-temperature grain growth problem. They are defined by the mechanism responsible for stabilizing the grain structure, and they are known as kinetic stabilization and thermodynamic stabilization.

Though both are intended to stop grain growth from occurring, they achieve that end quite differently. In kinetic stabilization, the mechanism working against grain growth is physical resistance (mobility reduction). The grain boundaries are inhibited from moving, or pinned, by second phase particles that raise the energy needed for movement [10, 11]. In thermodynamic stabilization, the end goal is not to raise the energy needed for gain growth, but to reduce the energy available for it. Instead of acting as a physical barrier, the goal is to make the grains energetically stable so they have no driving force toward growth [12]. Kinetic and thermodynamic stabilization will be treated in detail in Sections 2.3.1 and 2.3.2 respectively.

As these materials are typically in powder form, they are candidates for powder metallurgy techniques in forming useful components. Manufacturing of consolidated, bulk parts will likely involve high temperature and pressures for relatively short times. As the temperature is raised the energy available for grain growth is also increased, and quite significantly. The purpose of stabilization is to yield a useful material after processing that retains the superior strength attained in the milling step. For this reason, thermal stability must be verified at various temperatures, including those quite near the melting point. The driving force for growth may increase sufficiently with temperature to destabilize a microstructure which is stable at lower temperatures. Stability must be regarded with respect to the maximum processing or service temperature, and the material must be kept below the upper stability boundary for reliability purposes.

The research effort reported herein was conducted to determine the efficacy of stabilizing nanocrystalline copper and brass (copper 30 at% zinc). These materials are widely used and can benefit greatly from an increase in strength by grain size reduction. To stabilize these materials zirconium (Zr), antimony (Sb), and tungsten (W) were added in concentrations up to 10 at%. The stability was tested by annealing the samples at various temperatures. To determine the success of the stabilizer, the hardness of the annealed specimens were obtained since this is indicative of the grain size, especially in the as-milled condition. The grain size was estimated using X-ray diffractometry (XRD) and application of the Scherrer formula [13]. Though this is a good estimate at very small grain sizes (< 30 nm), it is less reliable as grain size increases. For this reason among others, it is imperative to verify the grain size by a more precise method. Transmission electron microscopy (TEM) was used to image the materials for purposes of determining the grain size as well as to detect the presence and distribution of a second phase. Scanning electron microscopy was used to check for porosity, verify atomic concentrations, and examine second phase distribution.

Part of the objective of this work was to determine the effect of processing conditions. Alloys were generated at room temperature and at cryogenic temperature (77 K). Also, they were milled in an argon atmosphere and in an evacuated atmosphere. Multi-step milling, where cryogenic and room temperature milling were combined, was also used. The specifics of these methods and the alloy systems for which they were used are discussed in Chapter 0. In general, it was found that stability was similar for the various processing conditions, though there are certain benefits and disadvantages for each setup.

When copper was alloyed with zirconium (Chapter 4), the grain size was found to be stable up to 900 °C. Though there was a second phase present, it is not thought to be sufficient to account for such remarkable stability. When pure brass and brass alloyed with zirconium (Chapter 5) were annealed, stability of the grain size was maintained to 800 °C which is similar to the copper-zirconium in terms of homologous temperature. A surprising feature of this particular study was that pure brass was found to be stable up to 600 °C, and the zirconium addition was only really useful at 800 °C. Antimony was also added to copper and brass (Chapter 6), but the addition was not nearly as effective at stabilizing grain size during annealing as zirconium. Copper only benefited slightly and required a higher concentration while brass alloyed with antimony actually saw a reduction in grain stability. Finally, copper was alloyed with tungsten (Chapter 7) to form a nanocomposite material. This “alloy” improved grain size retention during annealing, but only to 600 °C, and then only when tungsten was added in a much larger quantity than the other stabilizers. The cause for this is attributed to the dominance of kinetic stabilization in the system.

For nanocrystalline metals to deliver the potential benefits they pose, there must be a practical method of generating and processing them. The metastable state inherent in nonequilibrium processing requires attention so that there is not a deterioration of properties during manufacturing or worse yet, while the material is in service. The topic of stabilizing these unique structures is vital to bringing the technology from the laboratory to the production line. We’ll now turn our attention to the current state of the art in producing and

stabilizing nanocrystalline metals, especially with regard to ball milling and Cu-based systems.

## **2 Literature Review**

---

---

Nanomaterials are not new. Instead, it is a working knowledge of them that is a fairly recent advance in science and engineering [14]. A common example of the historical use of nanostructured materials is the incorporation of gold and silver nanoparticles into glass for creating stained glass of various colors [15]. Although it is now known that the size of the gold nanoparticles changes their color at sufficiently small dimensions, those adept in the trade a century ago were most certainly unaware of the fact. Though they could control the properties, the ability was based on macroscale influence and skill, not bottom-up processing approaches.

“Nanomaterial” is a very generic term but typically refers to a material with some feature with at least one dimension less than 100 nm. Though narrowed slightly, the definition still encompasses a very broad spectrum. For the purpose of this work, isolated nanostructures such as nanoparticles, carbon nanotubes, etc. will be neglected. In fact, the materials generated by the methods to be discussed are generally distinctly visible and capable of being manipulated without the aid of sophisticated equipment. The “bulk” materials are not nanoscale, but the subunits of their constitution are, and hence by this specification they are rightly termed nanomaterials, and more exactly, nanocrystalline materials.

The following literature review will be not be limited in scope to works relating to the stabilization of nanocrystalline (nc) materials, but is extended slightly to encompass some supporting information on properties and processing. However, these deviations from the topic of stabilization will be kept minor. The review will begin with a brief overview of the properties of nc materials in contrast to conventional materials (Section 2.1). After considering these motivations for pursuing the study of nanocrystalline materials, we will progress to how they may be created, with specific attention given to high-energy ball milling (Section 2.2). Finally, the focus will shift to the stabilization of these materials in nc form (Section 2.3).

## 2.1 The Strength of Nanocrystalline Materials

Nanocrystalline materials are crystalline by essence that they possess three-dimensional, long-range, periodic order which defines crystallinity [16]. However, the individual crystals are very small. The crystals are also known as crystallites, but herein will be referred to as grains. “Solid” materials commonly encountered (e.g. wrench, knife, paperclip, etc.) are not made of one crystal but many connected crystals. For this reason they receive the categorical title of being polycrystalline. Even though the grains may be quite small (e.g. 20 nm), the concept of long-range, periodic order is not nullified by such small dimensions since the constituent atoms are much smaller still.

The utility of nanocrystalline materials, especially metals, is the relationship between grain size and strength. A single material can have vastly different properties as the grain size is reduced. This behavior is can be described by the Hall-Petch equation [1, 2, 7, 17, 18],

$$\sigma = \sigma_o + \frac{k}{\sqrt{d}} \quad (2.1)$$

where  $\sigma$  is the yield stress,  $\sigma_o$  is the lattice friction stress,  $k$  is the Hall-Petch (hardening) constant, and  $d$  is the average grain diameter. As a means of visualizing the effect this has on yield stress (strength), the equation is plotted in Figure 2.1 with known values for copper (i.e.  $\sigma_o = 25.5 \text{ MPa}/\sqrt{\text{m}}$ ;  $k = 0.11 \text{ MPa}$  [19]). It is clear that the grain size becomes much more influential on strength in the nanocrystalline range (i.e.  $< 100 \text{ nm}$ ). The logarithmic scale on the abscissa reveals that the increase in yield stress is two times larger for a change in grain size from 100 nm to 10 nm than from 100,000 nm (100  $\mu\text{m}$ ) to 100 nm. For this reason, nanocrystalline materials generate quite a bit of interest.

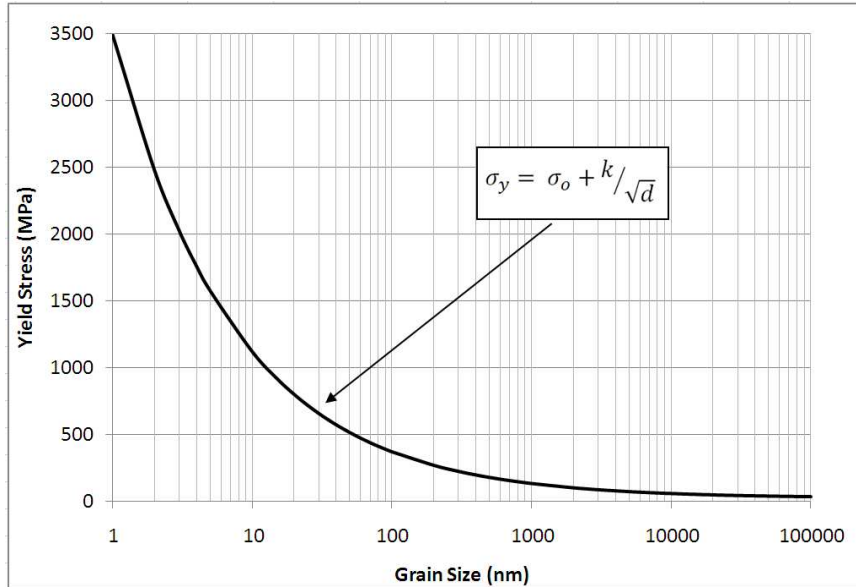


**Figure 2.1 - Hall-Petch relation between grain size and yield stress for Cu**

The Hall-Petch relation indicates extraordinarily high strength at small grain size. The question beckons, “Can we *realistically* expect this prediction to be accurate?” The answer comes as a confident, “No.” Although generally quite good, the Hall-Petch relation breaks down at very small grain sizes. The hardening mechanisms responsible for the increase in strength are typically attributed to dislocation motion [7], but simulations have found limited dislocation activity below 10 nm grain sizes [6]. This indicates the mechanism for deformation has changed. The cause for this is commonly attributed to mechanisms such as grain boundary sliding [20] which has been found by simulation in nc Cu [6, 21] or dislocation interaction with grain boundaries [22, 23].

Because of their small grain size, nanocrystalline materials show a variety of unique mechanical properties [24]. Copper has been found to possess a greatly enhanced strength in nanocrystalline form [3-5]. In alloys, strengthening may also arise from solute effects which are contained in solid solution [25] or which have segregated to grain boundaries [26]. Another important consideration for both strength and stabilization purposes is intermetallic inclusion which can raise the strength [27] and increase the grain size stability [12].

## 2.2 Producing Nanocrystalline Materials

Having established the significant effect grain size reduction has on strength, we can look more closely at the methods for generating such microstructures. Nanocrystalline metals can be generated by deposition (generating nanocrystalline material from the bottom up) or deformation processes (reducing the grain size of pre-existing materials). Deposition processes include techniques such as inert gas condensation [28] and electrolytic deposition [29], and deformation processes include techniques such as ball milling [8, 30] and high-pressure torsion (HPT) [31, 32]. As high-energy ball milling was the single method by which nanocrystalline materials were made in this work, the processing discussion will be focused there. There are many considerations to make when using the ball milling method. These include [8]:

- type of mill
- milling container
- milling speed
- milling time
- type, size, and size distribution of the grinding medium
- ball-to-powder weight ratio
- extent of filling the vial
- milling atmosphere
- process control agent
- temperature of milling

The length of this list quickly indicates that there must be a detailed procedure in place for results to be repeatable. The mill type used here was a SPEX 8000M shaker mill which is a high-energy mill. Other, lower-energy mills can achieve the same or similar results, but depending on their ability to transfer energy to the powder (impact energy and rate), it may take an order of magnitude longer. The SPEX-type mills run at a high speed (approximately 20 Hz [33]) with efficient energy transfer, so processing can take as little as a few hours

depending on the material/material system and the result desired. The energy transfer is determined in large part by the ball-to-powder ratio which is typically specified by mass. This is balanced by the volume of the balls and powder in regard to the volume of the vial. If there is too much powder, or too many balls, the kinetic energy is limited. By allowing for a longer mean free path and higher ball-to-powder ratio, the energy transfer will be more efficient, but the powder output will be lower.

The temperature affects the result greatly as lower temperatures have been found to quicken grain size reduction [34] and increase amorphization [35]. In this work, milling at room temperature tended to results in cold welding of the metal(s) to the vial and balls. To reduce this occurrence two methods were employed: addition of a process control agent (PCA) and milling at cryogenic temperature. Similar results could be obtained by adding 1 wt% sodium chloride or by milling at liquid nitrogen temperature (77 K). By using liquid nitrogen cooling the cold welding could be eliminated and the spurious effects of adding a PCA material could be eliminated. The results for the two conditions were similar, but the processing time was reduced from 8 hr in the room temperature case, to only 4 hr when using a cryogenic milling temperature (see Chapter 4).

Contamination is important to consider when processing a material by high-energy ball milling. All materials were stored and loaded in an argon environment to prevent oxidation. The vials and balls (both 440 stainless steel) were polished and cleaned with ethanol. The milling process not only works the powder mechanically, but the balls and vial interior are

also subject to large impact energies. Due to this there is inevitably a level of contamination from the milling equipment. The amount of contamination increases when milling for longer times [36] and when using a PCA as it becomes incorporated into the alloy [37, 38]. For this reason, short (4hr) PCA-free milling under an argon atmosphere was chosen for milling. The use of cryogenic processing to eliminate the need for a PCA did have a side-effect of metal foam formation. Perhaps a less common form of contamination, when milling in argon at liquid nitrogen temperature metal foam formation on annealing has been encountered [39] and was a constant consideration here. This argon entrapment manifested itself most clearly in the antimony-stabilized materials (Chapter 6).

### 2.3 Stabilization Efforts

Nanocrystalline metals are inherently unstable because of excess system energy that can be reduced through grain growth. The change in Gibbs free energy,  $G$ , with respect to the grain boundary area,  $A$ , is proportional to the grain boundary energy,  $\gamma$ , as shown in equation 2.2 [40]:

$$dG \propto \gamma dA \quad (2.2)$$

As the grain size decreases, the grain boundary area increases. This increase becomes quite significant at very small grain sizes where the boundary (surface) area to volume ratio rises

rapidly. This is analogous to the behavior indicated by the Hall-Petch relation (see Figure 2.1). This free energy is thermodynamically unfavorable and provides a driving force for grain growth.

The two principal manners in which the grain size instability can be addressed are kinetic stabilization and thermodynamic stabilization. The goal of these methods is to reduce the grain boundary mobility or energy respectively. Following the development of these concepts by Humphreys and Hatherly [41], grain growth proceeds by the motion of grain boundaries which have a velocity,  $v$ , described by:

$$v = MP \quad (2.3)$$

where the pressure,  $P$ , exerted by the grain is related to the velocity by a constant of proportionality,  $M$ , which is the mobility. The pressure on a grain boundary due to the radius of curvature,  $R$ , is given by:

$$P = \frac{2\gamma}{R} \quad (2.4)$$

The radius of curvature decreases with decreasing grain size so that when nanocrystalline, there exists a substantial pressure for expansion by grain growth. The concept of stabilization requires a zero velocity state which, by Equation 2.2, necessitates eliminating the pressure or

mobility while keeping  $R$  constant. This is where the two stabilization techniques differ. The kinetic route seeks to decrease mobility and the thermodynamic route seeks to decrease pressure by reducing the surface energy (driving force). The mobility has an Arrhenius temperature dependence:

$$M = M_o \left( -\frac{Q}{RT} \right) \quad (2.5)$$

where  $M_o$  is a pre-exponential constant,  $Q$  is the activation energy for growth,  $R$  is the ideal gas constant, and  $T$  is the absolute temperature. Because of this mobility relation, at high temperature kinetic means of stabilization will eventually be overcome [42]. We can now move on to look at some further considerations in each of the stabilization methods. In this a small sampling of the systems that have been studied and their results will be presented. Though the discussion will stay centered on copper and brass, pertinent deviations will be discussed as warranted.

### 2.3.1 Kinetic Stabilization

As stated, the kinetic mechanism to grain size stabilization involves reducing mobility. There are multiple ways to achieve this such as solute drag, porosity pinning, chemical ordering, and second phase (Zener) pinning [12]. The most influential here are solute drag and Zener pinning. In the case of solute drag, solutes can have a significant effect

on the mobility, lowering it substantially when in high concentration near grain boundaries [41]. Not only the amount of solute, but also the type of solute is important. At high boundary velocity faster diffusing solutes produce a greater drag whereas for slow moving boundaries the opposite is true [43]. The amount of solute should not be considered uniform in nanocrystalline systems. Being that many of the alloy systems employ dilute quantities of a strongly segregating solute, the boundaries are expected to be enriched and the grain boundary concentration will be greater than the bulk concentration. Where impurities are attracted to the boundaries, the mobility is decreased [44]. Solute drag has been modeled for a Pd81Zr19 alloy [45], and reported grain growth stagnation as the grain size and grain boundary concentration of Zr increased. In other work by the group the mechanism of stability was identified to be thermodynamic in nature [46]. The appreciable solubility of Zr in [47] as well as thermodynamic factors such as the elastic strain caused by the Zr and the chemical interactions between the Pd and Zr makes strong segregation of the solute less favorable than other systems. As determined in later work [48], even with segregation the reduction in boundary energy was both theoretically and experimentally determined to be insufficient to stabilize the grain size.

As for Zener pinning, the solute in this case is not uniformly distributed as a solid solution, but rather present as a distinct second phase. The second phase may be a precipitate or a composite material which has been forced into the matrix. Second phase pinning is less temperature sensitive than solute drag [49], but is highly dependent on particle size and distribution [10]. The general equation describing the effect is [12]:

$$P_z = \frac{3F\gamma}{2r} \quad (2.6)$$

where  $P_z$  is the pinning pressure exerted by a volume fraction,  $F$ , of particles with diameter,  $r$ , on a boundary with specific energy,  $\gamma$ . This form assumes spherical particles. It is quickly realized that increasing the volume fraction and reducing the particle size will improve the stabilization capability. As in Equation 2.4, there is a direct dependence of pressure on size. Very small grains will exert a large pressure for growth which can only be sufficiently resisted by a distribution of smaller particles (assuming a dilute solution of second phase). The limiting grain diameter,  $D$ , can be expressed as [50]:

$$D = \frac{4r\alpha}{3F} \quad (2.7)$$

where  $\alpha$  is a constant approximately equal to 1. Here we see again that the volume fraction and particle size are very important. The minimum stable grain size has an inverse dependence on the volume fraction and a proportional dependence on the particle size. The closer the particle is to the grain size, the higher the volume fraction must be to stabilize it.

This technique has been employed in a variety of systems, but with regard to nanocrystalline stabilization, especially that of copper, there has been work using Mo [51], Nb [51-53], and W [53, 54]. Though the particles are very effective at stabilizing the Cu when only a few

nanometers in size, coarsening or dissolution at elevated temperature leads to a precipitous decline in stability [11]. This is controlled by solubility in the matrix and the diffusivity at high temperature which will both degrade the grain thermal stabilization. This coarsening has been addressed in an interesting manner in [53]. Though 10% Nb in Cu coarsened significantly at 600 °C and above, by using a mixture of Nb and W (9.5% and 1.5% respectively) the precipitates resisted coarsening more effectively, and at higher temperatures they actually underwent inverse coarsening. This behavior was attributed to kinetic competition between Nb and W precipitation which leads first to the formation of metastable Nb-rich precipitates, until the mobility of W atoms becomes sufficient for a second population of precipitates to form, leading to an inverse coarsening of the Nb-rich precipitates by diffusion to the W precipitates. It is important to note that the method of preparation used in the study was sputter deposition which is capable of generating atomic dispersions of insoluble materials not practical even in high-energy ball milling which is addressed in the Cu-W work here (see Chapter 7).

### 2.3.2 Thermodynamic Stabilization

Now we consider stabilizing nanocrystalline structures by a thermodynamic means. This method employs grain boundary energy reduction as the means to reduce or eliminate grain boundary mobility. The addition of a solute with a strong tendency to segregate to grain boundaries acts to reduce the energy [42, 55]. To work well, the solute should have a large atomic size difference which drives segregation to the grain boundaries where it can be

effective at stabilizing the grain size. The change in surface energy by solute segregation can be described by the Gibbs adsorption isotherm [56]:

$$d\gamma = -\Gamma_A d\mu_A \quad \text{or} \quad \left. \frac{d\gamma}{d\mu_A} \right|_{n_B, T, a} = -\Gamma_A \quad (2.8)$$

where the change in surface energy with respect to the chemical potential,  $\mu_A$ , of the solute atoms ( $A$ ) in the solvent atoms ( $B$ ) at constant number,  $n_B$ , temperature,  $T$ , and surface area,  $a$ . The term  $-\Gamma_A$  is the excess amount of solute atoms at the boundary. The grain boundary energy can be calculated by solving the Gibbs adsorption equation in the dilute limit [57, 58]:

$$\gamma = \gamma_o + \Gamma_s [\Delta H_{seg} - T\Delta S_{seg}] \quad (2.9)$$

where  $\gamma_o$  is the grain boundary energy of an ideal solid solution,  $\Gamma_s$  is the specific solute excess at the interface,  $T$  is the absolute temperature, and  $\Delta H_{seg}$  and  $\Delta S_{seg}$  are the enthalpy and entropy of solute segregation respectively.  $\Delta H_{seg}$  consists of chemical ( $\Delta H_{chem}$  as described by Defay [59]) and elastic ( $\Delta H_{el}$  as described by McLean [60]) terms which were combined by Wynblatt and Ku in accounting for surface segregation [61, 62]. The enthalpy of segregation is then given in the original Wynblatt-Ku model [61] as  $\Delta H_{seg} = \Delta H_{chem} + \Delta H_{el}$  where the chemical contribution is given by:

$$\Delta H_{chem} = (\gamma_B - \gamma_A)\sigma + 2\omega [z_{in}(X_A^b - X_A^s) + z_{out}(X_A^b - \frac{1}{2})] \quad (2.10)$$

where  $\gamma_A$  and  $\gamma_B$  are the surface energies for the solvent and solute respectively,  $X_A^b$  and  $X_A^s$  are the atom fraction segregant of solvent in the bulk and interface respectively,  $\sigma$  is the surface area per mole,  $\omega$  is the regular solution parameter,  $z_{in}$  and  $z_{out}$  are the in-plane and half of the out-of-plane bonds of an atom in the surface plane. The regular solution parameter is given by:

$$\omega = \varepsilon_{AB} - \frac{1}{2}(\varepsilon_{AA} - \varepsilon_{BB}) = \frac{\Delta H_m}{ZX_A^b X_B^b} \quad (2.11)$$

where the bond energies between atoms of the solvent, A, and the solute, B, are given by the corresponding  $\varepsilon$  values,  $\Delta H_m$  is the enthalpy of mixing and Z is the coordination number. The elastic enthalpy is [63]:

$$\Delta H_{el} = -\Delta E_{el} = -\frac{2K_B G_A (V_B - V_A)^2}{3K_B V_A + 4G_A V_B} \quad (2.12)$$

where  $\Delta E_{el}$  is the change in elastic energy,  $K$  is the bulk modulus,  $G$  is the shear modulus, and  $V$  is the molar volume.

### 2.3.2.1 Modified Wynblatt-Ku Model

This approach was later modified to better account for grain boundary segregation where some bonding across the boundary exists [64]. This modified formula, which includes entropy effects, is:

$$\Delta G_{seg} = (\gamma_A - \gamma_B)(1 - \alpha)\sigma - \frac{8\Delta H_m}{Z} \left[ z_{in} \left( X_A^s - X_A^b \right) - z_{out} \left[ \left( X_A^b - \frac{1}{2} \right) - \alpha \left( X_A^s - \frac{1}{2} \right) \right] \right] + \Delta H_{el} - RT \ln \left[ \frac{X_A^b (1 - X_A^s)}{X_A^s (1 - X_A^b)} \right] \quad (2.13)$$

where  $\alpha = 5/6$  to account for cross-boundary bonding,  $X_A^s$  now represents a grain boundary concentration rather than a free surface, and  $\Delta H_m$  is more specifically the enthalpy of mixing of an equimolar liquid of A and B. The bonding terms are  $z_{in} = 6$  and  $z_{out} = 3$  for a face-centered cubic material and the coordination number is related by  $Z = z_{in} + 2z_{out}$ . The last term in Equation 2.13 is the entropy of segregation which can be represented by  $\Delta S_{seg}$ . Given that  $\Delta G_{seg} = \Delta H_{seg} - T\Delta S_{seg}$ , rearrangement of Equation 2.9 gives the normalized grain boundary energy as:

$$\frac{\gamma}{\gamma_o} = 1 + \Gamma_s \frac{\Delta G_{seg}}{\gamma_o} \quad (2.14)$$

where the grain boundary surface excess for the bilayer model is given by  $\Gamma_s = 2(X_A^s - X_A^b)/\sigma$ . Detailed numerical results for the grain size as a function of temperature and total

solute content,  $X_A^\circ$ , require combining Equations 2.9 and 2.13 with a mass balance equation for A. This level of detail is beyond the scope of the current work here, but is treated fully in [64]. Instead the limit of infinite grain size is used where  $X_A^b = X_A^\circ$ . If the plot of  $\gamma/\gamma_0$  vs.  $\Gamma_s$  intersects the  $\gamma/\gamma_0 = 0$  axis in this limit, thermodynamic stabilization is possible for the  $X_A^\circ$  and  $T$  values assumed. We could have also used a plot of  $\gamma/\gamma_0$  vs.  $X_A^s$  in this same context. A benefit of this model is that it only requires values which are readily available in the literature.

This treatment was applied to Fe-based systems by Darling et al. [65-67] where experimental work found Zr and Ta to work well in stabilizing nanocrystalline Fe. Ni and Cr were found to provide little to no improvement. Calculated stabilizations indicated that alloys of Fe with Ni or Cr would be unstable due to poor segregation and that Ta and Zr would be effective. Further, the calculated curves matched the relative stability of the four alloys. As mentioned in the discussion of kinetic stabilization, Pd-Zr alloys were also analyzed in this way [48]. The earlier work of Krill et al. [46] asserted that stability in the system was due to thermodynamic stabilization based on elastic contributions, but neglected the chemical effects which are substantial. Also, the grain size in the earlier work was determined solely by XRD which can be misleading, and when the work was done with more thorough microscopy, the grain size was found to increase to a larger extent and at a lower temperature [48].

### 2.3.2.2 Kirchheim's Model

A model by Kirchheim [56, 68, 69] and Liu and Kirchheim [42, 55] was developed for describing the effects of grain boundary segregation. In [68], Weissmuller's work [57, 58] is extended to establish the equilibrium area of grain boundaries and its temperature dependence. In this, the total energy is described by Equation 2.2 where  $dG = \gamma dA$  so that the total change in energy is related to the grain boundary energy and its associated area. For  $\gamma > 0$ , and decrease in  $dA$  will lower the free energy (i.e. grain growth is favorable). This grain growth is counteracted by the energy required for dissolution of the excess solute (Equation 2.8) into the grain interior. The equilibrium grain size can be calculated as [42]:

$$D = \frac{3\Gamma_s^* V_{AB}}{X_A^o} \quad (2.15)$$

where  $\Gamma_s^*$  is the solute excess equivalent of a saturated grain boundary monolayer and  $V_{AB}$  is the molar volume of the alloy. From this relation it can be seen that as the solute content increases the equilibrium grain size decreases. For a supersaturated grain boundary there is competition between segregation as excess concentration and precipitation into solute-rich particles. When an empirical relation for strongly segregating solutes is used as in [68], it was found that precipitation will ultimately lead to a lower energy state and be the favorable configuration unless kinetically hindered.

The temperature dependence of kinetic methods will lead to a loss of stability not problematic in thermodynamic routes because the grain boundary energy is only weakly dependent on temperature [42, 55]. Grain boundaries can be considered defects along with dislocation lines and vacancies [56], and the formation energy reduction by solute segregation was investigated in [56, 69]. The formation energy has been calculated to reduce to zero or even to become negative, such as in [70]. A defect energy of zero indicates the defect is in equilibrium while a negative energy indicates the number of defects will increase as long as supplied with solute. It was of particular interest to determine the validity of negative defect energies, and it was concluded that negative defect energy would not lead to an unlimited number defects. This is because solute atoms from the grain interior segregate at the freshly produced grain boundary (defect) area and, therefore, the local concentration within the grain (chemical potential) is decreased which produces an associated increase in boundary (defect) energy [56]. This defect energy reduction may be a mechanism for amorphization by ball milling, and has interesting implications for mechanical properties and diffusivity as the solute causes softening by reducing dislocation line energy reduction and enhances diffusion by lowering vacancy formation energy, however, this is balanced by the mobility reduction from the solute concentration [69].

#### **2.3.2.3 Trelewicz and Schuh's Model**

The model developed by Trelewicz and Schuh [40] allows for independent calculation of the energy state of the grain boundary and interior for binary systems. This statistical

thermodynamic model predicts an equilibrium grain size which involves segregation of the solute to grain boundaries as predicted in the above analysis. This treatment allows for the investigation of weakly segregating systems and those away from the dilute limit where solute interaction occurs. To do this, atomic bonding is divided into bulk, transitional, and boundary regions where the bonding distributions are determined by normalizing the volumetric density of atoms in each region by the total number of atoms in the system. Because of the generality of the analysis, the equations include numerous terms to describe the free energy and equilibrium condition, however, when simplifying assumptions are made such as for a dilute system with strong segregation tendency, the boundary energy reduces to that in Equation 2.9.

The equilibrium state is found to be unique in terms of grain size and global concentration. This means that for a given solute content there is only one equilibrium grain size and for any grain size there is one energy-minimizing concentration. The stable, equilibrium condition is where the free energy is minimized, so a boundary with excess segregation sites (“under-full”) or excess segregated solute (“over-full”) is unstable. As the solute content is increased, the equilibrium grain size follows a power-law-like decay (see Figure 2.2b). As temperature is increased, the amount of solute required to stabilize the grain size increases (Figure 2.2b) while at the same time the segregation energy decreases (Figure 2.2a) as does the interfacial excess (Figure 2.2c). The temperature effect is coupled dominantly to the entropy where it serves to randomize the solute distribution effectively desegregating the system.

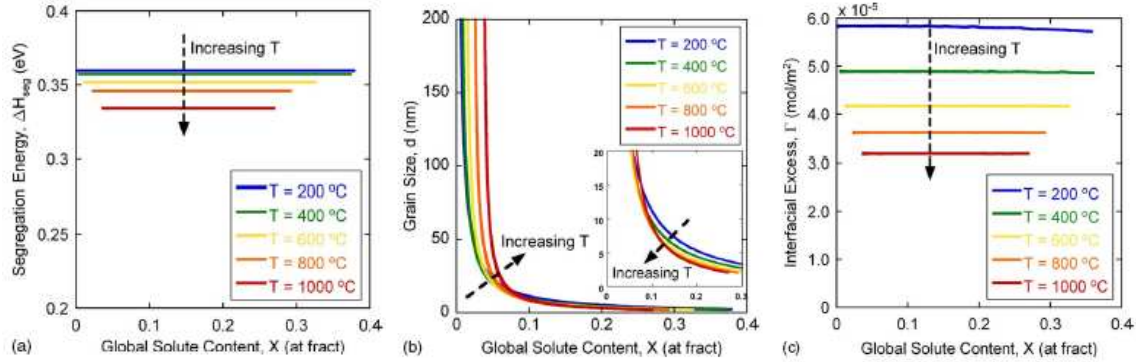


**Figure 2.2 -Influence of global solute content and temperature on (a) segregation energy, (b) equilibrium grain size, and (c) interfacial excess**

Similar to Figure 2.2, the trends for other variations in the state variables were investigated. As the bulk interaction energy increases (higher heat of mixing) the global solute concentration required for the same equilibrium grain size decreases. The interfacial excess drops more quickly with an increase in the solute concentration as bonding with like neighbors becomes more probable and the large heat of mixing indicates it is also favorable. Also, as the solvent grain boundary energy increases, more solute is required to drive the boundary to equilibrium, so the interfacial excess increases as does the segregation energy. The segregation energy is large in systems where the bulk interaction energy is large, the intergranular interaction energy is low, and the solvent grain boundary energy is low. This set of guidelines describes a solute which is energetically unfavorable to maintain in solution and which releases energy upon segregation to the boundary. This is commonly achieved in solutes with an appreciable size misfit and large heat of mixing.

There is much more in the way of theoretical developments of thermodynamic stabilization, but this work will adhere to the treatment above. Segregation is reviewed in [62] and the effect on boundary energy can be found in references such as [12, 26, 40, 42, 46, 55-58, 61, 62, 64, 71-75] if a more detailed treatment is desired. The stabilization mechanisms will be treated more specifically in each of the chapters presenting results and discussion, and the related systems will be described in context. There is interplay of kinetic and thermodynamic mechanisms, especially where the solute forms intermetallics with the solvent or if susceptible to oxide formation. For this reason, it can be difficult to separate the effects of the two, but generally the kinetic effects are expected to be less effective, especially at high temperature [71, 73].

### **3 *Experimental Methods***

---

---

The preparation of the alloys researched here was accomplished by mechanical alloying. High-energy ball milling (Section 3.1) was the vehicle by which this was done. All alloys were created from elemental powders, the purities of which are elaborated on in the results and discussion of the related materials (Chapters 4-7). The thermal behavior of the materials was assessed by annealing them over a range of temperatures (Section 3.2). To determine the properties of the processed materials, characterization was accomplished by hardness testing for mechanical properties (Section 3.3.1), X-ray diffraction (XRD) to analyze phases and estimate grain size (Section 3.3.2), and microscopy to determine composition, grain size, and porosity (Sections 3.3.3-3.3.5). Though general procedures will be outlined here, the specific application of these techniques will be detailed in the chapters pertaining to the individual alloy systems. All alloys were prepared, milled, and stored in an argon atmosphere (typically < 1 ppm O<sub>2</sub>) using a glove box. One exception to this was a bass alloy milled under vacuum which is discussed in Chapter 5.

### **3.1 Milling equipment and conditions**

High-energy ball milling was employed using SPEX 8000M shaker-type mills (see Figure 3.1). The mill operates at a rate of 1060 cycles/minute and is capable of grinding up to 10 g of powder at a time. Two configurations of the mill were used: one at room temperature, the other at cryogenic temperature. The mill used at room temperature was modified for additional cooling by adding a high-capacity fan (~200 ft<sup>3</sup>/min) located at the top of the mill. This was the only performance modification made to the equipment. It is of importance to note that this additional cooling will affect the results for very ductile materials which cold weld to the vial and balls if the temperature increases sufficiently. It has been found that internal temperature increase during milling can be significant [38], but the motor itself is a major heat source in the casing during processing, though the bearings of the clamp arm also become warm. The temperature of the vial was found to reach a constant value of ~30 °C within 2 hr of starting the process. As copper and brass are both rather ductile, the majority of processing required the use of the cryogenic mill (cryomill) to keep cold welding to a minimum.



Figure 3.1 - SPEX 8000M mixer/mill used for mechanical milling and alloying (image from [www.directindustry.com](http://www.directindustry.com))

### 3.1.1 Cold welding during milling and techniques for alleviation

#### 3.1.1.1 Milling vial and ball preparation

When milled at room temperature, copper cold welded to the vial reducing the overall yield.

The 440 stainless steel vial was repolished and the experiment redone, but cold welding then accumulated on the ball bearings. This result indicates the importance of the vial condition during milling, especially in regard to the surface roughness. The vial was extensively polished by proceeding from coarse to fine grit sandpapers (280 → 320 → 400 → 600 →

1200 grit) using water during the process. The final polish was accomplished using 1 µm alumina powder suspended in water leaving a mirror finish. The balls used were grade 25, 440 stainless steel which are mirror-polished from the manufacturer (Salem Specialty Ball Inc.) so any sticking to the balls was not attributable to surface condition. The vial and balls were rinsed and wiped down with 200-proof ethyl alcohol (ethanol) before first use. Having a thoroughly polished surface alleviated sticking to the vial greatly, but did not totally eliminate it at room temperature. When possible, if the alloy left only a minor residue on the vials and/or balls, these were reused for the same alloy so as to reduce contamination. Typically, an acceptable level could be described as leaving only a tint to the vial and/or balls and still retained the “mirror” appearance otherwise. The vial and balls were never exposed to ambient atmosphere if they were to be reused. The vial was always opened and kept in an argon environment until polished or reused. This reuse was more readily accomplished for alloys than for the pure copper as previous cold welding promoted further cold welding in later runs, and the old material could be incorporated into newer material leading to inhomogeneities.

### ***3.1.1.2 Process control agents***

Because sticking was extensive even after careful vial preparation, the addition of a process control agent was adopted. Sodium chloride (NaCl) was chosen to reduce the cold welding, and when added in quantities as low as 0.125 wt% was effective at eliminating the problem. Such small additions resulted in large agglomerated spheres of copper, and to produce a

coarse powder more NaCl was added. It required 1 wt% of NaCl to generate powder, but this large addition came with consequences. The powders produced using the NaCl had a profound corrosion response when left in ambient air. In less than 1 hr the powder was found to turn dark purple, but powders produced without the NaCl had no such change. The effect was found to be slightly reduced in annealed powders. This oxidation propensity made it imperative to perform characterization quickly after removing the powder from the argon atmosphere maintained in the glove box.

### **3.1.1.3 *Cryogenic milling***

Similar powder, in terms of particle size, was produced by milling at cryogenic temperatures without the use of NaCl. This eliminated the oxidation issues and reduced contamination effects in the later analysis. Although a cleaner method, cyomilling also has disadvantages. The careful control of the liquid nitrogen flow, frequent supply line fractures, and vial sealing issues at low temperature are all important considerations. However, once familiar with the equipment and after having improved the setup, the process became more predictable and the shorter milling times required were sufficient cause to prefer this method for powder generation.

The process for cryogenic milling was as follows (shown pictorially in Figure 3.2):

1. Submerge the sealed vial in liquid nitrogen contained in a small Styrofoam container

2. After having reached equilibrium (no violent boiling), place vial in polymer sleeve
3. Place the lid on the polymer sleeve and place in the clamp
4. Tighten the clamp but not the lock nut
5. Allow liquid nitrogen to flow at full capacity until liquid is ejected from the exhaust
6. Reduce the liquid nitrogen flow until liquid weakly trickles from the exhaust
7. Tighten the clamp again and fasten the lock nut
8. Close the door on the casing and start mill
9. Check frequently that hose is intact and the nitrogen flow produces a small vapor cloud

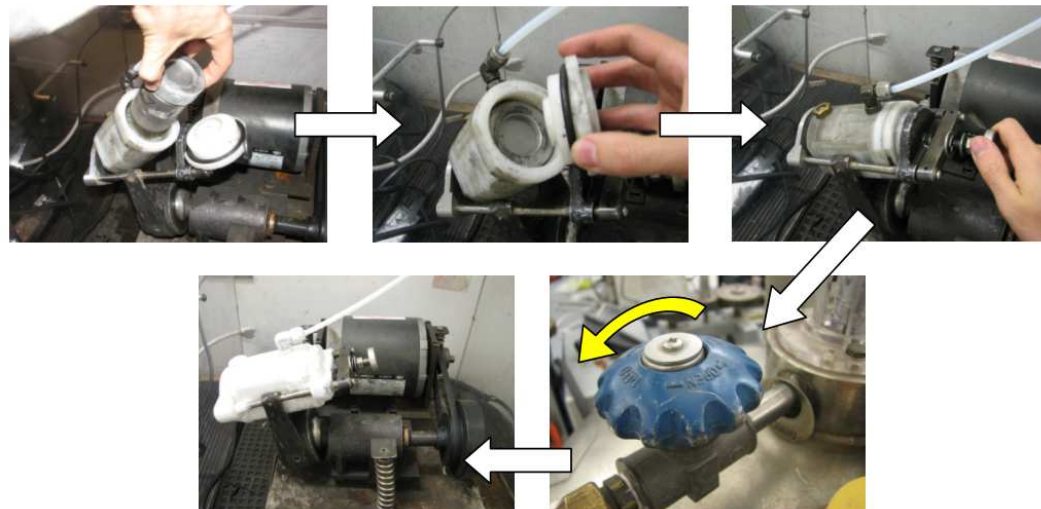


**Figure 3.2 – Equipment preparation for cryomilling**

After milling, the vial was put in the freezer while still cold. Only when ready for characterization was the vial transferred to the glove box where it was opened and then

analyzed. It is expected that grain growth at room temperature would not occur, though it has been noted in other work [9], because the materials are not highly pure due to contamination from the milling process and also that the solute intentionally added can be considered an “impurity.” Most of the samples were annealed later on which would have a far more important influence on grain size. Analysis of the as-milled powder directly from the freezer and up to a year later after having been stored in the glove box (typically slightly above room temperature) yielded the same results (within error) so the action was merely precautionary.

### **3.2 Annealing equipment and conditions**

Though characterization was performed on the as-milled powder, the truly interesting properties were those produced after annealing. The furnaces used for annealing were both Lindberg tube furnaces 2” in diameter. The samples were place into a quartz tube along with a thermocouple placed at the same position. The tube was pumped down to < 50 mtorr and refilled with 2% H<sub>2</sub> (bal. Ar). This was repeated three times and then the tube was allowed to pressurize to ~2 psi with the forming gas. The furnace was set to the appropriate temperature and allowed to stabilize for at least 30 min before the furnace was rolled over the tube. The thermocouple inside the tube was used to determine the sample temperature. This was especially important since there was disagreement between the furnace thermocouple and the sample thermocouple which was most pronounced at low temperatures (i.e. < 400 °C).

Samples were placed in ceramic boats for annealing. If more than one sample was to be run simultaneously in the same boat, the samples were placed in tantalum foil packets. No reaction was found to take place between the Ta foil and the samples, but after annealing at temperatures in excess of 600 °C, the Ta foil became brittle and removing the sample powder was difficult to accomplish without breaking the foil. The materials were annealed for 1 hr after reaching temperature, and the furnace was rolled off quickly after. Depending on processing temperature, the rate at which the furnace was rolled off was varied to reduce undue thermal shock on the tube (more slowly for higher temperatures). Typical cooling rates were ~2-3 °C/s. After annealing the samples were either prepared for characterization or placed in the glove box.

### **3.3 Characterization Methods**

To better observe and understand the microstructural evolution of the materials studied here, a variety of methods were used to determine their properties. Some properties, such as grain size, were determined and verified using multiple methods. Each characterization method has strengths and weaknesses and these were balanced to yield meaningful results. Simple methods, such as hardness and X-ray diffraction, were used for every sample while more involved techniques, such as transmission electron microscopy, were reserved only for the most significant samples as determined in the simpler methods. Many characterization techniques have caveats that must be considered when interpreting results. These may be

manifested as inherent limits of accuracy (e.g. X-ray grain size and energy dispersive spectroscopy) or small sample size and image artifacts such as faced when using transmission electron microscopy.

### 3.3.1 Vickers Microhardness

Hardness testing provides a quick method to get a general understanding of a material's mechanical properties. Though there is a general relation (i.e. Tabor's relation) between hardness and yield stress where the hardness is three times greater than the yield stress, this is assumed for a non-work-hardening material, and additional calculation is needed to account for work-hardening effects [76]. Despite inaccuracies in the relation, it provides valuable insight to strength of the material.

Hardness measurements were performed using a Buehler Micromet II Vickers microhardness tester. Samples for microhardness testing were prepared in two ways. The annealed powder was either compacted into a disk or it was supported by a hardened polymer. In the case of powder compacts, the powder was weighed out to create a compact approximately 1 mm thick. The most common diameter of the compacts was 3 mm though larger compacts were also made. The diameter of the compact was found to have no measurable effect on the hardness result. The die used for the compacts was made from tungsten carbide. Though many of the compacts were made using tungsten carbide punches as well, punches of that

material were prone to chipping and cracking so tool steel punches were made to replace the tungsten carbide punches.

Fabrication of the tool steel punches was accomplished by purchasing A2 tool steel which was manufactured to be 3 mm in diameter. The rod was sectioned into 3" lengths using a hacksaw and then wrapped in stainless steel foil and placed into a furnace preheated at ~970 °C and allowed to soak at that temperature for 30 min. The foil packet was then removed from the furnace and allowed to cool to room temperature. The rod was then placed in the drill press chuck with the vast majority of the length exposed. This portion was lightly sanded using 600 grit or finer sandpaper to remove the scale and periodically checked with the die as a measure of the fit. After the rod was uniform in diameter along the length and "slip fit" to the die, it was placed in the cutoff saw and cut into lengths appropriate for the die height (each about 5-7 mm in length). It was checked that the rod was perpendicular the saw blade so as to create a flat compact when in use. Any burr remaining after cutting was removed by file or by placing the punch in the drill press and sanding the face. Over-sanding would create a radius on the edge which didn't seem to reduce the effectiveness during pressing, but did require extra polishing of the compact to ensure flatness afterward.

All of the compacts were first rough sanded with 400 grit sandpaper. After both sides were flat, one side was chosen for sanding with 600 and 1500 grit sandpaper. The compact was final polished by hand using 1 µm alumina powder on a felt pad. Samples supported in a polymer were polished the same way. Powder was supported in epoxy and by superglue on a

glass slide. The epoxy samples were made by placing the powder on double-sided tape at the bottom of a mold. The mixture of hardener and resin were then poured on top of this. The sample was allowed to harden overnight and then polished as above. For the superglue on glass configuration, the powder was arranged in single layer on the glass slide. A drop of super glue was added to the top of the powder. Next, a weighing paper was used to push down on the glue and powder for several seconds ensuring the powder had good contact with the glass. The weighing paper was then removed, typically without any sticking, and the sample was allowed to dry at least 30 min before polishing. Comparisons of hardness values between the two polymer techniques were well within error.

A major difference in hardness results did arise with the compacted samples and the polymer-supported samples. The discovery was that the compacted samples were much harder than those of the polymer-supported samples. After testing a variety of preparation techniques, it was found that when a powder is annealed and then compacted the hardness can be as much as 1.5 GPa higher than the same powder in epoxy. The powder in epoxy had good correlation with powder compacted then annealed, and it is expected that the work-hardening during compaction was sufficient to cause the anomalous result. This work-hardening was not found to have a significant influence if the sample hardness was above 2.0 GPa. For peace-of-mind, all samples were tested in the supported powder configuration, many being retested after the initial compact testing.

All compact were produced by pressing between 2.0 GPa and 3.0 GPa. The most common pressure was 2.6 GPa. Even in cases where consolidated spheres were generated, this pressure was used to flatten them. The compacts routinely showed densities between 80% and 90%. The hardest materials and largest particle sizes showed the lowest densities. The trend was that the hard particles tended to be small in comparison to the softer material which especially convenient since the hardness indents were larger in softer materials which aided in keeping the indent within a single particle. All indents were made on single particles. Any particle boundaries were avoided, and if any indent showed cracking anywhere in the field of view (such as particle boundary) it was neglected. Also, if the indent did not show straight sides of equal length, it was not measured. At least ten measurements were made on each sample. If the spread of measurements was large, more measurements were made to help identify any outliers. Brittle samples or those with a small particle size commonly required as many as four indents for every one measured.

The load used was either 50 g or 25 g. There was no difference in measured hardness based on the load, so 25 g was the preferred load since it reduced artifacts. The indents were measured after a 12 s dwell time. Longer times (i.e. > 30 s) were used to check if the result would differ, but no effect was seen. The lengths of the diagonals were checked ensuring that all mechanical backlash was removed form the micrometer adjustments to ensure repeatability. Just the same, the stage was always raised into focus for indents, never lowered, so as to reduce any deviations based on equipment error cause by compliance issues

in the gearing. Samples were always supported on  $\frac{1}{4}$ " ceramic backing which was supported underneath by the vise fixture of the microscope.

### 3.3.2 X-ray diffraction

A Rigaku DMax/A diffractometer was used for all X-ray spectra collected here. Though powders were used primarily, in some instances compacted discs (6 mm or greater) were used to collect spectra. As the compact method was rare and the difference in results negligible, the powder method will be detailed. A glass slide was scratched using a diamond scribe and broken into small rectangles approximately 5 x 10 mm (a size appropriate for the holder). The glass slide section was then cleaned with ethanol. Double-sided tape was cut to size and placed on the glass slide being careful not to contaminate the tape and to ensure no glass was left exposed. The powder was removed from the glove box and sprinkled onto the tape. Another glass slide, cleaned with ethanol, was used to press the powder onto the tape. All of this took place on top of a weighing paper which served to capture any powder that did not stick to the tape. Powder was added until a thin uniform layer was deposited, and by tapping the slide, it was ensured only well-adhered particles remained.

The glass slide was placed into a holder in which mounting clay was located. The clay was mounded above the surface of the sample holder and the glass side was placed on this. Another, clean glass slide was used to push the sample down and ensure it was level with the surface of the sample holder for ideal placement in the X-ray chamber. Before the sample

was analyzed, a single-crystal silicon standard was used for alignment. Based on peak location and intensity the  $\theta$  (sample) and  $2\theta$  (detector) axes were realigned for maximum accuracy and intensity. The equipment was programmed to proceed stepwise in  $0.02^\circ$  increments and dwell for 1 s at each interval. Typical scans were from  $35-100^\circ$  on  $2\theta$  though others were used as needed.

The data was saved as a text file which was later opened with XPowder X-ray analysis software where a three step treatment was performed consisting of “function filter” smoothing, background subtraction, and “Rachinger Optimized”  $K\alpha 2$  stripping. The modified file was saved separately. The modified file was then opened with Origin analysis software and the data was plotted. Using the built-in peak fitting function, a “fit multiple peaks” sub program was chosen and the peaks were selected manually. The program then reported the Gaussian full width at half maximum (GFWHM) as well as peak centers, maximum intensities, etc. This information was transferred to an Excel file which used it to determine the peak broadening due to the sample (instrumental broadening was subtracted). The line broadening,  $\beta$ , was then used to determine the grain size,  $d$ , by application of the Scherrer equation [13]:

$$d = \frac{K\lambda}{\beta \cos \theta} \quad (3.1)$$

where  $\lambda$  is the X-ray wavelength,  $\theta$  is the angle of the reflection, and  $K$  is a shape factor. Cu K $\alpha$  X-ray radiation was the only used and has a wavelength of 1.5418 Å. The shape factor was set to 1 for the work here. The application of this equation is limited to small grain sizes due to competing broadening effects such as those from instrumental imperfections and strain. For this reason, estimation of grain size using XRD was always considered skeptically. Though generally accurate for grain sizes 30 nm and below, once above that limit there was a precipitous decline in accuracy. A grain size reported to be 50 nm by XRD, may actually be microns in size. If the grain growth is abnormal, the estimation will also be misleading since the large grains will not contribute to the broadening and will likely be masked in the signal.

XRD is first and foremost a tool for structural analysis, and therefore, the information provided on peak presence and location was also very useful. For example, the five peaks of Cu (i.e. 111, 200, 220, 311, 222) in the common scan range used were of greatest intensity in the scans, but if other peaks were present, that was a clear indicator that second phase was present. Typically of an intermetallic or oxide, these peaks would often be very weak in relation to the Cu fundamental reflections, but served useful for identifying major phases. Techniques such as selected area electron diffraction as utilized in TEM were much more sensitive to foreign phases, but matching the peaks using the XRD software proved very valuable. Unfortunately, due to the rarity of the alloys produced here, many of the possible intermetallics and oxides were not available in the database.

### **3.3.3 Optical microscopy**

Samples analyzed using optical microscopy were few in comparison to the other techniques. A Nikon Epiphot 300 microscope was used where samples were attached to double-sided tape and inverted above the objective lens. The samples were prepared in a method analogous those used in hardness testing. That is, they were polished with consecutively finer grits of sandpaper and final-polished with alumina paste. Optical microscopy was only used in reporting results related to the porosity of the antimony alloys (Chapter 6) which had extensive networks of large pores which made the technique valuable. Aside from that application it was generally used to inspect sample roughness during polishing.

### **3.3.4 Scanning electron microscopy**

Scanning electron microscopy (SEM) provides a valuable intermediate magnification technique. Though some SEMs can achieve extremely high resolution, the ones used here were general purpose units more valuable for their speed of data acquisition and ease of sample preparation. Once again, samples were polished as done for hardness measurement, and then mounted using double-sided carbon tape on a conductive holder. The analysis methods used were secondary electron (SE) imaging, backscatter electron (BSE) imaging, energy dispersive X-ray spectroscopy (EDS), and compositional mapping using EDS. The primary information gained by SEM was the composition, compositional distribution, powder morphology, and sample porosity.

BSE provides compositional contrast based on the electron matter interaction, and the systematic variation of this with atomic number differences. Though not used to provide atomic identity, it was useful in determining areas rich in a species of drastically different atomic number. EDS can provide composition, giving relative percentages of elements, but generally lacks high accuracy, especially when done in a standardless or quasi-standardless manner [77]. Using compositional mapping is a powerful tool as it correlates position and composition. The use of an SEM with a silicon drift detector (SDD) cuts down on collection time significantly and increases statistical accuracy. The JEOL JEM 6010LA used in the Cu-W study (Chapter 7) provided this ability and proved useful in determining the distribution of W in the Cu matrix.

SEM can be combined with a focused ion beam (FIB) to create a dual beam microscope. The FIB can “machine” away material in highly localized and precise manner and provide site specific information. The grain size can be determined by channeling of the ions. The ions are extremely large in comparison to the electrons used for SEM, and depending on the crystallographic orientation will “burrow” or channel between atoms. The more open the crystal orientation, the darker the image appears, since ions are more easily implanted and generate a weaker signal. The contrast difference between different crystal orientations (i.e. grains) gives grain size information. The resolution is not as good as TEM, but can provide valuable information about the sample since it can capture a larger area than in TEM. The act of viewing the sample using this technique is destructive, so careful microscopy is needed to

eliminate artifacts. FIB is also a useful technique for creating TEM specimens from a specific region, though there is a tendency for sample damage causing an amorphous region to form. With diligent use, FIB can be a powerful tool for analysis.

### **3.3.5 Transmission electron microscopy**

Transmission electron microscopy (TEM) provides a means to image nanoscale grains directly, and therefore gives precise, quantitative information. In addition to average grain size, such as that derived from XRD, it also gives grain size distributions. This is accomplished by generating a selected area electron diffraction (SAED or simply SAD) pattern. From the SAD pattern a wealth of information can be derived. In regard to grain size in a polycrystalline material, rings will appear which can be selected to highlight the grains of that orientation in a dark field image. The methods, theory and terminology of the technique will be covered in any text book on TEM, but Williams and Carter [78] have an easy to read text on the subject.

For as valuable as TEM is to gaining quantitative information on nanocrystalline samples, the preparation of the samples is not trivial. For electron transparency, a sample should be less than 100 nm thick, and in a wedge configuration, should have a very shallow angle to permit the largest possible area to be examined. This must be accomplished without damaging the area and introducing artifacts or contamination. As mentioned above, FIB can be used to produce the samples, but unless very low beam energies are used, a thick amorphous surface will

develop and degrade the sample quality. Several methods for sample preparation were used here and cover many techniques not including FIB.

The first method of producing TEM samples was electropolishing. The technique involves applying a bias on a conductive sample while spraying with a small jet or jets of an electrolyte to create a current. The electrolyte is an appropriate electropolishing solution for the sample material and the ions act to carry the current. The process leaves a small hole in the center surrounded by a thin “dished out” area (if the equipment is operating properly). The rate of removal should be nearly uniform across the sample surface to ensure a large thin area after a hole is first produced. Porosity in the sample tends to cause early termination of the automated process by anomalous light detection which indicates a hole has been created and the sample is properly thinned. The thinned surfaces should be highly polished when finished.

Samples for electropolishing were prepared by compacting and thinning by hand until ~100  $\mu\text{m}$  in thickness. These were then electropolished with 30 vol% nitric acid in methanol at -20 °C. A Tenupol II electropolisher was used at 18 V with a jet speed of 0.5 (unitless, on a scale of 0-10). The current was typically between 200-300 mA. Because the samples were never fully consolidated, the process did not work well. Also, due to high solute contents of significantly different materials, the surface condition was usually poor. The process worked well for the coarse-grained Cu dummy samples made from pure foil, but the experimental samples were always more troublesome.

The samples had a very limited thin area and highly uneven surfaces, so a finishing step was incorporated using a Fischione Model 1010 ion mill. The program typically consisted of a high-angle, high-energy roughing step, followed by incremental steps to a final low energy low angle configuration. A common program was 15° with 3.5 kV, 5 mA for 20 min, 9° with 2.5 kV, 5 mA for 30 min, and finally 6°, 1.5 kV, 5 mA for 45 min. Liquid nitrogen cooling was maintained throughout the process. After this process, the thin area was much larger and the surface roughness was eliminated.

Other configurations such as pressing powder into gallium and placing powder in epoxy were also tried. The gallium supported powder worked reasonably well in electropolishing as the copper or brass would etch at a slightly faster rate, but could not be easily ion milled due to the low melting point of the gallium. This also made handling of the discs punched from the compacted sheets difficult requiring constant refrigeration. The epoxy supported powder was time-consuming to prepare and never extending to electropolishing, mechanical polishing, or ion milling. The best solution, compacting then annealing samples followed by electropolishing and ion milling, was the technique of choice. If the electropolishing program was terminated prematurely by porosity, the sample was electropolished in five second increments with the detector off. Over-polishing (i.e. creating a large hole) was not a major disadvantage since the ion mill did an excellent job of final polishing.

The prepared samples were examined using the SAD patterns, centered dark field (CDF or simply DF), bright field (BF), and EDS. The SAD patterns give structural and phase

information analogous the XRD, but the sensitivity for second phase detection is much higher. The presence of intermetallics and oxides at low annealing temperatures never showed in the X-ray spectra, but were readily visible in the SAD pattern. Oxide formation could be an artifact of sample preparation, but this not necessarily the case. The SAD rings corresponding to the Cu or brass were selected using the smallest available objective aperture and used to identify grains. Second phase rings were selected in the same manner to identify precipitates.

Dark field images were particularly useful for deriving grain size and distribution information. As only grains with a specific crystallographic orientation appear when the appropriate ring is selected, the image could then be used to determine the grain metrics. Image J was used to create binary images which were then processed using the “analyze particles” function. This worked well in determining grain or precipitate size, but for systems where intermetallic rings may overlap with the chosen fundamental reflection this can cause both to show up in the dark field image. There is no substitute for judicious choice when determining grain size. The grain size was also measured in Image J using the line function and measuring two directions perpendicular to each other. The average was taken as the grain diameter. Typically 300 grains were measured, but when the grain size was large, the limit was nearer to 200 grains.

## **4 Stabilization of Copper by Zirconium**

---

---

Copper zirconium alloys were generated by mechanical alloying via high-energy ball milling. The addition of zirconium to copper in quantities of 1, 2, and 5 at% has been found effective at stabilizing the grains in the nanocrystalline state at homologous temperatures in excess of 0.85. Two processing conditions were chosen as exemplar studies. In one case the milling was performed for 8 hr at room temperature and used 1 wt. % sodium chloride as a process control agent (PCA). In another configuration the powder was milled for 4 hr at liquid nitrogen temperature with no PCA. Both were successful in eliminating cold welding of the powder to the milling media and vial. The two conditions responded very similarly to annealing with the greatest variation being the as-milled condition. Higher zirconium content led to substantial hardening during annealing, but overall grain size stabilization was not found to be enhanced.

## 4.1 Introduction

The unique properties of metals with average grain sizes below 100 nm have lead to great interest in their study. Although copper has been reported to have remarkably high strengths when nanocrystalline [3-5], the instability of this microstructure leads to concern for commercialization purposes. The high energy state due to excessive grain boundary area renders most nanocrystalline materials susceptible to grain growth at low temperature (e.g. Cu at 75 °C [79]). Indeed, some highly pure nanocrystalline metals have been found to undergo grain growth at room temperature [9], one of which is copper [74]. If the nanostructure cannot be retained at even modest processing and/or service temperatures, the material is of no practical use. The addition of dopant materials which segregate to the grain boundaries have been found successful in reducing the susceptibility to grain growth by two basic routes; kinetic or thermodynamic stabilization [80] as discussed in Sections 2.3.1 and 2.3.2 respectively. Solutes of a larger atomic radius which do not have appreciable solubility in the host material can be put into solid solution by nonequilibrium processing such as mechanical alloying, and from the metastable, as-milled condition, annealing allows the solute to diffuse to the more favorable (lower energy) grain boundary sites which make up an appreciable volume of nanocrystalline materials. Once at these boundaries, the grain boundary energy can be reduced, and, in the ideal case, eliminate the driving force for boundary migration and crystallite growth [56, 74]. This thermodynamic approach is the basis for the use of zirconium which has a much larger atomic radius than copper and hence generates significant lattice strain which can be reduced by segregation of zirconium to the

grain boundaries where it can then be active toward stabilization. A recently developed model of grain boundary energy with solute segregation [64] is applied to the system to establish feasibility of complete thermodynamic stabilization. This modified Wynblatt-Ku model is also discussed in Section 2.3.2.1.

To determine the stabilization efficacy of zirconium in copper the two powders were mechanically alloyed using a Spex shaker mill. Zirconium was added in the amounts of 1, 2, and 5 at%. Two milling conditions were chosen for study. In the first, powders were milled at room temperature for 8 hr and 1 wt% NaCl was added as a process control agent (PCA). In the second condition, no PCA was added and the powders were milled for 4 hr at liquid nitrogen temperature (-196 °C). Using a PCA is common in mechanical milling/alloying, but powder contamination is a serious shortcoming [37]. Without a PCA the alloys milled at room temperature quickly agglomerated into large flakes and spheres as well as adhering to the milling media and the vial. Both methods eliminated adhesion to the vial and milling media and generated coarse powders. The thermal stability was investigated by annealing for 1 hr at 100 °C intervals to a maximum of 1000 °C. Both sets of powder were found to possess greatly enhanced grain size stability over pure copper as determined by microhardness, x-ray diffraction, and both transmission and scanning electron microscopy characterization.

## 4.2 Experimental Details

Elemental powders of copper (Alfa Aesar, 99.9%) and zirconium (Cerac, 99.7%) were added to a 440 stainless steel vial (Spex SamplePrep) with grade 25, 440 stainless steel ball bearings (Salem Specialty Ball). The ball charge consisted of 17 balls 0.3125" in diameter and 16 balls 0.250" in diameter. The ball to powder weight ratio was maintained at 10:1. All materials were loaded into the vial in an argon atmosphere ( $O_2 < 1$  ppm) and sealed before transferring to the mill. A Spex 8000 mixer/mill was used to mechanically alloy the powders. Zirconium was added in quantities of 1, 2, and 5 at%. Two milling conditions were undertaken. In the first, powders were milled at room temperature for 8 hr and 1 wt% NaCl (Alfa Aesar, 99.99%) was added as a PCA. In the second condition, a modified Spex 8000 mixer mill was used where the powders were milled for 4 hr at liquid nitrogen temperature (-196 °C) and no PCA was added. The conditions will be denoted as CuXZr-RT and CuXZr-C for the first and second conditions respectively where  $X$  denotes the atomic percentage of zirconium (i.e. Cu5Zr-C is copper with 5 at% zirconium milled at cryogenic temperature for 4 hr). The milled powders were annealed under 2% H<sub>2</sub> (bal. Ar) for 1 hr at temperatures from 100 °C to 1000 °C in 100 °C increments in a Lindberg tube furnace into which the samples were inserted once the furnace had stabilized at the appropriate temperature. After annealing, the powders were compacted at room temperature in a 3 mm tungsten carbide die at a uniaxial pressure of 2.6 GPa. The powder compacts were polished and at least 10 Vickers hardness measurements were collected using a Buelher Micromet II with a 50 g load applied for 12 sec. X-ray diffraction (XRD) analysis was conducted using a Rigaku DMax/A X-ray

diffractometer using Cu K $\alpha$  radiation. Proper alignment was verified before each use using a standard single crystal silicon sample. The spectra were processed by removing the background and K $\alpha_2$  contribution (optimized Rachinger's method) using Xpowder software ([www.xpowder.com](http://www.xpowder.com)). The grain size was estimated using the Scherrer equation [13] applied to the first peak of the pattern. Transmission electron microscopy (TEM) analysis was carried out using a JEOL 2000FX with a beam energy of 200 keV. Samples for TEM analysis were prepared by pressing the powder in gallium (as-milled powder) or by annealing compacted powder. Both methods were followed by electropolishing 3 mm disks in 30 vol% nitric acid in methanol at -20 °C in a Tenupol-2 electropolisher and finishing by ion milling using a Fiscione Model 1010. Scanning electron microscopy (SEM) and focused ion beam channeling contrast imaging (FIBCCI) were performed using an FEI Quanta 3D FEG dual beam microscope.

### 4.3 Results

As shown in Figure 4.1, the as-milled powders showed total solubility for all compositions in both milling environments. The XRD patterns show nearly identical spectra for both milling conditions for each of the compositions. The peaks become broader and less intense as Zr content increases. The cryo-milled alloys show this effect somewhat more noticeably and would therefore be expected to possess a smaller grain size at each

composition than the room temperature milled counterpart. The high-angle peaks are nearly unidentifiable in the 5% alloys and are on the order of the background noise.

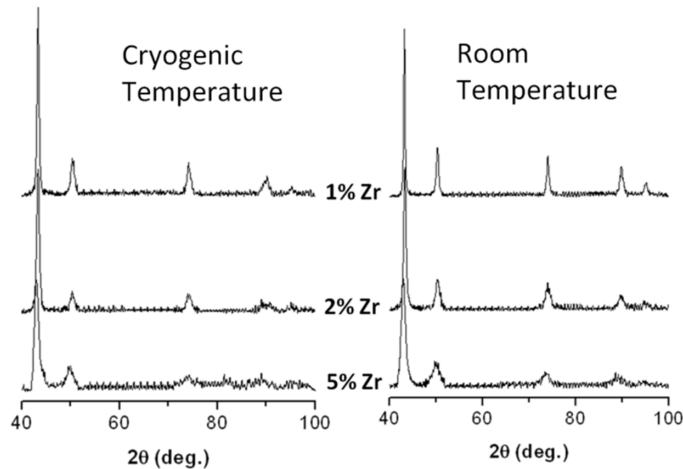


**Figure 4.1 – XRD comparison of the as-milled Cu-Zr alloys**

The XRD patterns for each annealing temperature for Cu<sub>1</sub>Zr-C is shown in Figure 4.2. It can be seen that even up to 800 °C the pattern shows negligible change. The most noticeable sharpening occurs for the high angle peaks (i.e. 311 and 222), but they too are not substantially sharpened until the highest temperatures.

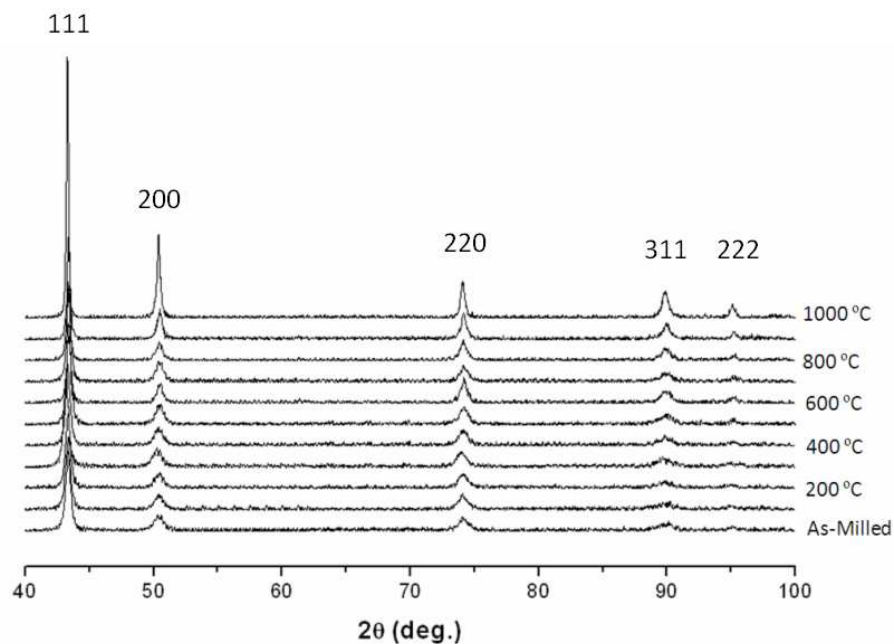


**Figure 4.2 - Cu1Zr-C X-ray spectra after annealing for 1 hr at increments of 100 °C**

The grain size estimations of the alloy powders by XRD are shown in Figure 4.3, and it can be seen that the 1% Zr alloys are equally stable to the higher concentrations (2% and 5%) at modest annealing temperatures and even more stable at the highest temperatures. Whereas with the 5% Zr alloys (triangles), grain size begins rising significantly at 500 °C (though from a lower initial value), the grain size of 1% and 2% alloys did not increase significantly until 600 °C. For the 1% and 2% alloys this rise, though noticeable, is not extensive, and the grain sizes remain within 10 nm of their as-milled conditions until nearer to 800 °C. The cryo-milled alloys (open symbols) consistently maintained a smaller grain size than the room temperature-milled alloys (filled symbols), and most noticeably after 600 °C. However, for a fixed composition, the *trend* in size was mirrored even if the size itself was not. The plateau effect in the pure copper samples is assumed to be generated by bimodal grain growth and

not actually maintaining a uniform size in that range. The reported grain sizes of 40 nm or greater from XRD are considered skeptically, as it has been found that they are prone to inaccuracy [48].

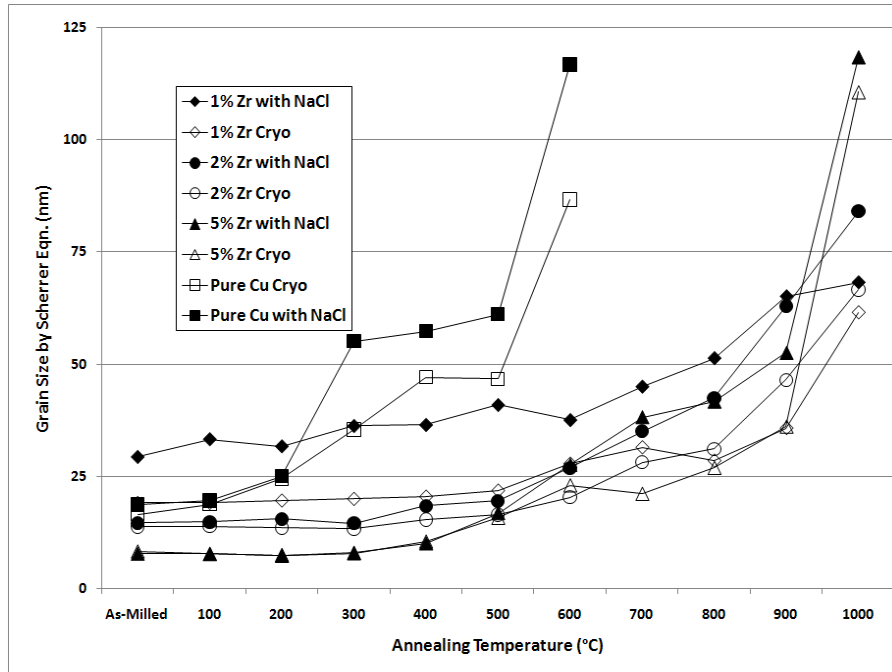
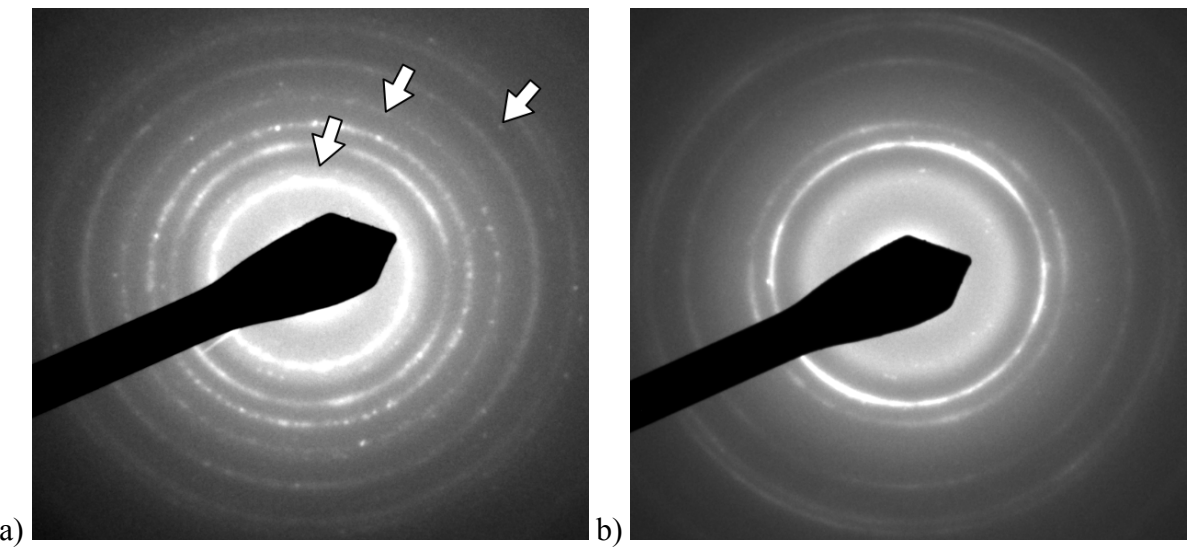


Figure 4.3 - XRD grain size estimations for Cu-Zr alloys and pure Cu equivalently processed

As seen in Figure 4.1, although the 1% and 2% Zr alloys have closely related peak positions, the 5% Zr addition shows a substantial peak shift indicative of lattice expansion caused by the dissolution of Zr into the Cu lattice. The broad, poorly defined peaks in the as-milled condition made precise lattice parameter calculation impractical, but the trend was a lattice expansion at low annealing temperature and sharp drop to within error of pure copper (3.6148 Å [13]) from 500 °C to 600 °C. The amount of lattice expansion increased with

increasing solute content and the RT as-milled lattice parameters in both the 2% and 5% Zr alloys were larger than those for the cryo-milled ones. However, after annealing to 100 °C, the cryo-milled alloys had a larger spacing. The cause for the discrepancy was examined by selected area diffraction in the TEM. Figure 4.4 shows the 5% alloys in the as-milled condition. These indicate that intermetallic formation occurs in the RT milled alloys, but is suppressed in the cryogenically milled alloys. The broad diffuse nature of the Cu<sub>5</sub>Zr-C rings in comparison to that of the Cu<sub>5</sub>Zr-RT alloy indicates a smaller grain size though the two are identical as estimated by the Scherrer grain size in Figure 4.3. The formation of a partially amorphous structure is not ruled out due to the ease of glass formation in the Cu-Zr system [81, 82]. After low temperature annealing the structure may become more ordered and the lattice spacing increase. Though the lattice parameter measurements were not able to be considered absolute, the trends are considered instructive.



**Figure 4.4 - Selected area diffraction patterns for the 5% Zr alloys in the as-milled condition a) Cu5Zr-RT with intermetallic rings indicated by arrows, b) Cu5Zr-C without intermetallic rings. The innermost ring is attributed to ZrO<sub>2</sub>.**

Variation in the hardness is qualitatively similar to that of the lattice parameter. The microhardness measurements shown in Figure 4.5 reveal a hardening effect at low temperatures for the 2% and 5% Zr alloys. Higher Zr contents result in a greater hardening response as has been observed elsewhere [83]. The 1% Zr alloys are both remarkably stable throughout the temperature range, with the room temperature environment being consistently softer which would be expected for a larger grain size as in Figure 4.3. In the as-milled conditions the Cu1Zr-C sample is considerably harder than the Cu1Zr-RT alloy, the 2% Zr alloys are nearly equal, and the 5% Zr alloys show the Cu5Zr-RT alloy to have a higher as-milled hardness. The Cu5Zr-C and Cu2Zr-C samples are equivalent in as-milled hardness but at 100 °C they have separated significantly. At 900 °C the entire range of compositions and milling conditions is still well stabilized, but at 1000 °C they all drop precipitously, though

the 1% alloys are affected least drastically. For the 1% alloys to maintain hardness in excess of 1.75 GPa even at 1000 °C is truly remarkable.

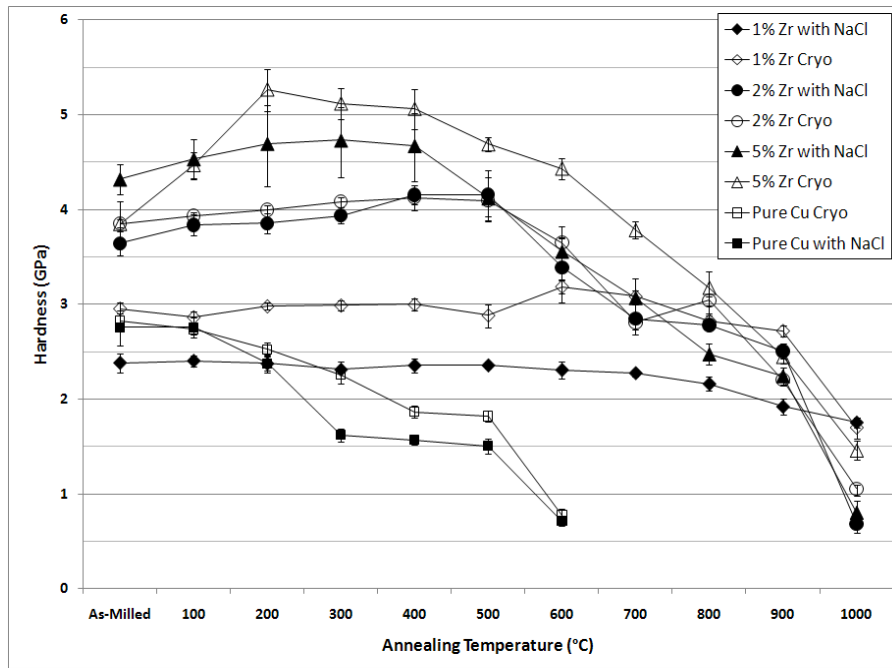
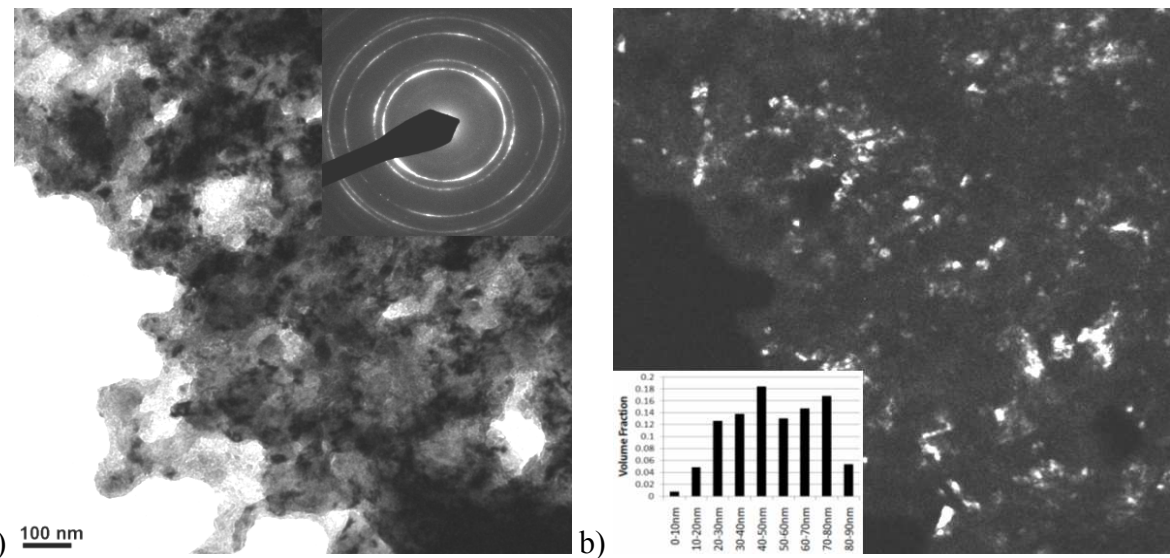


Figure 4.5 - Hardness values for Cu-Zr alloys and pure Cu equivalently processed

The impressive hardness, even at  $> 0.8 T_m$ , was verified by testing the annealing and compaction in several configurations, and it was found that the hardness is sensitive to the order of compaction and annealing. The various methods tested were to anneal the powder then compact it, anneal the powder then support it in epoxy, and to compact the powder then anneal. The last step was always to polish the surface of the powder. When pure, unmilled copper was annealed at 1000 °C then pressed to 2.6 GPa, the hardness of the polished compact was  $\sim 1.4$  GPa. Of course this is not expected of pure copper. If the annealed powder

was not pressed but supported in epoxy the hardness was only ~0.6 GPa. Obviously the compaction step had introduced significant cold work. This effect was not observed for Cu1Zr-C samples which were also tested in the different configurations. It was noticed, as reported previously [39], that the cryo-milled compact expanded when annealed while the unmilled copper did not. The gas expansion may influence the stability by additional stress, but the hardness of the compacted then annealed sample was within 8% (ignoring error bars) of the annealed then compacted sample though on the lower extreme. In general, it was observed that samples of hardness greater than ~1.75 GPa did not experience the hardening effect due to the strain hardening of compaction.

TEM investigation confirms both the nanocrystalline nature of the material as well as the stability at very high homologous temperatures. Cu1Zr-C was chosen as a representative case since the stability was equal to or greater than the other compositions and milling environments with the lowest concentration of zirconium. The TEM bright field (BF) and dark field (DF) images of Cu1Zr-C in the as-milled condition are shown in Figure 4.6 with volume fraction grain size distributions and selected area diffraction (SAD) patterns inset. The Cu-fcc diffraction rings are clearly visible and continuous, indicative of a fine polycrystalline structure. The dark field image using the 111 and 200 rings confirms the existence of many small grains though a few larger grains (>50 nm) are present as well. The volume average grain size was found to be 27.8 nm and the number average 18.4 nm.



**Figure 4.6 - Cu1Zr-C in the as-milled condition a) bright field image with SAD pattern inset top-right and (b) corresponding dark field image with volume fraction grain size distribution inset bottom left**

The microstructure was examined in a similar manner after the powder was annealed at 900 °C. The TEM BF and DF images of Cu1Zr-C after annealing at 900°C are shown in Figure 4.7. The SAD pattern (Figure 4.7a) shows a coarsening of the structure as the Cu-fcc diffraction rings are no longer continuous. Also, new rings have appeared which have smaller diameters and therefore larger lattice spacings. Figure 4.7b shows the BF image and Figure 4.7c shows the DF image using the 110 and 200 rings as above. The volume fraction histogram is inset in the DF image on the bottom right. The volume average and number average grain sizes were found to be 59.2 nm and 53.6 nm respectively. Since Cu and Zr form intermetallics, the appearance of new rings was anticipated. Selecting the inner SAD rings for DF, many small second phase particles were found to exist throughout the material as shown in Figure 4.7d. The precipitates have volume and number fractions of 7.5 nm and

4.0 nm respectively with 78% of the precipitates being 5 nm or less and the next 19% being in the range of 5-10 nm.

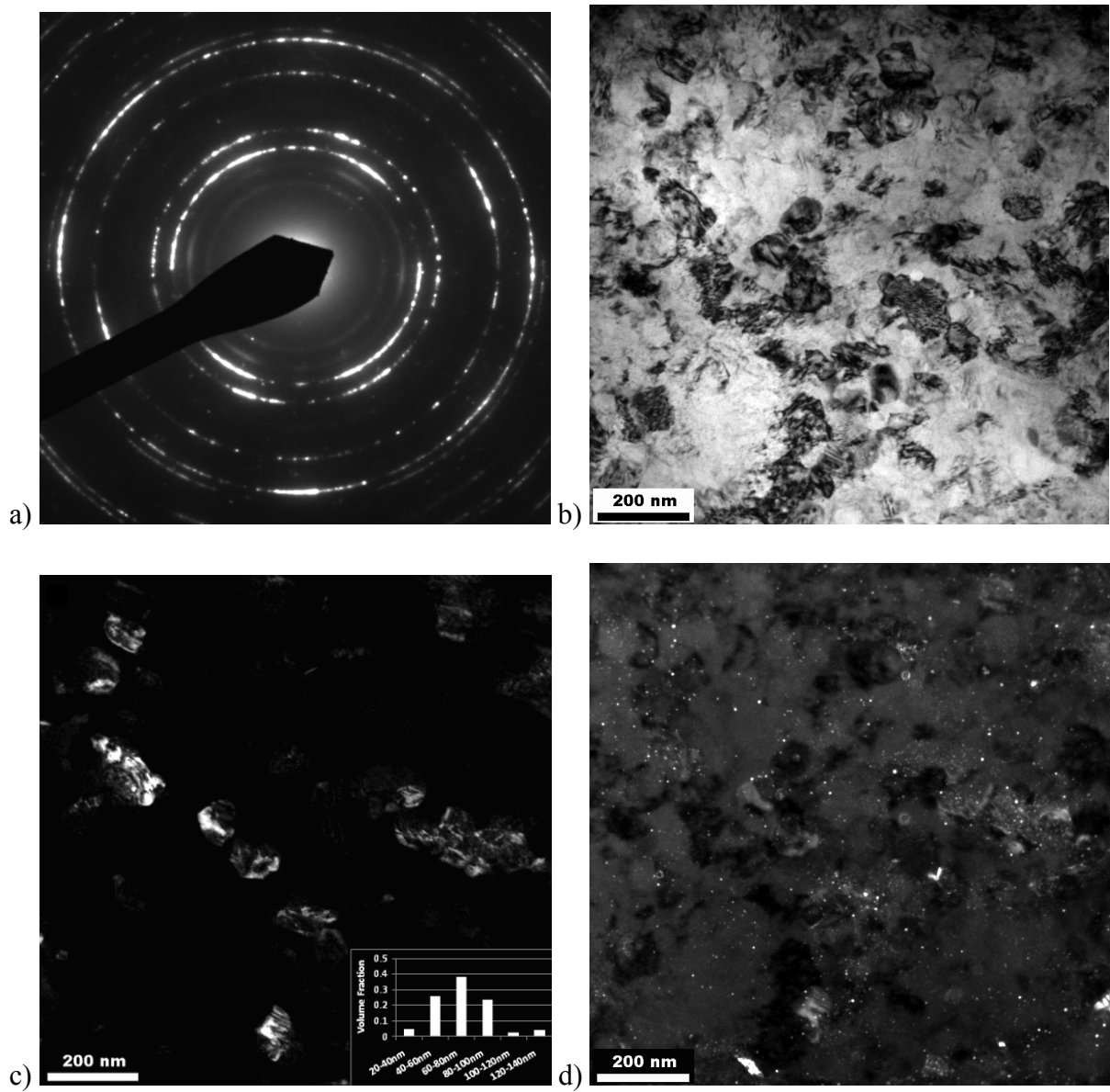
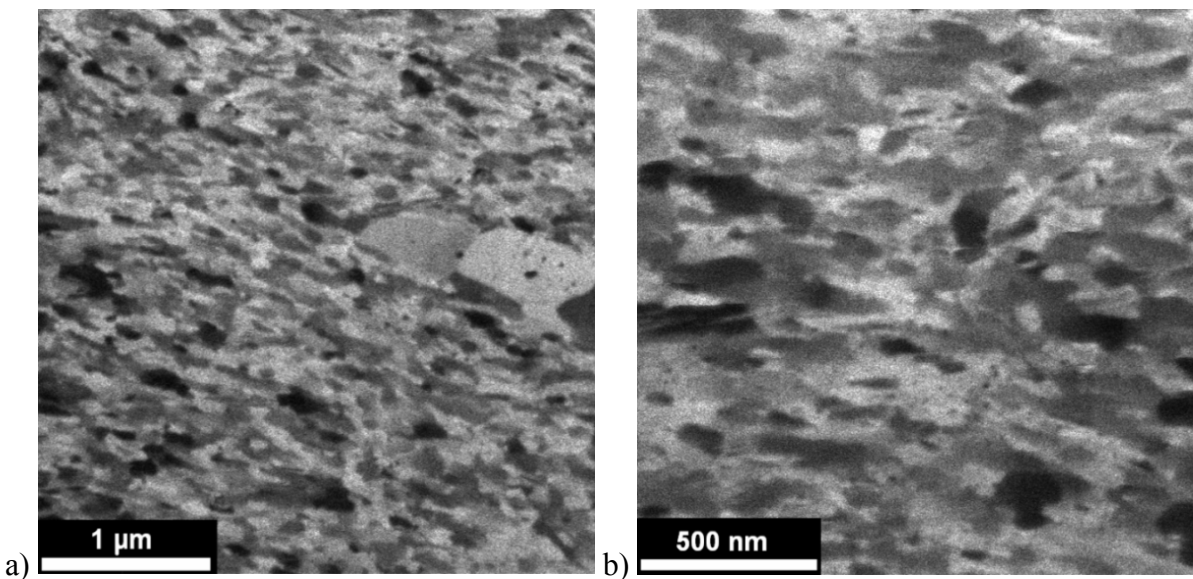


Figure 4.7 - Cu<sub>1</sub>Zr-C annealed for 1 hr at 900°C a) SAD pattern, (b) Bright field image (c) dark field image generated by the 110 and 200 diffraction rings with volume fraction grain size distribution inset bottom left (c) dark field image using innermost rings of SAD pattern shown in (a).

In other work on alloys with higher Zr composition (not reported), XRD spectra contained appreciable peaks in addition to those from Cu. These were compared to the SAD patterns at lower composition and found to correlate well which aided in phase identification. The brightest ring not belonging to copper, the innermost ring, was found to correspond to zirconia ( $\text{ZrO}_2$ ), while the principal intermetallic phase was found to be  $\text{Cu}_5\text{Zr}$ , but other phases are likely present. The formation of  $\text{ZrO}_2$  may occur during the electropolishing and/or transport of the samples between the TEM and the glovebox. SEM examination of Cu<sub>1</sub>Zr-C annealed at 1000 °C revealed no appreciable oxygen content by EDS, but it is not a quantitative result and oxygen is likely present during processing. The  $\text{Cu}_5\text{Zr}$  ring is quite faint and broad indicating limited and small precipitate formation as observed in TEM examination.

The considerable stability suggested by XRD, microhardness, and TEM was still regarded cautiously. Though considered the most reliable method, TEM results were verified by FIB channeling contrast imaging (FIBCCI) since the possibility of grain fallout during electropolishing was considered as an artifact that may shift the grain size to unrealistically small averages by the loss of the largest grain sizes. In the FIBCCI method, though the smallest grain sizes could not be resolved, the presence of large grains that may be lost in sample preparation could be resolved. This technique provides a valuable intermediate analysis between optical microscopy and TEM for evaluating grain size [66, 67]. The results of the analysis of the material annealed at 900 °C are shown in Figure 4.8. The grains are shown to be nearly equiaxed and uniform in size. Aside from the grains of 500-600 nm at

center-right in Figure 4.8a, there were no other large grains in the sample area ( $\sim 20 \times 20 \mu\text{m}$ ). The higher magnification in Figure 4.8b shows many of the grains are below 100 nm, but the resolution is not sufficient for an exact measurement. However, this technique is not intended to reveal exact grain size but to determine if there is a significant presence of large grains that was excluded from measurement by TEM. Also, considering that the areas of uniform shade (especially medium gray) may be a collection of unresolved grains, the TEM and FIBCCI results are in good agreement and considered representative of the bulk material.



**Figure 4.8 - FIB grain size image of Cu1Zr-C annealed at 900 °C by ion channeling contrast at magnifications of (a) 40,000X and (b) 80,000X**

## 4.4 Discussion

Zr is an oversize atom in Cu with a size misfit of 24%. Zr has an equilibrium solubility in Cu of only 0.12 at% at 972°C [84, 85] and it is expected to work well for the stabilization of Cu by Zr segregation to the grain boundaries. The basis for the thermodynamic stabilization effect due to solute grain boundary segregation was treated in a recent paper [64] and in Section 2.3.2, but will be briefly outlined here also. The grain boundary energy,  $\gamma$ , at grain boundary solute segregation excess,  $\Gamma_s$ , is given by:

$$\gamma = \gamma_o + \Gamma_s [\Delta H_{seg} - T\Delta S_{seg}] \quad (4.1)$$

where  $\gamma_o$  is the intrinsic (no segregation) grain boundary energy and  $\Delta G_{seg} = \Delta H_{seg} - T\Delta S_{seg}$  is the Gibb's free energy change due to segregation. A regular solution model based on a bilayer grain boundary and configurational (mixing) entropy was developed to evaluate  $\Delta H_{seg}$  and  $\Delta S_{seg}$  [64]. This includes both the chemical [59] and elastic [60] size misfit effects for segregation, following the method proposed by Wynblatt and Ku [61, 62, 72] for surface segregation. Using A to denote solute (Zr) and B solvent (Cu), the equation for  $\Delta G_{seg}$  is:

$$\Delta G_{seg} = (\gamma_A - \gamma_B)(1 - \alpha)\sigma - \frac{8\Delta H_m}{Z} \left[ z_{in} (X_A^s - X_A^b) - z_{out} \left[ (X_A^b - \frac{1}{2}) - \alpha(X_A^s - \frac{1}{2}) \right] \right] + \Delta H_{el} - RT \ln \left[ \frac{X_A^b(1 - X_A^s)}{X_A^s(1 - X_A^b)} \right] \quad (4.2)$$

$\gamma_A$  and  $\gamma_B$  are surface energies,  $\alpha = 5/6$ ,  $\sigma$  is the molar grain boundary area for the solvent,  $X_A^s$  and  $X_A^b$  denote the mole fractions of solute segregated to grain boundaries and in the bulk (grain interior), respectively,  $\Delta H_{el}$  is the elastic strain energy enthalpy as given in [64],  $\Delta H_m$  is the enthalpy of mixing of an equimolar liquid of A and B (used to evaluate the bond interaction parameter  $\Omega \cong 4\Delta H_m$  in the regular solution model) and  $z_{in} = 6$ ,  $z_{out} = 3$ ,  $Z = z_{in} + 2z_{out}$ . The grain boundary surface excess for the bilayer model is given by  $\Gamma_s = 2(X_A^s - X_A^b)/\sigma$ . Rearrangement of equation 4.1 gives the normalized grain boundary energy as:

$$\frac{\gamma}{\gamma_o} = 1 + \Gamma_s \frac{\Delta G_{seg}}{\gamma_o} \quad (4.3)$$

Detailed numerical results for the grain size as a function of temperature and total solute content  $X_A^o$  require combining Equations 4.1 and 4.2 with a mass balance equation for A. This level of detail is beyond the scope of the current investigation. Instead we use the limit of infinite grain size where  $X_A^b = X_A^o$ . As discussed in [64], if the plot of  $\gamma/\gamma_o$  vs.  $\Gamma_s$  intersects the  $\gamma/\gamma_o = 0$  axis in this limit, thermodynamic stabilization is possible for the  $X_A^o$  and  $T$  values assumed. We could have also used a plot of  $\gamma/\gamma_o$  vs.  $X_A^{gb}$  in this same context. This model requires values which are readily available in the literature. The parameters used in the following analysis are listed in Table 4.1. The  $\Delta H_m$  values used were -16 kJ/mol and -25 kJ/mol [86] for Cu-Zr and Fe-Zr respectively, and -9.1 kJ/mol for Cu-Zn [87].

**Table 4.1 - Constants used in calculating grain boundary energies**

	<b>Cu</b>	<b>Zr</b>	<b>Zn</b>	<b>Fe</b>	
Surface Energy $\gamma =$	1.8075	1.9545	0.9915	2.417	J/m <sup>2</sup>
Bulk Modulus $K =$	137.8	89.8	69.4	170	GPa
Shear Modulus $G =$	48.3	35	41.9	81.6	GPa
Atomic Volume $V =$	1.18E-29	2.34E-29	1.52E-29	2.34E-29	m <sup>3</sup> /atom
Molar Grain Boundary Area $\sigma =$	31224.34	49286.31	36969.53	31195.06	m <sup>2</sup> /mol

Using values given in Table 4.1, the model was applied to the Cu-Zr alloys experimentally tested. Figure 4.9 shows the variation in the energy with initial Zr concentration. As the initial solute concentration is increased, the amount of segregant needed on the grain boundary needed for stabilization is reduced. As the temperature is increased, the solute excess required for stabilization increases, and at sufficient temperature (i.e. > 400 °C) complete stabilization is no longer achieved.

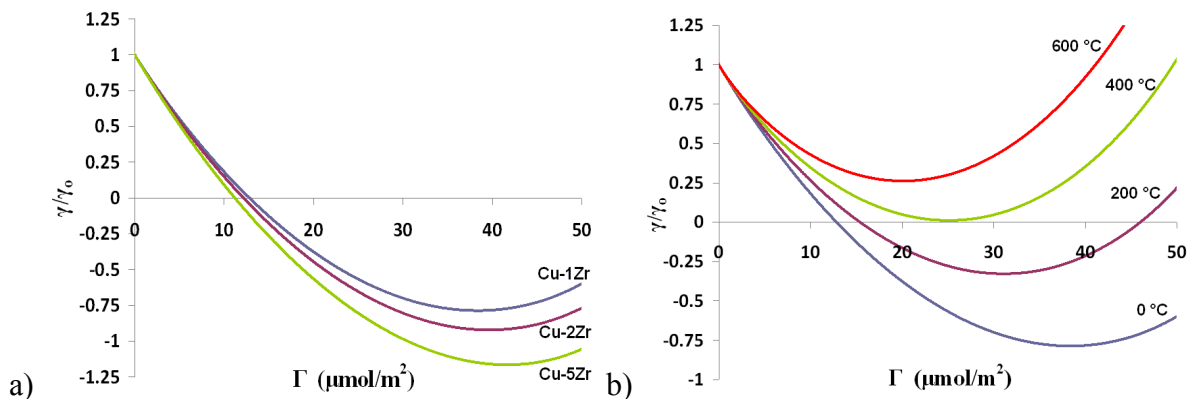


**Figure 4.9 - Normalized grain boundary energy for (a) varying bulk Zr concentrations ( $X_{Zr} = 0.01, 0.02, 0.05$ ) at 273K and (b) for variation in temperature with  $X_{Zr} = 0.01$**

Though the results for variations in stability with temperature and concentration are qualitatively useful, the simplified treatment shouldn't be considered a quantitative treatment. For instance, the stability was found to extend well beyond the calculated 400 °C stability maximum indicated in Figure 4.10. Where this treatment excels is in comparative study. The relative stability of various alloys can be quite instructive. As reported previously [65-67], Fe-Zr alloys have shown very good stability. Therefore, this alloy is used as a benchmark against the current work which has exceeded the Fe-Zr alloys when maximum stable homologous temperatures are compared. Indeed, when plotted together (see Figure 4.10), the relative amount of solute excess for zero boundary energy is less, and the magnitude of energy reduction is greater for the Cu-Zr system. For relative comparison, the Cu-Zn system is also included. The Zn isn't expected to stabilize the copper as brass does not have an inherently stable grain size, and correspondingly, Zn is found to be ineffective as a stabilizing solute even at high concentration (i.e. 30 at%).

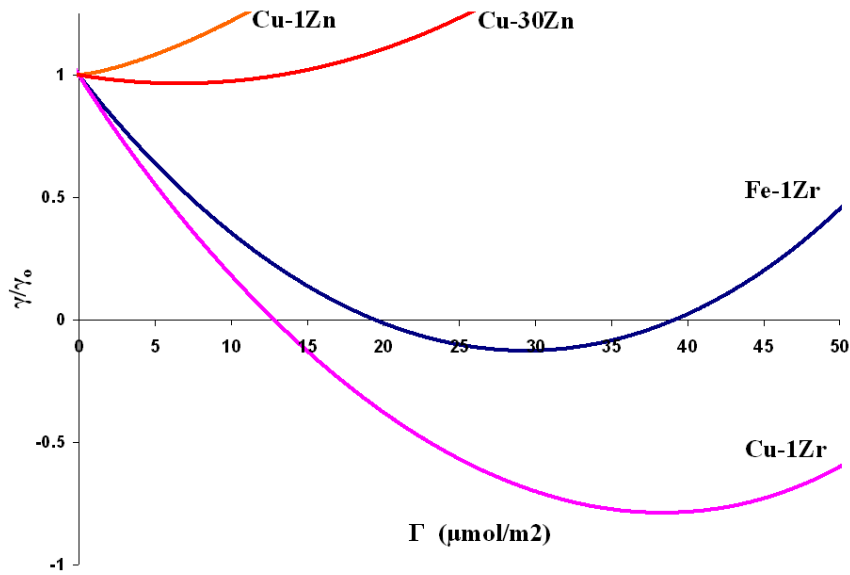


**Figure 4.10 - Comparison of normalized grain energies for various alloy systems**

This treatment ignores intermetallic formation which is likely to occur since Cu and Zr have a negative heat of mixing [88] leading to a variety of equilibrium intermetallics [84, 85, 89]. The best stability was achieved with the lowest Zr concentration and this is thought to be related to intermetallic formation. Intermetallic formation introduces competitive use of the available Zr, and at higher solute levels (e.g. 5 at%) the likelihood that local Zr concentration is sufficient for achieving intermetallic formation is increased. Since the equilibrium intermetallic with the lowest Zr concentration is typically cited to be  $\text{Cu}_9\text{Zr}_2$ , the local concentration must reach  $\sim 18.8$  at% Zr [84]. However, the major intermetallic phase was identified as  $\text{Cu}_5\text{Zr}$  (by Xpowder software) which is metastable at room temperature [90], though repeatedly reported there [91-94]. The formation of intermetallics could add additional stabilization by Zener pinning [10, 41], and even with only 1% Zr there appears to

be significant presence. The effect of precipitates may contribute to a thermokinetic stabilization mechanism as described by Chen *et al.* [71].

The major factor distinguishing the room temperature milled alloys from the cryo-milled alloys is the as-milled hardness. At 1% Zr, the room temperature-milled alloy was much softer. At 2% Zr, both milling conditions were similar. After Zr content was increased to 5%, the room temperature-milled alloy was harder. This is expected to be linked to the intermetallic formation as seen in Figure 4.4 where the SAD pattern for Cu5Zr-RT has obvious intermetallic rings and that for Cu5Zr-C does not. The intermetallic formation during milling, though still not extensive, seems to be most important to stability as the Zr content increases, causing lower overall annealed hardness and larger grain size. The intermetallic formation is expected to be limited in the 1% Zr alloys as found by TEM, and further study of the presence and importance of intermetallics is currently underway.

Cu-Zr alloys have been of interest primarily due to the unique binary bulk glass forming properties [81, 82], and much of the literature is based on this aspect. Cu-Zr alloys been studied for use as high strength, high conductivity alloys in concentration up to ~0.73 at% Zr [83, 95]. The annealing behavior found in [83] is similar to this work where a hardening effect which increases with increasing Zr content is seen at low temperature and is lost by 500-600 °C. The hardening is associated with precipitate formation which is reported to be significant, but with a much larger grain size (~500 nm). Solute segregation effects on grain boundary strength may be partly responsible for the hardening [26, 75, 96], and Zr is

expected to increase grain boundary cohesion [97]. Saarivita [95] also reported precipitation occurring at concentrations above 0.15%, but again not at nanocrystalline grain size. Recently the solid solubility of Zr in Cu (up to ~4.3 at%) was studied by planetary ball milling [98], and not surprisingly Zr was found to dissolve in quantities much greater than equilibrium. When added in dilute quantities, Zr has been found to stabilize 300 nm Cu grains to at least 350 °C (0.17% Zr) [94] and to 500 °C for 100 nm grains (0.18%) [92]. Such a low concentration is believed to be insufficient to stabilize a grain size well below 100 nm since the critical solute concentration is proportional to the inverse of the grain size [74]. An addition of 5% Zr to copper was milled with an organic PCA by Morris [99], and found stable to 900 °C, with a loss of stability at 1000 °C as found here, but the stabilization was attributed to the formation of ZrC (with some ZrO<sub>2</sub>) which acted in a solely kinetic fashion by pinning grain boundaries. As ZrO<sub>2</sub> was found to form here also, it may be an effective material for kinetic stabilization. No study of the stabilizing effects of elemental Zr in Cu at temperatures approaching the melting point of Cu was found.

Another point of difference in the RT and cryo processing routes is the effect the PCA has on the powder. Even at concentrations of 0.5 wt% NaCl, the copper was found to agglomerate into large (2-4 mm) particles, and the size of the particles increased with milling time. To suppress the formation of these agglomerations, 1 wt% NaCl was used. This large addition caused the RT alloys to quickly oxidize in air. In a matter of 1 hr or less the powders would darken significantly until a very dark purple was observed. The effect was accelerated for larger zirconium content with Cu<sub>5</sub>Zr-C being the most susceptible. The effect was somewhat

suppressed after annealing, but not eliminated. The possibility of the NaCl reacting with water in the air coupled with the particular affinity for oxygen that Zr possesses may be responsible. Also, the RT alloys, likely have a greater fraction of Zr segregated to the surface in the as-milled condition since the temperature within the milling vial can be 100-350K above ambient [38]. Although the RT alloys do show very good stability, and are inherently simpler to produce, another PCA may be more appropriate though most are organic compounds which result in appreciable contamination of carbon, oxygen, and/or nitrogen [37]. Powder contamination, and not just from a PCA, is a serious concern in mechanical alloying [8], but with the short milling time and suppression of cold-welding, cryogenic milling is one avenue for reducing the occurrence.

## 4.5 Conclusions

Zr is an excellent candidate for stabilizing nanocrystalline Cu when mechanically alloyed at RT using NaCl as a PCA or at cryogenic temperature without a PCA. When Zr is added to Cu in concentrations as low as 1 at%, a nanoscale grain size can be maintained to  $> 0.85 T_m$  for pure Cu. This statement was found consistent with data collected by microhardness, XRD, TEM and SEM (by FIBCCI). Cryo-milled alloys were found to have similar, though slightly superior stability as found by hardness and XRD grain size comparison. This is explained by the suppression of intermetallic formation during milling when processed at liquid nitrogen temperature. Cu-Zr intermetallic formation was found

along with ZrO<sub>2</sub> particles which may add kinetic stability. The thermodynamic stabilization of Cu by Zr was calculated using a modified Wynblatt-Ku model that accounts for grain boundary segregation. When applied in conjunction with other, known systems, the result can be particularly useful. When compared to Fe-Zr, a well-stabilized system, Cu-Zr shows somewhat superior stability, and this is reflected in the experimental results. The ideal alloy content for Zr in Cu was found to be 1 at% based on superior retention of grain size and hardness at high temperature as well as reduced intermetallic formation.

## **5 Stabilization of Brass by Zirconium**

---

---

Nanocrystalline cartridge brass was produced by cryogenic ball milling and subsequently heat treated to a maximum temperature of 800 °C. The grain size was found to be relatively stable in comparison to pure copper and a high hardness was retained up to 600 °C though many grains had grown to larger than 100 nm. When zirconium was added to the brass alloy, the grain size was stabilized near 100 nm even at 800 °C. The hardness was retained above 2.5 GPa for all zirconium alloys to the same temperature where the pure brass dropped significantly. Up to 600 °C the zirconium did not greatly enhance stability. At 800 °C stabilization is believed to be dominated by Zn-Zr interactions and second phase precipitates were observed in XRD and TEM. Thermodynamic modeling of the system using a modified Wynblatt-Ku approach indicates stabilization will not be achieved, and the mechanism may be kinetic. The possible influence of microstructural features on the thermal performance of the brass and brass-zirconium alloys is discussed.

## 5.1 Introduction

Copper with the addition of 30% zinc forms a single-phase, fcc  $\alpha$ -brass [100] which is also known as cartridge brass (UNS designation C26000). This is an important structural material currently employed in a diverse number of areas including radiator cores, locks, hinges, ammunition components, plumbing components, rivets, and more [101]. Nanocrystalline (nc) materials have habitually shown a significant increase in strength over their coarse-grained counterparts generating interest in their use. However, the grain size stability of nc materials is typically poor (some showing grain growth even at room temperature [9]), and the strength drops precipitously with grain growth. For these reasons it was of interest to examine the thermal stability of nanocrystalline cartridge brass and determine the effectiveness of adding zirconium as a grain boundary segregant.

The addition of 1 at% Zr to Cu has been found to stabilize the grain size below 100 nm in excess of 80% of the melting point of pure Cu (see Chapter 4), and this provided the motivation to explore the efficiency of Zr as a grain boundary stabilizer in Cu 30% Zn. Pure brass, as well as alloys with 1% and 5% Zr, were mechanically alloyed using a high-energy ball mill maintained at cryogenic temperature (-196 °C). The nanocrystalline alloys were then annealed to a maximum temperature of 800 °C in intervals of 200 °C. Analysis before and after annealing was carried out using X-ray diffraction, microhardness, and transmission electron microscopy. The Zr addition only significantly improved the hardness and grain size retention at 800 °C where pure brass performed poorly.

## 5.2 Experimental

Elemental powders of copper (Alfa Aesar, 99.9%), zinc (Alfa Aesar, 99.9%) and zirconium (Cerac, 99.7%) were added to a 440 stainless steel vial (Spex SamplePrep) with grade 25, 440 stainless steel ball bearings (Salem Specialty Ball). The ball charge consisted of 17 balls 0.3125" in diameter and 16 balls 0.250" in diameter. The ball to powder weight ratio was maintained at 10:1. All materials were loaded into the vial in an argon atmosphere ( $O_2 < 1$  ppm) and sealed before transferring to the mill with one exception where pure brass was sealed under vacuum. A modified Spex 8000 mixer/mill was used where the powders were milled for 4 hr at liquid nitrogen temperature (-196 °C). Zirconium was added with the copper and zinc in quantities of 1 and 5 at% (these alloys will be referred to as B1Zr and B5Zr respectively). The milled powders were annealed under 2%  $H_2$  (bal. Ar) for 1 hr at temperatures from 200 °C to 800 °C in 200 °C increments in a Lindberg tube furnace into which the samples were inserted once the furnace had stabilized at the appropriate temperature. After annealing, the powders were supported in epoxy and polished. At least 10 Vickers hardness measurements were collected for each annealing condition using a Buelher Micromet II with a 50 g load applied for 12 sec. Error bars for hardness were calculated by standard deviation. X-ray diffraction (XRD) analysis was conducted using a Rigaku DMax/A X-ray diffractometer using Cu K $\alpha$  radiation. Proper alignment was verified before each use using a single crystal silicon standard. Spectra were collected on powder for all alloys except

the in-situ consolidated Zr alloy prepared for TEM (see below). For this alloy, three 3 mm compacts were placed next to each other in a triangular shape and polished flat before collecting each spectrum. The spectra were processed by smoothing (function filter), removing the background, and  $K\alpha_2$  stripping (optimized Rachinger's method) using Xpowder software ([www.xpowder.com](http://www.xpowder.com)). The grain size was estimated using the Scherrer equation [13] applied to the first peak of the pattern. Transmission electron microscopy (TEM) analysis was carried out using a JEOL 2000FX with a beam energy of 200 keV. 1% Zr samples for TEM analysis were prepared by milling the alloy as described above after which room temperature milling was performed for an additional 4 hr. This allowed the powder to consolidate into small 1-3 mm spheres which were then uniaxially pressed in a 3 mm tungsten carbide die to 2.6 GPa and annealed as described above. This hybrid milling condition will be referred to as B1Zr CRT. Pure brass TEM samples were generated by pressing as described above and subsequently annealing the compact. Both sample types were electropolished in 30 vol% nitric acid in methanol at -20 °C in a Tenupol-2 electropolisher and final thinning was performed with a Fischione Model 1010 ion mill. TEM images have basic brightness and contrast adjustments applied to aid in viewing and printing clarity. Scanning electron microscopy (SEM) analysis of pure brass was performed with a Hitachi S3200 to determine porosity. The SEM is equipped with an energy dispersive X-ray spectrometer (EDS) which was used to verify atomic concentrations.

### 5.3 Results

Pure brass was milled under two conditions. In the first, the milling atmosphere was high purity Ar. In the second, the vial was evacuated and sealed before milling. XRD spectra were acquired after each annealing and are shown in Figure 5.1. The peak broadening is significant in the as-milled condition, and the peaks do not sharpen appreciably until 600 °C. After the 800 °C anneal the peaks are shifted to slightly higher angles indicative of a lattice contraction. The brass alloys milled under Ar and vacuum did not show significant differences upon annealing.

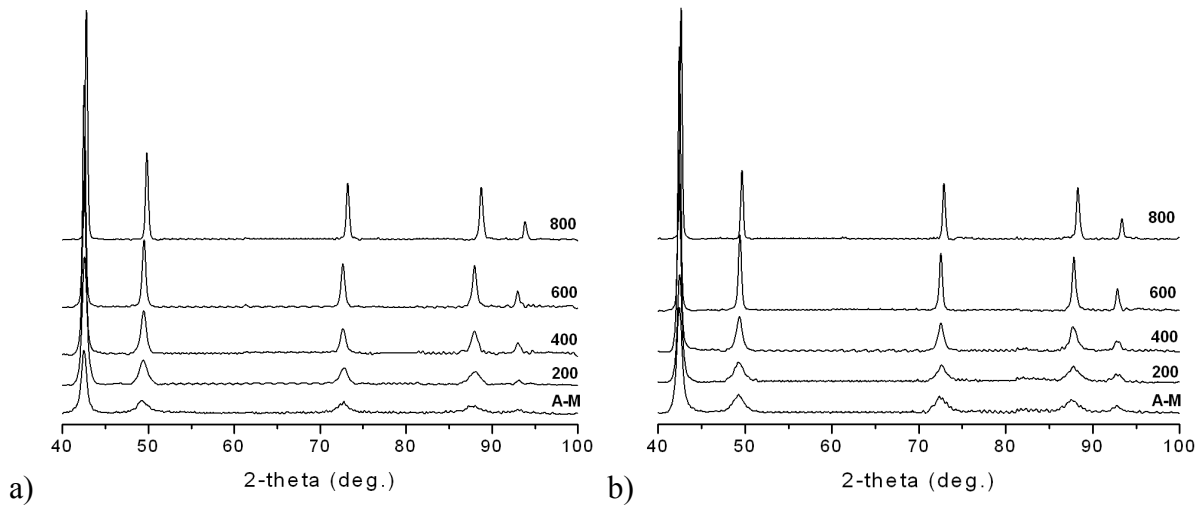


**Figure 5.1 – XRD comparisons for pure brass milled in (a) Ar and (b) vacuum. Annealing temperatures are listed in °C, except for the unannealed (as-milled) condition labeled “A-M”.**

The XRD spectra for the 1% and 5% Zr alloys are shown in Figure 5.2. The appreciable as-milled peak broadening in the 1% Zr alloy indicates a very small grain size, and the peaks sharpen slowly as annealing temperature increases. For the high angle peaks (i.e. 311 and 222), sharp, well-defined profiles do not occur until 600 °C, and are significantly narrowed only at 800 °C. In the 5% Zr alloy, the as-milled condition has a single, extremely broad peak indicative of an amorphous, or at least partially amorphous structure, which is lost by 400 °C. Again, the higher angle peaks do not become clearly distinguishable until 600 °C and are not definitive until 800 °C. At 800 °C, additional peaks between the 111 and 200 peaks become visible and these are associated with  $Zn_3Zr_3O$ , which will be discussed below.

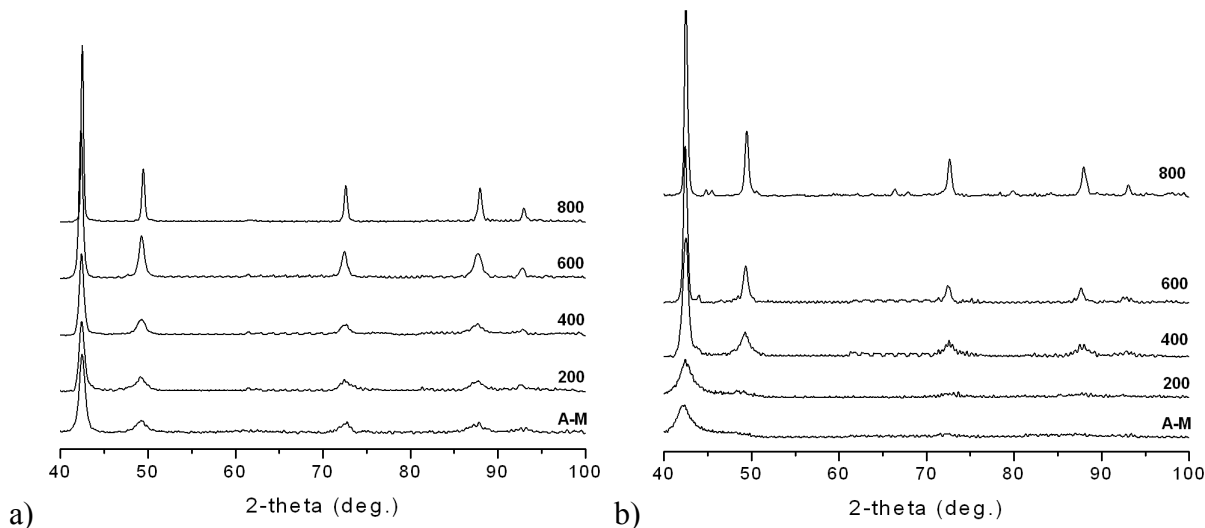


**Figure 5.2 - Post annealing XRD spectra of brass with 1% Zr and 5% Zr additions. Annealing temperatures are listed in °C, except for the unannealed (as-milled) condition labeled “A-M”.**

Based on the above X-ray spectra, it is expected that both pure brass and the brass zirconium alloys will retain a nanoscale grain size up to at least 400 °C, and indeed, by Scherrer grain size estimation (see Figure 5.3) it is reported that both remain below 25 nm at 400 °C (0.55 T<sub>m</sub>) with the Zr alloys retaining such dimensions until 600 °C (0.72 T<sub>m</sub>) for all conditions. Data obtained in previous work [102] for copper alloys with equivalent Zr content are also plotted as a comparison. The Cu-Zr system was found to be remarkably stable, and as shown, the brass zirconium alloys show similar stability when the homologous temperatures are compared. Also of note is that the pure brass indicates superior stability over pure copper (not shown) which exceeded 40 nm by 400 °C. This size has been found to be a typical cutoff for reasonable accuracy when using the Scherrer equation under these conditions. Ar entrapment during milling at 77 K has been noted in previous work [39], and to determine if the processing conditions were of importance in the pure brass stability (i.e. milling in Ar atmosphere), the material was also milled under vacuum. The two conditions are nearly identical until being annealed at 600 °C, but by then both are out of the range of accuracy for XRD analysis though qualitatively similar. The B1Zr CRT sample shows a larger as-milled grain size, but improved stability over samples that were only cryo-milled at higher temperature. The configuration used in collecting X-ray spectra for the B1Zr CRT samples (see experimental section) may lead to anomalous results, but as these were generated specifically for TEM use, the XRD estimation is not considered quantitatively.

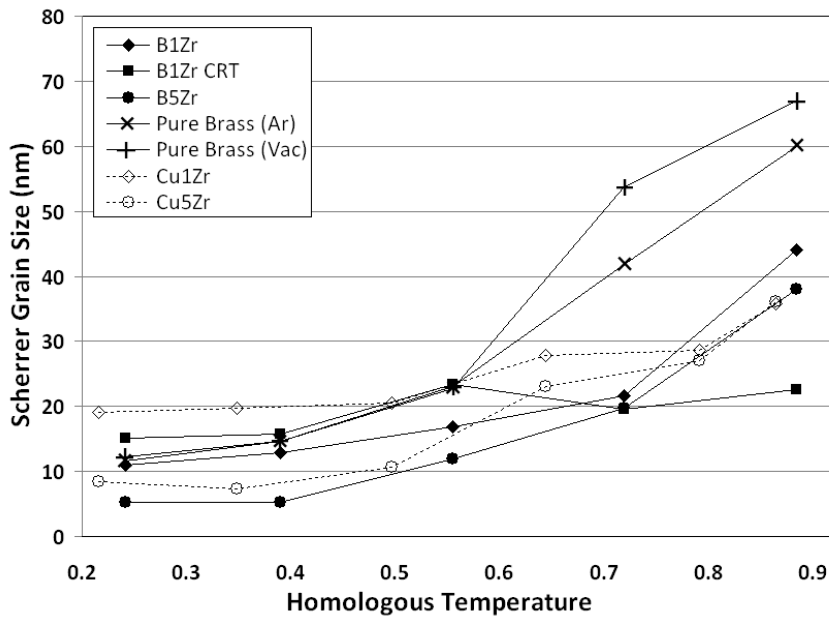


**Figure 5.3 - Comparison of XRD grain size estimates. Cu-Zr data is added from [102].**

The microhardness values of the alloys are shown in Figure 5.4. All of the alloys are close in as-milled hardness, but when annealed at 200 °C the cryo-only Zr alloys harden, with the 5% Zr alloy hardening quite significantly. The pure brass alloys are quite close in hardness throughout the annealing range, with separation increasing at 600 °C analogous to the XRD grain size estimates. These pure alloys retain hardness remarkably well, with the Zr additions being truly beneficial only at the highest temperature. The B1Zr CRT alloy showed delayed hardening compared to the cryo-only alloys, and was hardest after a 400 °C anneal. At all other temperatures the B1Zr CRT alloy was softer than the corresponding, cryo-only alloy, though only by a small margin (averaging < 0.25 GPa) and typically within error.

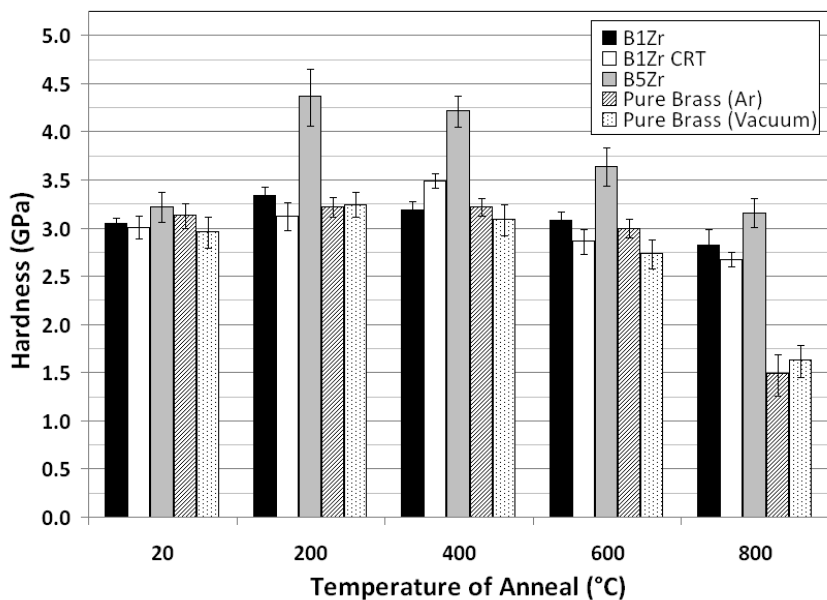


**Figure 5.4 – Measured hardness values for the brass and brass-Zr alloys**

TEM analysis was conducted to determine grain size more accurately. The results for the B1Zr CRT alloy after annealing at 800 °C are shown in Figure 5.5. The selected area diffraction (SAD) inset of Figure 5.5a shows major rings corresponding to  $\alpha$ -brass (fcc) structure. These are accompanied by two inner rings attributed to a second phase (more on this below). The dark field image corresponding to the brass rings (Figure 5.5d) reveals that the material is primarily made up of grains near 100 nm. The volume and number average grain sizes are 121 nm and 105.7 nm respectively. Greater than 70% (by number) of the grains are 120nm or less. The second phase particles in Figure 5.5c have volume and number averages of 10.8 nm and 7.4 nm respectively with 48.4% being 5 nm or less and 26.9% between 5 nm and 10 nm. The inner rings in Figure 5.5a were very weak for the alloy when annealed at 600 °C.

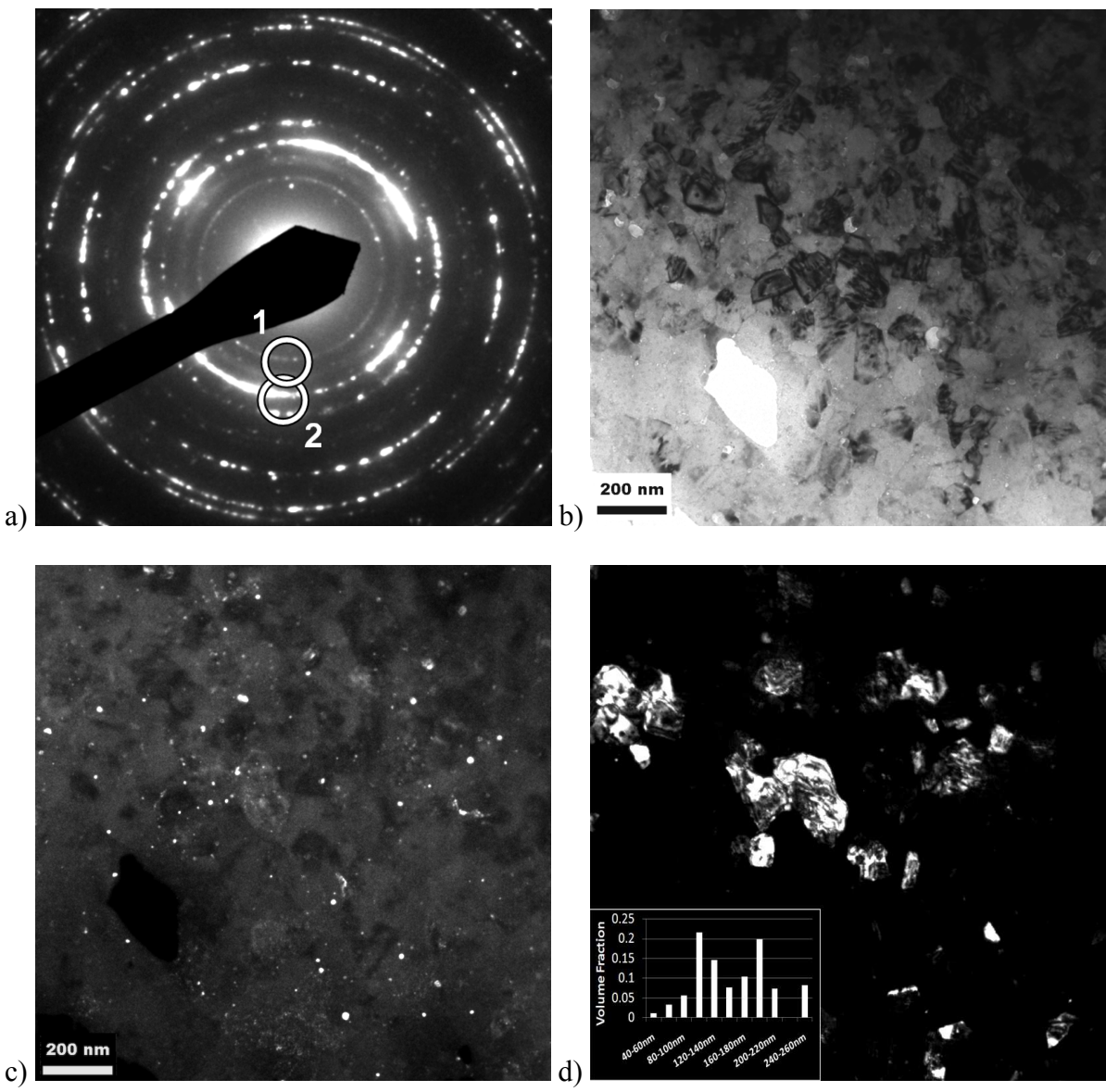


**Figure 5.5 – B1Zr CRT after annealing for 1 hr at 800 °C** (a) SAD pattern with objective aperture positions indicated for inner rings (position 1) and 111 and 200 brass rings (position 2). Bright field image is shown in (b) and dark field images are shown corresponding to (c) objective aperture position 1 and (d) objective aperture position 2 with volume fraction grain size inset lower-left. Scale bar equivalent for bright and dark field images.

The TEM of pure brass (see Figure 5.6) confirmed that the alloy remained nanoscale even at 600 °C. The SAD pattern inset for Figure 5.6a shows the grain size to be quite small and also reveals faint extra rings which correspond to ZnO. The volume and number average grain sizes 74.3 nm and 66.7 nm respectively and grain size distribution is more tightly bound than B1Zr CRT at 800 °C with 69.0% of the grains being between 40 nm and 80 nm. A summary of the dark field grain size results are listed in Table 5.1.

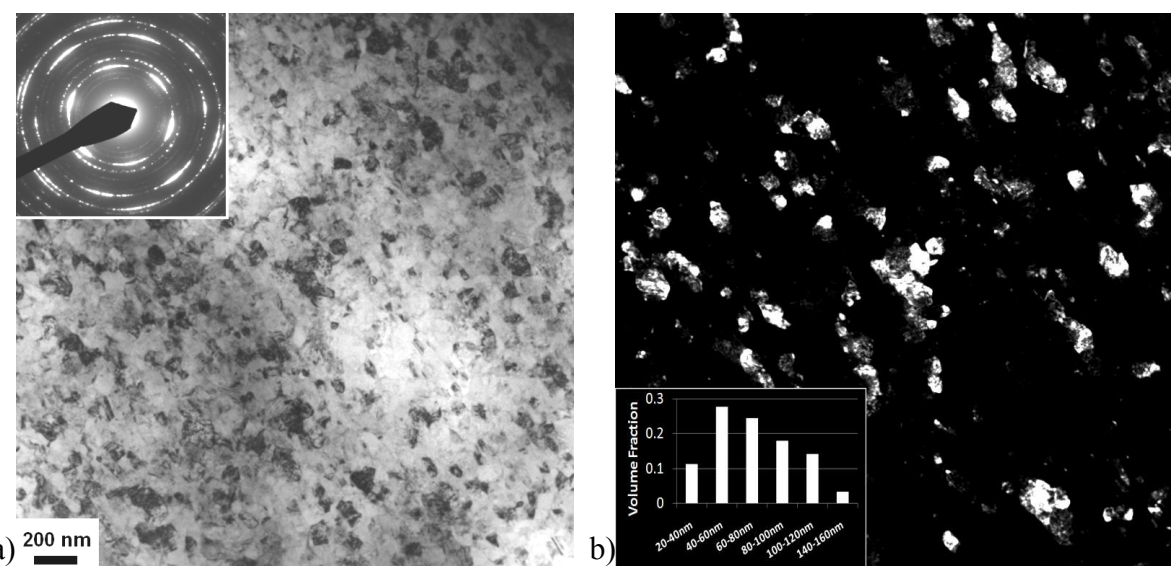


**Figure 5.6 – TEM results for pure brass milled in Ar and annealed at 600 °C for 1 hr (a) bright field with SAD pattern inset at upper-left and (b) corresponding dark field image with volume fraction grain size inset lower left. Scale bar in bright field image valid for both images.**

**Table 5.1 - Dark field grain size results for pure brass and 1% Zr alloy (B1Zr CRT)**

Annealing Temperature	1% Zr		Pure	
	Volume Average	Number Average	Volume Average	Number Average
As-Milled	17.5	10.9	32	17.9
600	73.4	64.2	74.3	66.7
800	121	105.7	-	-

## 5.4 Discussion

### 5.4.1 Pure Brass

Nanocrystalline cartridge brass was found to retain remarkable hardness at annealing temperatures up to 600 °C and it was found that the grain size is well-stabilized for a “pure” material. The vacuum-milled brass was used to determine if Ar entrapment during milling may have affected the properties of the corresponding alloy which could have manifested by grain boundary pinning due to porosity [80] or additional lattice strain. By SEM examination of the powders (not shown), it was found that the Ar-milled alloy did contain significantly more porosity after annealing at 800 °C although the vacuum-milled alloy also contained some. Their annealing behavior, evidenced through hardness and XRD grain size estimation, is quite similar and it is expected that the Ar environment is not responsible for the retention of properties.

As Zn content increases in  $\alpha$ -brass the stacking fault energy (SFE) decreases [103], and in addition to stacking faults, cartridge brass is known to contain microstructural features such as twinning [17, 104] and short-range ordering [105-107] which can increase strength. When plotted using the Hall Petch constants of  $\sigma_0 = 45.11$  MPa and  $k = 0.31$  MN/m<sup>3/2</sup> [17], the experimental hardness is below the calculated line, but in agreement with other data utilizing severe plastic deformation techniques [108]. Besides grain size strengthening, there are other contributing factors that determine the strength of pure brass and possibly play a role in retaining the hardness after annealing. Anneal hardening that occurs below the

recrystallization temperature, is controlled by solute segregation to dislocations and has been reported in copper single phase solid solutions [109-111]. Depending on the degree of the prior cold-work, anneal hardening causes a peak in hardness in the range of 200-300 °C and may have an effect on the hardness of annealed brass. It is important to note that formation of annealing twins is reported to produce an anomalous hardening in Cu and Ni after annealing [112]. Also, as Zn content is increased the annealed strength of  $\alpha$ -brass increases [104].

Twinned microstructures in Cu [113, 114] and Cu-based alloys [115, 116] are well-known to show high strength in the as-processed state (i.e. prior to annealing). Twinning is more likely for low SFE materials, low temperature and high strain rates, but somewhat suppressed as grain size is reduced [17]. Twinning in nanocrystalline materials is a complex process and the topic has been reviewed by Zhu et al. [117] recently. As the grain size is reduced below 100 nm, deformation twinning is frequently observed even in materials with a relatively large SFE [117]. An inverse grain size effect on twinning has been observed where the propensity for twinning reaches a local maximum within the nanoscale regime and then begins to decrease again in Ni [118] and Cu [119] which have stacking and general planar fault energy differences great enough to indicate the effect is a common phenomena [117].

Cryogenic ball milling (low temperature, high strain rate) is likely to generate a high deformation twin density in coarse-grained materials, but the grain size effect eliminates easy assumptions about the result on nanocrystalline brass. In the case of Cu-30%Zn, Miura et al. [120] reported that cryo-rolling and subsequent annealing (up to 270 °C) resulted in an

ultrafine-grained microstructure decorated with deformation and annealing twins. A nanotwinned microstructure in Cu is also shown to have enhanced thermal stability when twin density increases [121]. Saldana et al. [121] discussed that twin boundaries retard migration of grain boundaries and triple junctions. For ultra-fine grained samples produced by equal-channel angular pressing (ECAP) others [92, 122] have found weakening and grain growth to commence nearer to 250 °C in  $\alpha$ -brass with copper being lower in both cases. In both studies the ECAP was performed at or above room temperature. Cryogenic severe plastic deformation of low SFE brass (SFE = 14 mJ/m<sup>2</sup> [123]) with high energy ball milling involves multi-directional forces that facilitate twinning in the microstructure. Therefore, the presence of a high density of thermally stable deformation twins together with annealing twins that nucleate and grow upon annealing may account for the retained hardness and grain size of pure brass. The resolution capabilities of the TEM used in this work negated the ability to properly interrogate nanoscale twinning, though larger twins were prevalent.

#### **5.4.2 Brass-Zirconium**

Zirconium has been found to stabilize a number of nanocrystalline materials such as Pd [48, 124], Fe [66, 67], and Cu [83, 92, 102]. A strong elastic misfit component (elastic enthalpy of ~72 kJ/mol in cartridge brass) drives segregation to boundaries where the Zr can be active in reducing the grain boundary energy by thermodynamic means. Though the elastic enthalpy is lower than in Cu or Fe (> 90 kJ/mol), the solid solubility of Zr in either Cu or Zn is negligible [84, 85, 125-127] and substantial segregation is expected. Others [92] have found

brass to benefit somewhat less than Cu from Zr addition in UFG materials, but the Zr content was significantly less than used here (0.13% and 0.18% respectively).

The brass-Zr alloys provide a somewhat more challenging analysis compared to binary systems with regard to grain size stabilization mechanisms and the role of intermetallics. Zirconium forms a variety of binary intermetallics with both copper [84, 85] and zinc [125-127] in addition to the ternary intermetallics  $\text{Cu}_2\text{ZnZr}_3$  [128],  $\text{Cu}_2\text{ZnZr}$  [129], and  $\text{Cu}_7\text{Zn}_{16}\text{Zr}_6$  [130]. TEM SAD results indicate that there is second phase formation in the B1Zr CRT alloy (see Figure 5.5), but for the 1% Zr alloy, the formation of a second phase was below detection limits using XRD at any annealing temperature. The presence but limited extent of precipitation indicates that the stabilization mechanism is likely thermokinetic [71] in nature where both thermodynamic stabilization (grain boundary energy reduction) and kinetic stabilization (grain boundary mobility reduction) are in cooperation, though the thermodynamic mechanism is expected to dominate. In this, some of the added Zr can be active in reducing grain boundary energy while some is active through kinetic means such as solute drag or grain boundary pinning. The thermokinetic treatment in [71] deals more specifically with solute drag, but the most effective kinetic mechanism present in these alloys is likely Zener pinning since the precipitates tend to be quite small [10].

A variety of peaks not associated with pure brass developed at high temperature for the 5% Zr alloy. Identification of these was best fit by  $\text{Zn}_3\text{Zr}_3\text{O}$  using XRD data (see Figure 5.7). The calculated peaks of  $\text{Zn}_3\text{Zr}_3\text{O}$  are largely consistent with the additional peaks but are

shifted to lower angles indicating an expanded lattice parameter which may arise due to a non-stoichiometric composition. With the limited pattern library available in the X-ray software for the alloy, there may be a phase with a better fit, but it is also likely a mixture of intermetallics. The important feature is that there is a significant presence of second phase particles.

An oxide phase need not form during annealing (clear evidence of oxidation after annealing was not visibly observed) but may arise by simple exposure to ambient air as zinc and zirconium have strong affinities for oxygen. Oxygen may also be incorporated before or during milling that is not removed during annealing. The equimolar intermetallic ZnZr may be the precursor for oxide phase, and thermodynamically, its enthalpy of formation is the most energetically favorable for any equilibrium Zn-Zr intermetallics [131]. Oxidation of B1Zr CRT specimen during annealing is unlikely to appear in the TEM sample since hundreds of microns of material are removed from both surfaces of the consolidated compact before electropolishing and ion milling and no oxidation was visibly apparent even on the surface of the compact. Alloys milled at room temperature are known to form intermetallics suppressed under cryo-milling conditions [102], and it is possible that some oxidation occurred during the milling that lead to  $Zr_3Zn_3O$  formation.

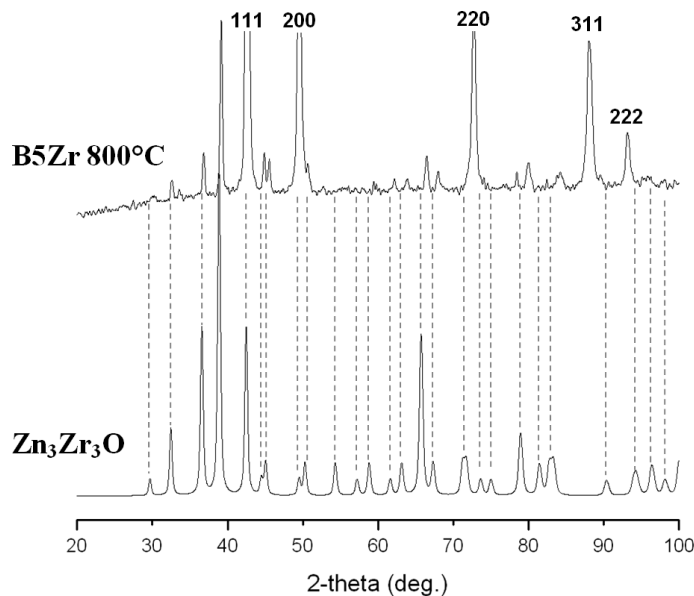


**Figure 5.7 - Comparison of experimental XRD pattern for B5Zr after 800 °C anneal and the calculated pattern for  $\text{Zn}_3\text{Zr}_3\text{O}$ . Dashed lines are associated with the calculated pattern peaks. Brass peaks are labeled with corresponding reflections.**

As Zr content and/or temperature increases, the likelihood of surface segregation also increases which may promote oxide formation. Identification of the major phase as  $\text{Zn}_3\text{Zr}_3\text{O}$  doesn't preclude other minor phases from being present as well. Equilibrium Zn-Zr intermetallics form at a lower Zr concentration (4.3% [126] to 6.7% [125, 127] Zr) than those in the Cu-Zr system (18.2% Zr [84, 85]). To contrast with earlier findings [102], XRD results for Cu-Zr alloys did not show intermetallic peaks even for the 5% Zr alloy when annealed to 1000 °C, and the major phase identified there,  $\text{Cu}_5\text{Zr}$ , is not present in the brass system. A further observation for the brass alloys is that when pure, annealing at 800 °C caused significant dezincification as found by EDS analysis (a loss of ~5% and 1% for the Ar-milled and vacuum-milled alloys respectively). This is also evidenced by a peak shift in the XRD

spectra (Figure 5.1) which is not seen in the Zr alloys (Figure 5.2) possibly due to Zn-Zr interaction. For these reasons it is expected that grain boundary and surface interactions are primarily between Zn and Zr.

The possibility of thermodynamic stabilization can be obtained using an approximation based on a modified Wynblatt-Ku approach [64] which is discussed in Section 2.3.2.1. The plots of normalized grain-boundary energy  $\gamma/\gamma_0$  vs. grain-boundary solute excess  $\Gamma$  shown in Figure 5.8 correspond to the limit  $T = 0$  K and infinite grain size. If these do not intersect zero ( $\gamma/\gamma_0 = 0$ ) then thermodynamic stabilization is not possible under any conditions [64]. The input parameters needed are the size misfit elastic energy change  $\Delta E_{el}$  and the liquid equimolar enthalpy of mixing  $\Delta H_m$ . The former is obtained from the Friedel - Eshelby analysis [63], while the latter is experimental data if available, or model calculations [86]. The surface energies [132],  $\gamma_s$ , of the solvent and solute also make a small contribution. The values used for Figure 5.8 are given in Table 5.2. Values not listed in a reference were calculated using a weighted average value from data in the respective references.

**Table 5.2 - Material constants used in thermodynamic calculations. Values for brass were a weighted average of Cu and Zn values.**

Solute - Solvent	$\gamma_s^{\text{solute}}$ (J/m <sup>2</sup> )	$\gamma_s^{\text{solvent}}$ (J/m <sup>2</sup> )	$\Delta E_{el}$ (kJ/mol)	$\Delta H_{\text{mix}}$ (kJ/mol)
Zr - brass	1.9545 [49]	1.5627	71.75	-19.9
Zr - Cu	1.9545 [49]	1.8075 [49]	91.35	-16 [48]

Figure 8a indicates that additions of Zr up to 10% will have no effect on thermodynamic stabilization of the grain size. The experimental hardness results being equal for B1Zr at 600 °C (minimal second phase present) indicate that Zr is not effective for thermodynamic stabilization of brass. The increased hardness and grain size stabilization observed at 800 °C for the B5Zr alloy indicate that kinetic contributions due to second phase particles are effective. Figure 8b compares B1Zr with Cu1Zr. The latter shows a strong trend for thermodynamic stabilization and this was the case for the results reported in [102]. Although the thermodynamic model is simplified to the limits stated, and to the extent that brass is treated as a single (weighted average) component, the model predictions agree qualitatively with the experimental results obtained for the brass-Zr here and Cu-Zr in [102].

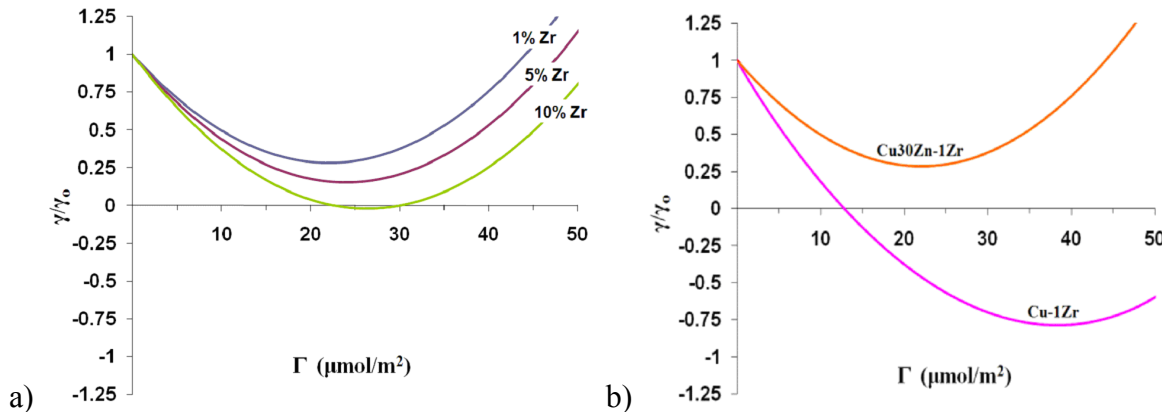


**Figure 5.8 - Thermodynamic model of (a) concentration effect of Zr in brass, and (b) brass and Cu with 1 Zr**

## 5.5 Conclusions

Nanocrystalline cartridge brass produced by cryogenic ball milling showed significant stability for being a “pure” material. There are a variety of microstructural possibilities in a low SFE material like cartridge brass, and retention of the grain size and hardness is likely at least partially attributed to these and not merely a grain size effect. When zirconium was added in an amount as small as 1%, the grain size could be stabilized near 100 nm to 800 °C which is ~88% of the melting temperature of brass. The hardness was also well-maintained at these temperatures. Zn-Zr interactions are dominant in the system, and  $Zn_3Zr_3O$  was identified as a second phase precipitate after annealing at 800 °C though additional phases are likely present in minor quantities. Thermodynamic modeling using a modified Wynblatt-Ku approach predicts increased, but not total stability in the system. The presence of a finely dispersed second phase at high temperature is expected to introduce a significant kinetic contribution to the stability.

## ***6 Stabilization of Copper & Brass by Antimony***

---

---

Nanocrystalline copper and brass (30% zinc) were generated by cryogenic, high-energy ball milling. Antimony was added to investigate its usefulness in stabilizing the grain structure during annealing up to a maximum temperature of 800 °C. Nanocrystalline copper alloyed with antimony in quantities up to 5 at% was found to have improved stability up to 400 °C, but nanocrystalline brass alloyed to the same level performed similarly or worse than when pure. Thermodynamic evaluation indicates antimony should be beneficial when available as an excess boundary concentration, but this is complicated by the appreciable solubility of antimony in copper which reduces or eliminates a truly excess concentration at boundaries.

### **6.1 Introduction**

In previous reports [96, 133, 134], antimony (Sb) was found to enhance the grain size stability and strength of copper (Cu) when added in dilute quantities. The effect on ultra-fine grain (UFG) Cu was studied experimentally [96] by deforming the alloys via equal channel angular pressing (ECAP) to a grain size of 350 nm. Grain growth onset was found at 250 °C for pure copper, and 400 °C for the Cu-Sb alloys indicating a stabilizing effect. However, the

effect was found by MD simulation [96, 134] to be much more profound in nanocrystalline Cu where the grains were found to be stable during accelerated annealing at 1200K (927 °C) for a concentration of only 0.5% Sb. Based on this it was of interest to study the stability experimentally.

To generate the nanocrystalline Sb alloys, cryogenic, high-energy ball milling was used. Alloy compositions of 0.5, 1, and 5% Sb were studied. In addition to pure Cu, an  $\alpha$ -brass alloy (copper 30% zinc) was also studied as the matrix material. The alloys were annealed to a maximum of 800 °C in 200 °C increments. Analysis was then conducted by x-ray diffraction, microhardness, and optical and electron microscopy. The results of these methods indicate that the stability of the materials is not significant, and is comparable to the undoped materials.

## 6.2 Experimental

Elemental powders of copper (Alfa Aesar, 99.9%), zinc (Alfa Aesar, 99.9%) and antimony (Alfa Aesar, 99.999%) were added to a 440 stainless steel vial (Spex SamplePrep) with grade 25, 440 stainless steel ball bearings (Salem Specialty Ball). The ball charge consisted of 17 balls 0.3125" in diameter and 16 balls 0.250" in diameter. The ball to powder weight ratio was maintained at 10:1. All materials were loaded into the vial in an argon atmosphere ( $O_2 < 1$  ppm) and sealed before transferring to the mill. A modified Spex 8000M

mixer mill was used where the powders were milled for 4 hr at liquid nitrogen temperature (-196 °C). Antimony was added with the copper (or copper and zinc (Zn) for brass alloys) in quantities of 0.5, 1 and 5 at%. The Cu-Sb alloys will be referred to as Cu0.5Sb, Cu1Sb and Cu5Sb respectively. Brass-Sb alloys will be referred to as B0.5Sb, B1Sb and B5Sb respectively. The milled powders were annealed under 2% H<sub>2</sub> (bal. Ar) for 1 hr at temperatures from 200 °C to 800 °C in 200 °C increments in a Lindberg tube furnace into which the samples were inserted once the furnace had stabilized at the appropriate temperature. The hardness of the polished alloys was determined by no less than 10 Vickers hardness measurements collected using a Buelher Micromet II with a 25 g load applied for 12 sec. Error bars for hardness were calculated by standard deviation. X-ray diffraction (XRD) analysis was conducted using a Rigaku DMax/A X-ray diffractometer using Cu K $\alpha$  radiation. Proper alignment was verified before each use using a single crystal silicon standard. The spectra were processed by removing the background and K $\alpha_2$  contribution (optimized Rachinger's method) using Xpowder software ([www.xpowder.com](http://www.xpowder.com)). The grain size was estimated using the Scherrer equation [13] applied to the first peak of the pattern. Transmission electron microscopy (TEM) analysis was carried out using a JEOL 2000FX with a beam energy of 200 keV. Samples for TEM analysis were prepared by electropolishing in 30 vol% nitric acid in methanol at -20 °C in a Tenupol-2 electropolisher then finishing with ion-milling in a Fischione Model 1010. TEM images have basic contrast and brightness adjustments made. Scanning electron microscopy (SEM) analysis was performed with a Hitachi S3200 equipped with an energy dispersive X-ray spectrometer

(EDS) which was used to determine atomic concentrations. Optical microscopy was performed using a Nikon Epiphot 300 microscope equipped for digital imaging.

### 6.3 Results

As a first method of analysis, XRD was used to collect spectra of the alloys. The 5% Sb alloys are shown in Figure 6.1 throughout the annealing range. The 5% alloys were chosen since they alone show intermetallic formation (at least B5Sb), and as will be demonstrated below, also have the greatest stability. Aside from the intermetallic formation, the as-milled peak broadening indicates an amorphous or nearly amorphous structure, and particularly unexpected is the increase in peak broadening both alloys demonstrate at 800 °C though most pronounced in the Cu-Sb alloy.

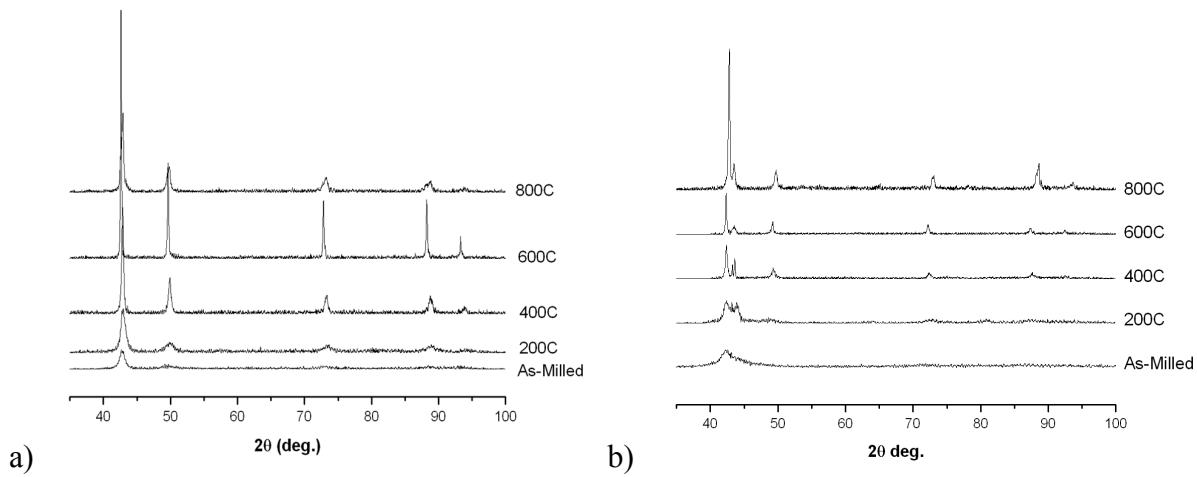


Figure 6.1 - XRD spectra for 5% Sb alloys of (a) copper and (b) brass

The XRD spectra were used for grain size estimation using the Scherrer equation. The grain size estimates based on this treatment are shown in Figure 6.2. As can be seen, the grain size increases quickly at 400 °C for both sets of alloys, and the stability is estimated to be comparable to the pure materials for both the Cu and brass alloys. The upper limit of reasonable accuracy is approximately 40 nm under these conditions, and any grain size reported to be larger has a high likelihood of being much larger than the predicted size. As mentioned in regard to the peak broadening observed in Figure 6.1, the grain size is estimated to be smaller at 800 °C for the Cu<sub>1</sub>Sb and Cu<sub>5</sub>Sb alloys as well as for the B<sub>5</sub>Sb alloy. Pure Cu also shows a similar behavior.

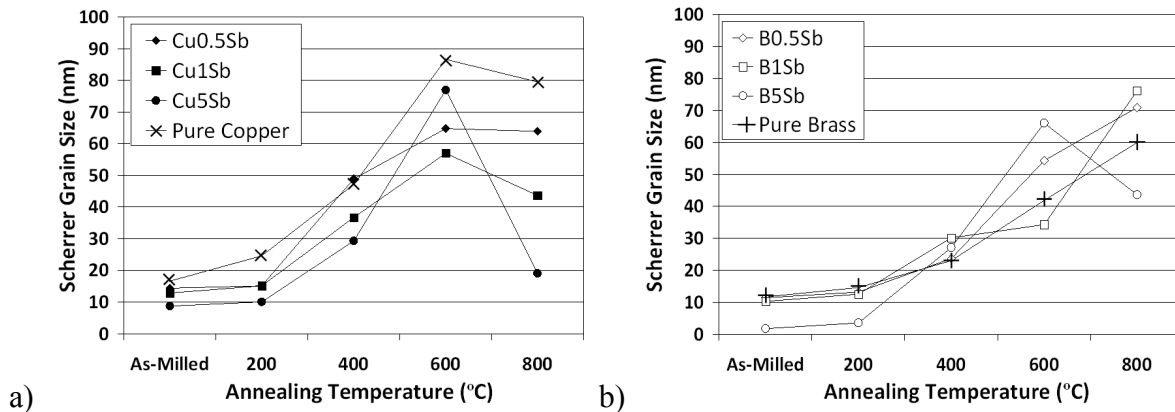
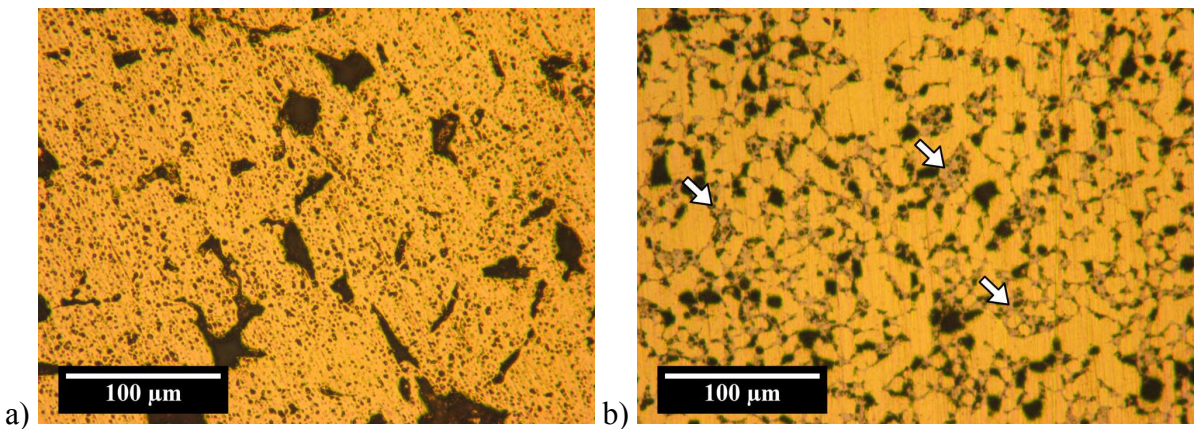


Figure 6.2 - XRD grain size estimation using the Scherrer equation for (a) Cu-Sb alloys and (b) brass-Sb alloys

The apparent grain size reduction is not only unexpected, it is difficult to justify. During annealing, compacted samples were found to expand and loose powder samples to become quite porous within the particles which may cause anomalous broadening if on a uniform and

fine scale. The fact that the grain size reverses only at 800 °C makes it highly unlikely that the grain size is indeed small since the Cu<sub>5</sub>Sb alloy is in the 2-phase liquid-solid region of the phase diagram [135]. No confirmation of a nanoscale grain structure was found when using focused-ion beam ion channeling contrast and resolvable porosity was not sufficient to be the cause either. As the cause of this behavior is not critical to the grain size stability, any additional effort into identifying the phenomenon was decided against.

In regard to the expansion, this behavior has been observed previously when milling in Ar at liquid nitrogen temperature [39]. Given this propensity in concert with the deep eutectic produced by the antimony addition [135], the conditions are ideal for generating a metallic foam at low temperature. Evidence that this was the case was sought by optical microscopy and the results are shown in Figure 6.3. After annealing the compacted materials at 600 °C for 1 hr, both samples were highly porous with densities of ~60% (as-compacted densities were ~90%). For the Cu<sub>5</sub>Sb alloy (Figure 6.3a), the porosity within particles is extensive. The B<sub>5</sub>Sb alloys (Figure 6.3b) shows an apparent second phase separating out at particle boundaries as indicated by the arrows in the image.



**Figure 6.3 - Optical images of (a) Cu<sub>5</sub>Sb and (b) B<sub>5</sub>Sb after being compacted, annealed at 600 °C for 1hr and polished. Arrows indicate a possible second phase between particles.**

A more detailed investigation of the B<sub>5</sub>Sb alloy annealed at 600 °C was sought by SEM examination. The phase separation is clearly observable in the micrograph in Figure 6.4. This interparticle phase (position 1 in Figure 6.4) was found to be extremely rich in Sb and slightly enriched in Cu as opposed to the particles (position 2 in Figure 6.4) which tended to be depleted of antimony and slightly Zn rich. Also, there was lamellar precipitation visible in many particles such as that just above position 2 in Figure 6.4 which has been studied for similar concentrations of Sb in Cu [136]. The EDS results were qualitatively consistent at other locations, and though not an absolute method of measurement, there is good indication that the antimony strongly segregates to particle boundaries and surfaces. The same segregation was not seen optically after annealing at 400 °C in the B<sub>5</sub>Sb alloy, and was not observed at all in the Cu<sub>5</sub>Sb alloy.

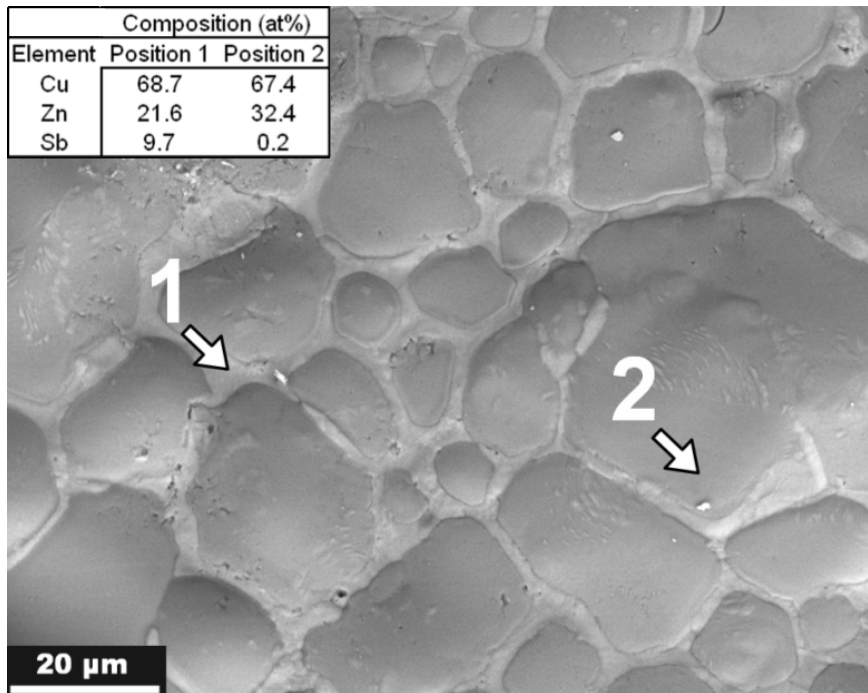
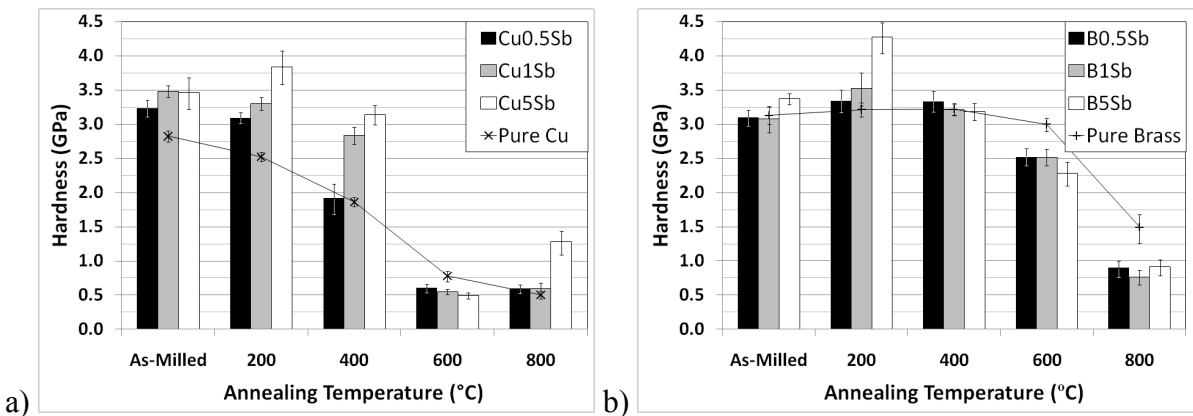


**Figure 6.4 – Backscattered electron image of B5Sb alloy compacted then annealed at 600 °C for 1 hr with compositional results based on EDS data collected at the points indicated inset top-left.**

The hardness of each alloy was determined after annealing, and the results are shown in Figure 6.5. The Cu0.5Sb alloy drops in hardness significantly at 400 °C with the 1% and 5% alloys following suit at 600 °C. Though no anneal hardening occurs in the Cu0.5Sb or Cu1Sb alloys, the Cu5Sb samples does show an increased hardness at 200 °C. All of the brass-Sb alloys showed hardening with low temperature annealing. As a system, the brass alloys maintained a higher hardness at 600 °C, but brass alloys have been found to do the same even when pure [137]. At their highest hardness, both alloy systems were prone to cracking during indentation and required numerous indentations before 10 reliable indents could be obtained.

Somewhat anomalously, the hardness of the Cu<sub>5</sub>Sb sample increases after annealing at 800 °C. This is in agreement with the results in Figure 6.2a where the grain size is reported to drop which would also increase hardness. However, the hardness is expected to be significantly higher if the grain size returned to the nano regime. It is instead believed that an increase in density caused by entrance of the alloy into the 2-phase solid-liquid region (based on equilibrium phase diagram [135]) is more likely the cause. As expected, the hardness of porous alloys will be underrepresented. This is particularly troublesome if the porosity is unresolved in the hardness tester. Samples where porosity was present in these results are those containing 1% or greater Sb and at temperatures of 600 °C and above as well as pure Cu and brass at 800 °C. Though nanoindentation could be used to resolve this issue and increase accuracy, in regard to stability, the susceptible alloys and problem temperatures are not seen to be of technological importance for this work. Though there may well be other applications for the alloys, they are ineffective at grain size stabilization which is of principal importance here.



The conditions of maximum stability were examined using TEM. This condition was identified as that where the hardness first dropped considerably and where the XRD grain size estimation exceeded 40 nm. For Cu0.5Sb, this annealing temperature was 400 °C. As shown in the inset of Figure 6.6a, the SAD pattern is somewhat discontinuous and there is a faint contribution from a second phase. Dark field (Figure 6.6b) shows the grain size to be varied, but generally close to 100 nm. The volume average grain size is 62.5 nm and the number average is 55.0 nm.

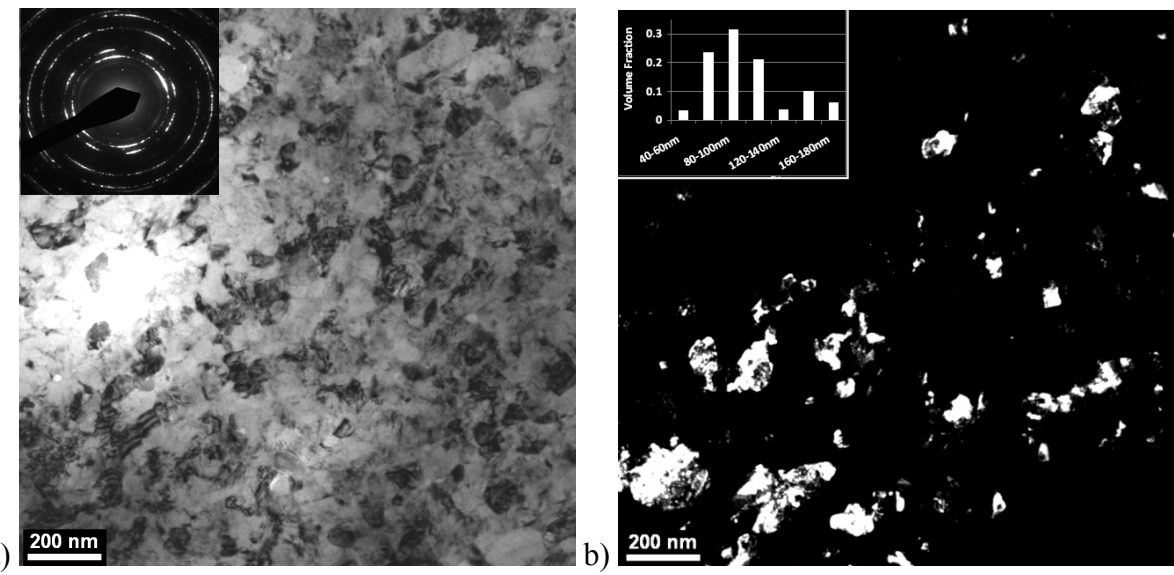


**Figure 6.6 - TEM images of Cu0.5Sb annealed at 400 °C using (a) bright field with inset SAD pattern, and (b) corresponding dark field with inset grain size histogram**

For the B0.5Sb alloy the temperature of interest was 600 °C. As seen in Figure 6.7a, for this condition the SAD rings are extensively broken up and also contains a faint second phase contribution. The grain size is larger than that of the Cu0.5Sb alloy, but the annealing temperature is also higher. The volume average grain size is 89.2 nm and the number average is 80.6 nm. This grain size is actually larger than reported for pure brass under identical conditions where the averages were 74.3 nm and 66.7 nm respectively [137].

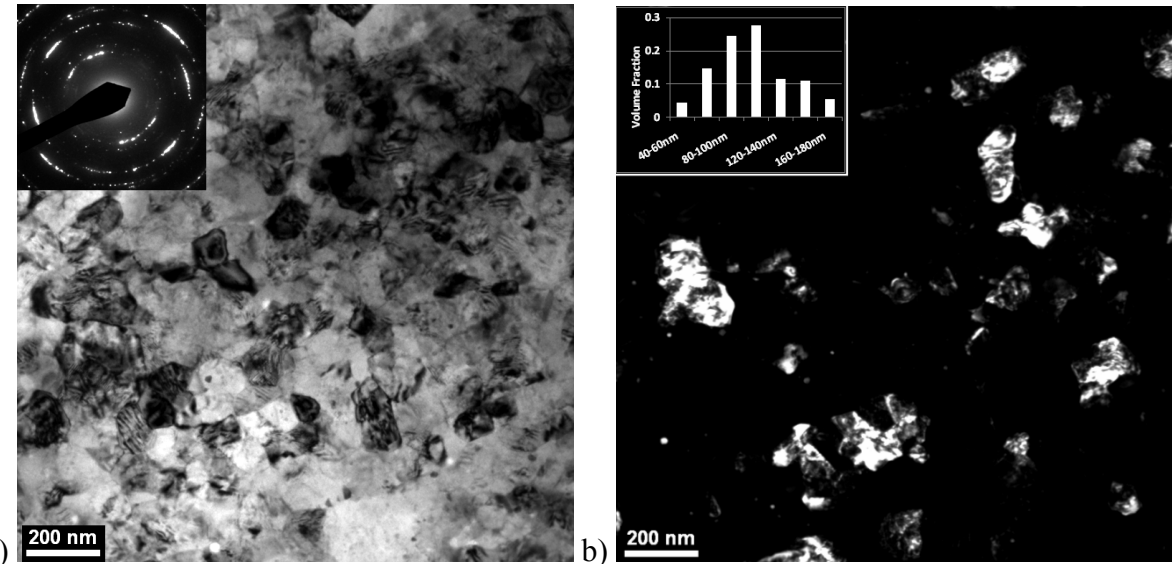


**Figure 6.7 - TEM images of B0.5Sb annealed at 600 °C using (a) bright field with inset SAD pattern, and (b) corresponding dark field with inset grain size histogram**

## 6.4 Discussion

No significant stabilization of copper or brass was found by adding antimony in quantities up to 5 at%. This is in contrast to previous MD simulations [96, 134] which suggested that Sb would be effective in thermodynamically stabilizing nanocrystalline Cu in dilute quantities (0.5%) up to 1200K (937 °C), but this is not entirely unexpected. To facilitate stabilization of the grains, solute must segregate in excess to grain boundaries. There are chemical and elastic contributions to the segregation such that a large atomic misfit and enthalpy of mixing will favor solute segregation to grain boundaries and surfaces to reduce the interfacial energy [40, 42, 57, 61]. As a first indication, consulting the phase

diagram for the Cu-Sb system [135] reveals that Sb maintains ~1% solubility at room temperature which is foreboding to achieving total stability. If the segregant is able to fit into the matrix in an equilibrium configuration, there is little expectation that grain boundaries will be stabilized by “excess” solute on the boundaries. The solubility reaches a maximum of 5.8% at 645 °C so that even for large concentrations (e.g. Cu<sub>5</sub>Sb alloy) which will favor segregation at lower temperatures will likely suffer as the temperature is elevated, indeed, where it is most important. Experimentally the results for the Cu-Sb alloys generated here are quite similar to those for UFG Cu-Sb alloys [96] exhibiting an increase in stability to 400 °C. This improvement is relatively modest in comparison to other systems using other segregants such as Zr [102, 137], Nb [51-53], W [53, 54], Mo [51], etc.

The brass-Sb alloys behaved similarly to the Cu-Sb alloys in that the alloying additions were ineffective at significantly extending the grain stability. With the brass, it actually appears the additions only reduced the stability of the material. Sb has negligible solid solubility in Zn [135, 138], and in the Cu-Zn-Sb ternary [139] the Sb solubility in Cu<sub>30</sub>Zn is ~0.6% at 550 °C and only 0.01% at 200 °C. The lower solubility in brass may account for the Sb segregation seen optically and using SEM where it was found that Cu and Sb were enriched. Despite lack of solubility, significant intermetallic formation was only seen in the B<sub>5</sub>Sb alloy, and not in the Cu<sub>5</sub>Sb alloy which is attributed to Zn-Sb interactions [140]. Though these complex interactions may be of interest for other purposes, in regard to grain size stabilization it appears to be quite detrimental.

These alloys, based on their processing, were susceptible to pore formation at elevated temperature and with increasing Sb concentration. This is expected to be caused by the increased diffusion of Ar and structural softening at high temperature which is exacerbated by a steep decline in the solidus line with increased Sb addition in Cu. Though this tendency toward pore formation can by no means be disregarded, the impact on stability is expected to be minimal at the lower annealing temperatures when the material is still able to resist expansion, and if anything, beneficial by porosity pinning [80] as long as the pore size is small enough to be effective. After low annealing temperatures the alloys were quite brittle as might be expected from Seah's work [97] and which worsened with increasing Sb content. Effort was put into consolidating the alloys for mechanical testing (hot pressing with 1.5 GPa pressure at 400 °C), however, the specimens broke apart even before testing and the endeavor was abandoned.

The thermodynamic expectations for the system can be quite misleading. When a modified Wynblatt-Ku model [64] is applied to the Cu-Sb and brass-Sb systems, the indication is that stabilization will be achieved. Antimony has a number of characteristics favorable for this result when applying this treatment. First, the enthalpy of mixing as reported in Miedema et al. [141] is -7 kJ/mol for Cu-Sb, and -3 kJ/mol for Zn-Sb. These small negative values indicate that interatomic potential is not strongly favored for like or dislike neighbors and uniform distribution is likely. Secondly, the atomic volume of Sb is quite large (~16.96 cm<sup>3</sup>/mol [141]). This will lead to a large elastic misfit contribution to segregation. Sb also has a low surface energy (~.566 J/mol [132]) which aids in boundary energy reduction when

enriched in solute. Despite favorable indications, it is expected the high level of equilibrium solubility overrides the calculated stabilization trends. Although there may be room temperature segregation, it is expected dissolution back into solution reduces or eliminates the excess boundary concentration during annealing.

A high solubility can have a two-fold effect. In Pd-Zr alloys, the solubility of Zr in Pd is ~14% [47]. Improved stability for a 20% Zr alloy was found to be thermodynamically caused due Zr segregation to grain boundaries [46]. In subsequent work, the grain growth and stabilization behavior were modeled as solute drag for 19% Zr [45] finding good correlation. Later work outside of that group using the modified Wynblatt-Ku model [48] found that the system is not expected to be thermodynamically stable. When reproducing the experimental work, it was discovered that XRD results indicated a stable grain size and were nearly identical to the early work, however, additional microscopy indicated the grain size had grown much larger. The Pd-Zr alloys were supersaturated but thermodynamically ineffective, but the solute was present in quantities large enough for significant solute drag effects. Sb in Cu is expected to be thermodynamically suitable but evidently the boundary concentration at high temperature is not high enough for a true excess concentration and apparently too dilute for significant solute drag.

Even though there is appreciable equilibrium solubility of Sb in Cu, grain boundary enrichment has been reported for a 0.5 at% alloy with a 57  $\mu\text{m}$  grain size [142] as found by Auger analysis where the segregation was reported to be nearly complete after a 700 °C

extrusion. An enriched boundary condition was also found in the UFG Cu work [96]. Antimony segregation has also been reported to drastically reduce surface and grain boundary energy in copper, even when present at only 0.25 at% [143]. As mentioned for brass, segregation was also significant, though apparently mostly to surfaces, but the lack of solubility of Sb in brass may be the determining factor in this behavior. Even though the 5% Sb alloys should have the excess solute available at room temperature, the solubility (in Cu) quickly increases to 4.6% at 400 °C and by 488 °C is 5.65% [135] which decreases and eventually eliminates the effective solute excess as the composition quickly approaches equilibrium solubility in the annealing range of interest. This is further complicated by the formation of intermetallics as seen in TEM which reduces the excess solute available for segregation but contributes to kinetic stability as proposed for MD results in [96] though the thermodynamic effect is thought to be much more important to stability.

## 6.5 Conclusions

In regard to grain size stabilization of copper and brass, antimony was found to be mostly ineffective. Though some benefit was achieved in copper for Sb concentrations of 1% and 5%, brass failed to realize additional stability for any concentration. Though thermodynamic calculation seems to favor stabilization, the considerable equilibrium solubility of Sb in Cu is thought to work in opposition. Careful definition of “excess” solute on the boundaries in light of equilibrium conditions can help account for the discrepancy.

The alloys were found to become porous at high annealing temperatures, and the level of porosity increased with Sb content. The 5% Sb in brass experienced significant surface segregation at 600 °C as evidenced by optical and electron microscopy. Though these findings are important to note, the influence they have on the grain size stability at relevant temperatures is not expected to be significant. Based on these results, antimony is not suggested as a dopant for grain size stabilization given the other options for stabilizing these systems (e.g. Zr, Nb, etc.).

## **7 *Stabilization of Copper by Tungsten***

---

---

Copper was mechanically alloyed with tungsten in a cryogenic, high-energy ball mill. The process created tungsten particles as a second phase in a nanocrystalline copper matrix. These “alloys” were then annealed to a maximum temperature of 800 °C. As milling time and tungsten content were increased, the grain size stabilization improved. The addition of tungsten stabilized the Cu in a nanocrystalline state during annealing up to 400 °C with 1% W and 600 °C with 10% W, both being milled for 8 hr. Though the stability is improved over pure copper, the benefit was likely hindered by an extremely broad particle size distribution (~10-5000 nm). For the 10% alloy, the effective second phase content (nm particle size) was found to be closer to half of the initial input.

### **7.1 Introduction**

The stabilization of nanocrystalline metals can be carried out in two principal manners: the reduction of grain boundary energy or the reduction of grain boundary mobility. To reduce the grain boundary energy (and therefore the driving force for grain growth) is considered the thermodynamic stabilization route (see Section 2.3.2). Typically this is accomplished by adding a solute which lowers grain boundary energy upon segregation (e.g.

[56, 58, 61, 74]). The second method, or kinetic stabilization, involves reducing the grain mobility by methods such as solute drag and second phase drag [12]. The kinetic route to stabilization (see Section 2.3.1) is thought to be fundamentally inferior to thermodynamic mechanisms since solute drag is unable to stop growth alone but is thought to be aided by thermodynamic contributions [71, 73] and a second phase tends to coarsen at high temperature [144] where the stabilization is most critical. Second phase drag, also known as Zener drag or Zener pinning [41], is mostly clearly demonstrated in immiscible systems where no equilibrium solubility exists. Also, that no intermetallic compounds form between the constituents simplifies the systemic considerations since the pinning will be the result of a single phase. An exemplary case of these properties is found in the Cu-W system. A brief consultation of the equilibrium phase diagram [145] reveals that an “alloy” of the two will have no solid solubility and form no compounds on heating. The kinetic ability is also bolstered by the negligible diffusivity of W in Cu, though in nanocrystalline Cu the grain boundary volume is much higher which enhances diffusion [146]. These favorable properties have been demonstrated in deposited films ~0.2-1.2  $\mu\text{m}$  thick [53, 54] where a 10% W alloy was found to outperform Mo and Nb alloys of the same concentration, and stabilized the Cu grains below 30 nm up to 900 °C. Though mechanical alloying via ball milling has been applied to the Cu-W system (e.g. [147-149]), the thermal stability of nanograined Cu in this system has only been well-described in thin film structures.

The ability to generate similar results on a larger scale was studied by alloying Cu and W powders via cryogenically high-energy ball milling. Alloying, as used here, must be loosely

interpreted because of the immiscibility of the constituents, and the final material is more properly considered a composite, but for simplicity the two terms should be considered equal for the purpose of this discourse. W was added to copper in concentrations of 1, 5, and 10 at%. Characterization by x-ray diffraction, microhardness, and electron microscopy provides evidence that the alloys displayed improved microstructural stability with increasing W concentration and milling time. A shorter milling time was found equally effective when a W nanopowder was used, but for reasons described, was not ideal for comparison. The reasons for this improvement and penalty associated are discussed.

## 7.2 Experimental

Elemental powders of copper (Alfa Aesar, 99.9%) and tungsten (Cerac, 99.99%) or tungsten nanopowder (50nm, Hongwu Nanometer, 99.9%) were added in appropriate quantities to a 440 stainless steel vial (Spex SamplePrep) with grade 25, 440 stainless steel ball bearings (Salem Specialty Ball). The ball charge consisted of 17 balls 0.3125" in diameter and 16 balls 0.250" in diameter. The ball to powder weight ratio was maintained at 10:1. All materials were loaded into the vial in an argon atmosphere ( $O_2 < 1$  ppm) and sealed before transferring to the mill. A modified Spex 8000 mixer/mill was used where the powders were milled for 4 hr or 8 hr at liquid nitrogen temperature (-196 °C). Tungsten was added with the copper to concentrations of 1, 5 and 10 at% (these alloys will be referred to as Cu1W, Cu5W and Cu10W respectively). Tungsten nanopowder was only added in a

concentration of 10% and will be denoted as Cu10nW. The alloys using the large W powder particles as a precursor will referred to as conventional W alloys. Milling times are listed with the compositions in figures and text. The milled powders were annealed under 2% H<sub>2</sub> (bal. Ar) for 1 hr at temperatures from 200 °C to 800 °C in 200 °C increments in a Lindberg tube furnace into which the samples were inserted once the furnace had stabilized at the appropriate temperature. After annealing the compacted powder, samples were polished and at least 10 Vickers hardness measurements were collected for each annealing condition using a Buelher Micromet II with a 25 g load applied for 12 sec. Cu with 5% or less tungsten yielded coarse powder (particles > 500 µm) which were supported on a glass slide, fixed in place using super glue, and polished flat. Using supported particles allowed the elimination of compaction effects on hardness. The method was verified by comparison with the compacted samples, and the results were equivalent. Error bars for hardness were calculated by standard deviation. X-ray diffraction (XRD) analysis was conducted using a Rigaku DMax/A X-ray diffractometer using Cu K $\alpha$  radiation. Proper alignment was verified before each use using a single crystal silicon standard. The spectra were processed by smoothing (function filter), removing the background, and K $\alpha$ 2 stripping (optimized Rachinger's method) using Xpowder software ([www.xpowder.com](http://www.xpowder.com)). The grain size was estimated using the Scherrer equation [13] applied to the first peak of the pattern. Scanning electron microscopy (SEM) analysis was performed with a JEOL JEM 6010LA using a 20 keV beam energy. The SEM is equipped with an energy dispersive X-ray spectrometer (EDS) which was used for x-ray mapping and to verify atomic concentrations. Transmission electron microscopy (TEM) was carried out using a JEOL JEM 2000FX using a beam energy of 200

keV. TEM samples were generated by uniaxially pressing the powder at 2.6 GPa in 3 mm tungsten carbide die and subsequently annealing the compact. The compacts were mechanically thinned, electropolished using 30 vol% nitric acid in methanol at -20 °C in a Tenupol-2 electropolisher, and final thinning was performed with a Fischione Model 1010 ion mill. TEM images have basic brightness and contrast adjustments applied to aid in viewing and printing clarity. To determine grain size at least 170 grains were measured, and particle sizes were determined using at least 200 particles. Grains are assumed spherical for grain size results.

### 7.3 Results

Though not absolute, XRD grain size estimation provides a quick and informative analysis technique. In the present configuration, any estimated grain size over 40 nm is considered to be well above that number, and estimates below 30 nm are believed to be reasonably accurate. Given these caveats, the results from XRD estimation are shown in Figure 7.1. It can be seen that as the percentage of W increases, the annealing temperature to which it remains nanoscale also increases. Also, the longer milling times (gray symbols) tend to extend stability, and the effect seems quite profound for the Cu1W alloy. The three conventional W alloys when milled for 8 hr and the Cu10nW when milled for 4 hr showed nearly identical behavior up to 400 °C which is much improved over pure Cu. Differences in estimated grain size above 40 nm are considered instructive, but not necessarily proportional.

Also of interest is that the W nanopowder contained significant oxidation as found by XRD and SEM analysis which will affect the behavior.

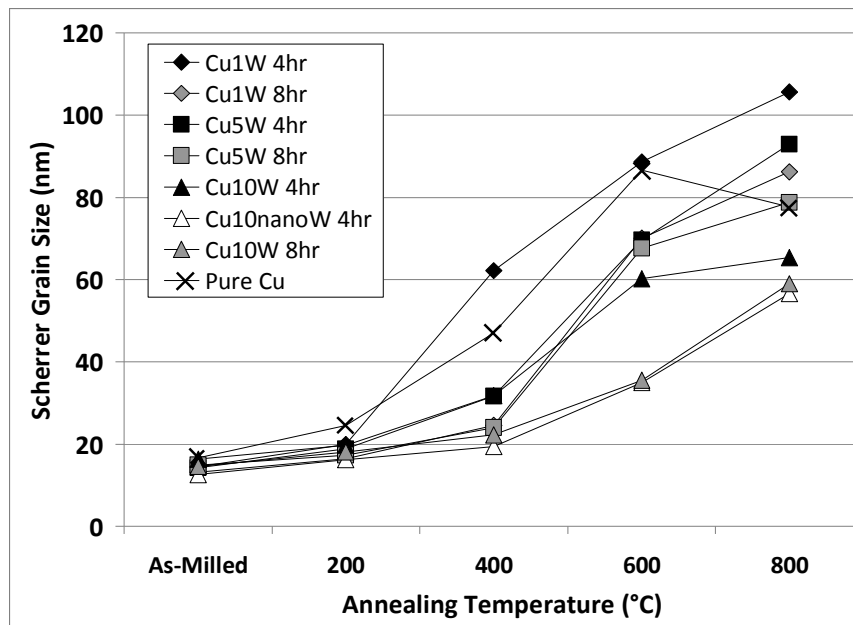


**Figure 7.1 - XRD grain size estimate for various alloys and annealing conditions**

Cu10W milled for 8hr and Cu10nW milled for 4 hr both showed expected stability to 600 °C by XRD estimation, and the evolution of the X-ray spectra with annealing is shown in Figure 7.2. The Cu10W 8 hr sample has noticeably more intense W peaks than the Cu10nW sample in relation to the Cu peaks. EDS analysis reports 10.37 at% and 9.92 at% W for the two alloys respectively, and though it will contribute, it also is expected that the finer particle size also reduces intensity by broadening the signal to a somewhat greater extent. Both alloys show a nearly imperceptible change in peak sharpness throughout the annealing range, and when the Scherrer equation is applied to the W peaks, the estimate particle size between ~17-

30 nm for all alloys and at all temperatures. Though some alloys exhibited slight coarsening, the expected error is great enough not to claim any fundamental knowledge of the behavior. This is further elaborated on in the electron microscopy results.

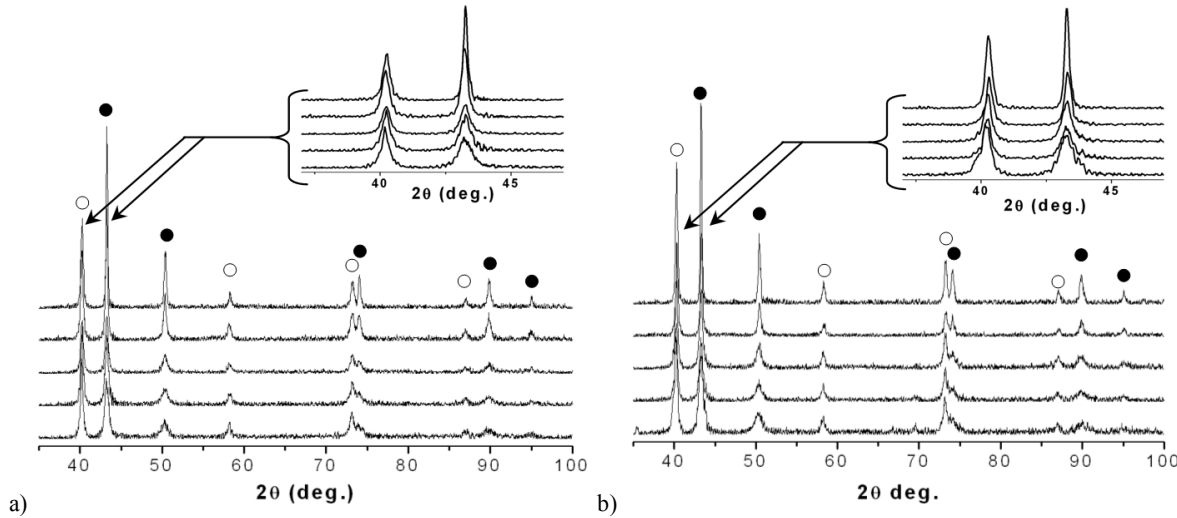


**Figure 7.2 – XRD spectra after annealing at labeled annealing temperatures for (a) Cu10W milled for 8 hr and (b) Cu10nW milled for 4 hr.** ○ - indicates (with increasing angle) W peaks for 110, 200, 211, and 220 reflections. • - indicates (with increasing angle) Cu peaks for 111, 200, 220, 311 and 222 reflections. The insets at the top-right of the images highlight the W 110 and Cu 111 peaks.

The hardness values were obtained for each alloy through the annealing range and the results are shown in Figure 7.3. All of the conventional W alloys are nearly identical in as-milled hardness, but the nanoscale W alloy is somewhat higher. The alloys show similar trends as seen in Figure 7.1, but here it is found that the Cu10W 8 hr alloy and the Cu10nW alloy retain an appreciable hardness that is not closely mirrored by the Cu10W 4 hr alloy and hence cannot be linked to W content alone. The first two alloys do show a smaller grain size

(though well above the accuracy limit) but the finer dispersion of W particles is likely responsible for the behavior.

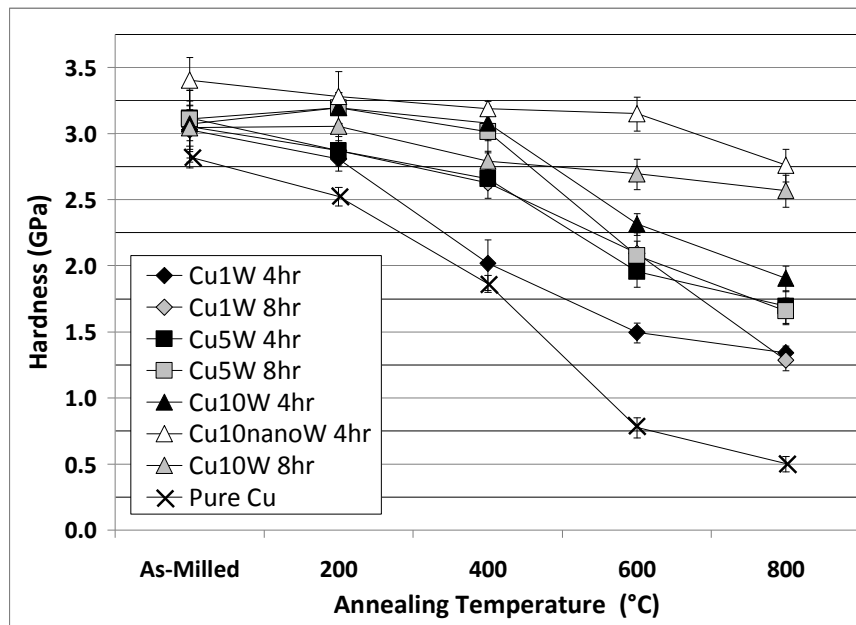


**Figure 7.3 - Hardness results for annealed Cu-W alloys**

When the samples were polished and examined using SEM (see Figure 7.4) the lack of particle size uniformity and the error of the particle size estimate using the Scherrer equation became quickly evident. The Cu1W alloys are shown in Figure 7.4 and though there is a definite reduction in overall particle size by milling for longer time, there are still many large particles. EDS mapping of the alloys (Figure 7.4c, d) reports tungsten throughout the bulk, possibly as unresolved particles. The qualitative differences between the two are small and if there is a finer distribution after milling for 8 hr then a higher resolution technique would be

needed. However, the simplicity and simple sample preparation make SEM attractive for qualitative treatment.

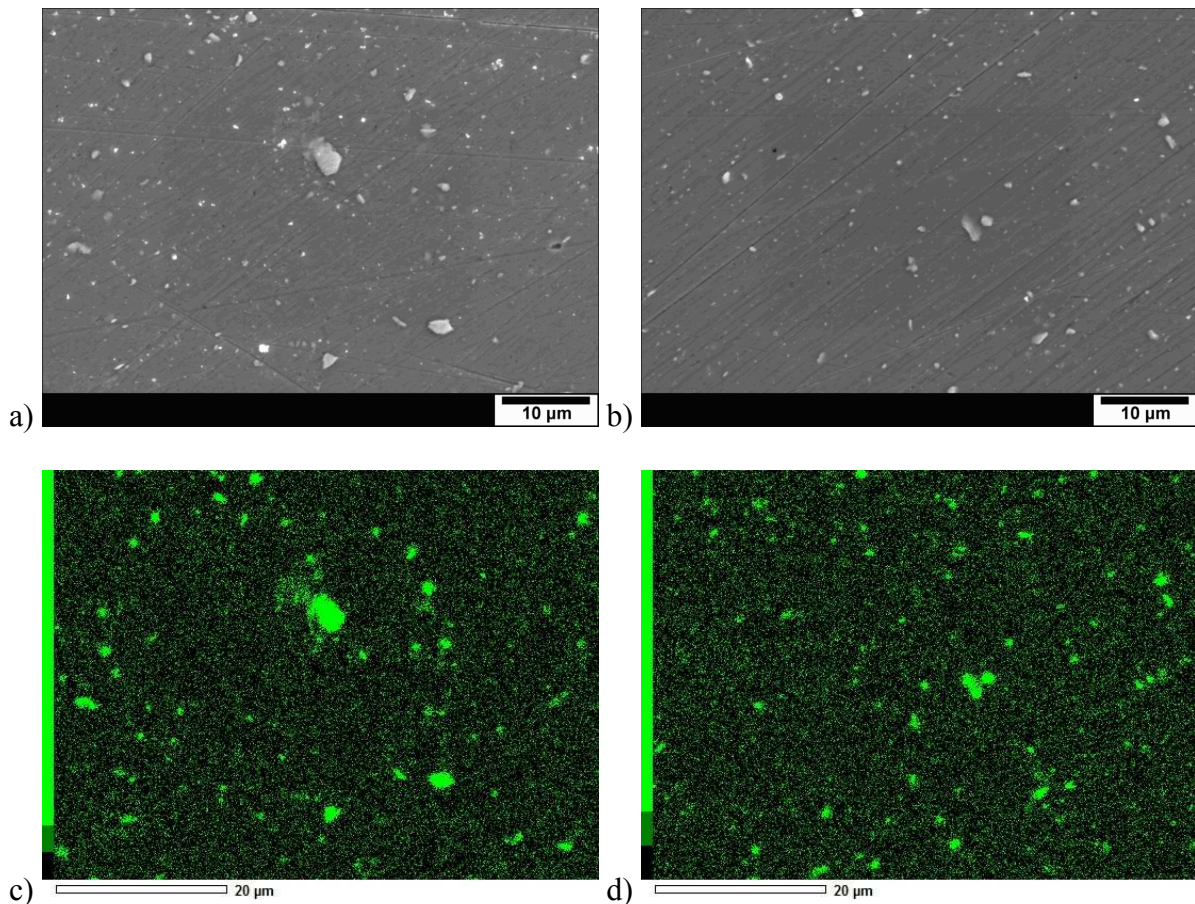
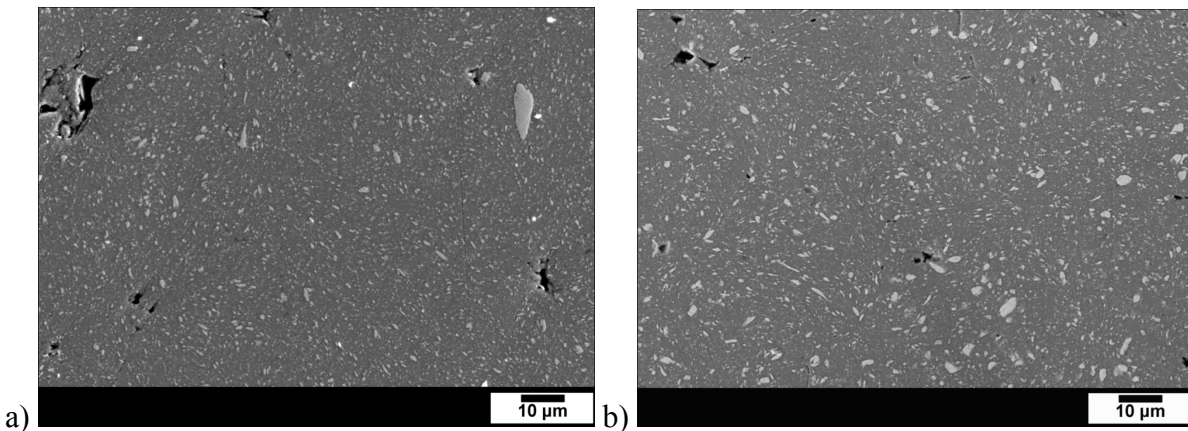


Figure 7.4 - SEM images of as-milled Cu<sub>1</sub>W milled for (a) 4 hr and (b) 8 hr. EDS maps of (c) W corresponding to the sample milled for 4 hr shown in (a) and (d) W corresponding to the sample milled for 8 hr shown in (b).

SEM of the 10% W alloys (Figure 7.5) showed a similar particle size distribution to the 1% alloys but with a greater area fraction of W. This is especially concerning because the W nanopowder was expected to be valuable for the initial size benefit. After examination of the

as-received powder it was clear that many particles were not nanoscale but rather up to a few microns in diameter. The SEM images reveal that the distribution of the particle sizes actually tend to be slightly larger than for the 8 hr milled Cu10W alloy. It is expected the large particles were not reduced in size as well due to the shorter milling time, but the higher content of nanoscale particles initially present was close to the final concentration in the Cu10W milled for 8 hr. This indicates that only the smallest particles are effective with regard to stabilization as expected (see discussion).



**Figure 7.5 - SEM images of as-milled Cu10W 8hr and Cu10nW milled for 4 hr**

The area fraction of the particles and particle size distribution was calculated by generating a binary image and using Image J particle size analysis (see Table 7.1). This was compared to the overall gray level (256 grayscale) in the binary image and showed good correlation. The results of the analysis cannot be taken too quantitatively since there are W particles below the resolution limit in the SEM images which are not accounted for, and for stabilization purposes, are the most important. However, based on the relative W concentrations and the

milling times, the area fraction is regarded as the most significant indicator. As evidenced with the conventional W alloys, the area fractions drop significantly when milled longer. The Cu10W and Cu10nW alloys have nearly identical W particle area fractions and their annealing behaviors are quite similar. Of course, analysis in this way is hardly quantitative in any absolute sense, but it does provide a simple method for estimating the performance in a relative sense. Ideally, there would be no resolved particles, and obviously the milling conditions were insufficient for achieving a nanoscale dispersion of W particles equivalent to the initial concentration. Also to note, the cause for a particle area fraction in excess of the molar quantity added is due to the subsurface sampling of high energy electrons. As verified using CASINO Monte Carlo software (<http://www.gel.usherbrooke.ca/casino/index.html>), even if a 50 nm W particle is 100 nm below the surface of the Cu, a great majority of the backscattered electrons (contrast mechanism) will come from the W. Being that most particles resolved are much larger than that, particles appearing in the images are present at various depths of the material.

**Table 7.1 - W particle size distribution and area fraction from SEM analysis for W particles observable with SEM resolution (the smallest particles not included).**

	Cu1W		Cu5W		Cu10W		Cu10nW
	4hr	8hr	4hr	8hr	4hr	8hr	4hr
Milling Time							
Volume Average	401.04	418.02	762.87	551.27	592.84	505.18	531.76
Number Average	238.08	262.48	345.54	335.96	307.27	284.75	298.17
Area Fraction	0.0248	0.0154	0.1058	0.0744	0.2026	0.1526	0.1430

As for the unresolved particles in SEM, TEM was used to better determine the actual Cu grain and W particle sizes. The Cu10W 8 hr alloy was chosen as a focus case since it exhibited the best stability and most realistic milling scenario for large scale production as well as to avoid complications possibly caused by the oxidation present with the W nanopowder. Figure 7.6 shows the Cu10W 8hr alloy after annealing at 600 °C. This was the limit of stability as estimated by XRD, and the fairly continuous rings in the selected area diffraction (SAD) pattern (Figure 7.6a) coupled with dark field (Figure 7.6b) both confirm the grain size retention (47.4 nm and 32.6 nm volume and number averages respectively). Using the W 110 ring in the SAD pattern, the particle distribution could be highlighted (Figure 7.6c). It is evident that there is a considerable distribution of nanoscale W particles. The volume and number averages for the W particles are 14.5 nm and 9.1 nm respectively. The distribution of grain and particle sizes is shown in Figure 7.6d. Particles > 40 nm were not included in TEM size and distribution since they greatly skewed the volume average computation and contributed very little to the number fraction since they were rare at high magnification. These large particles are more accurately dealt with in the SEM analysis above.

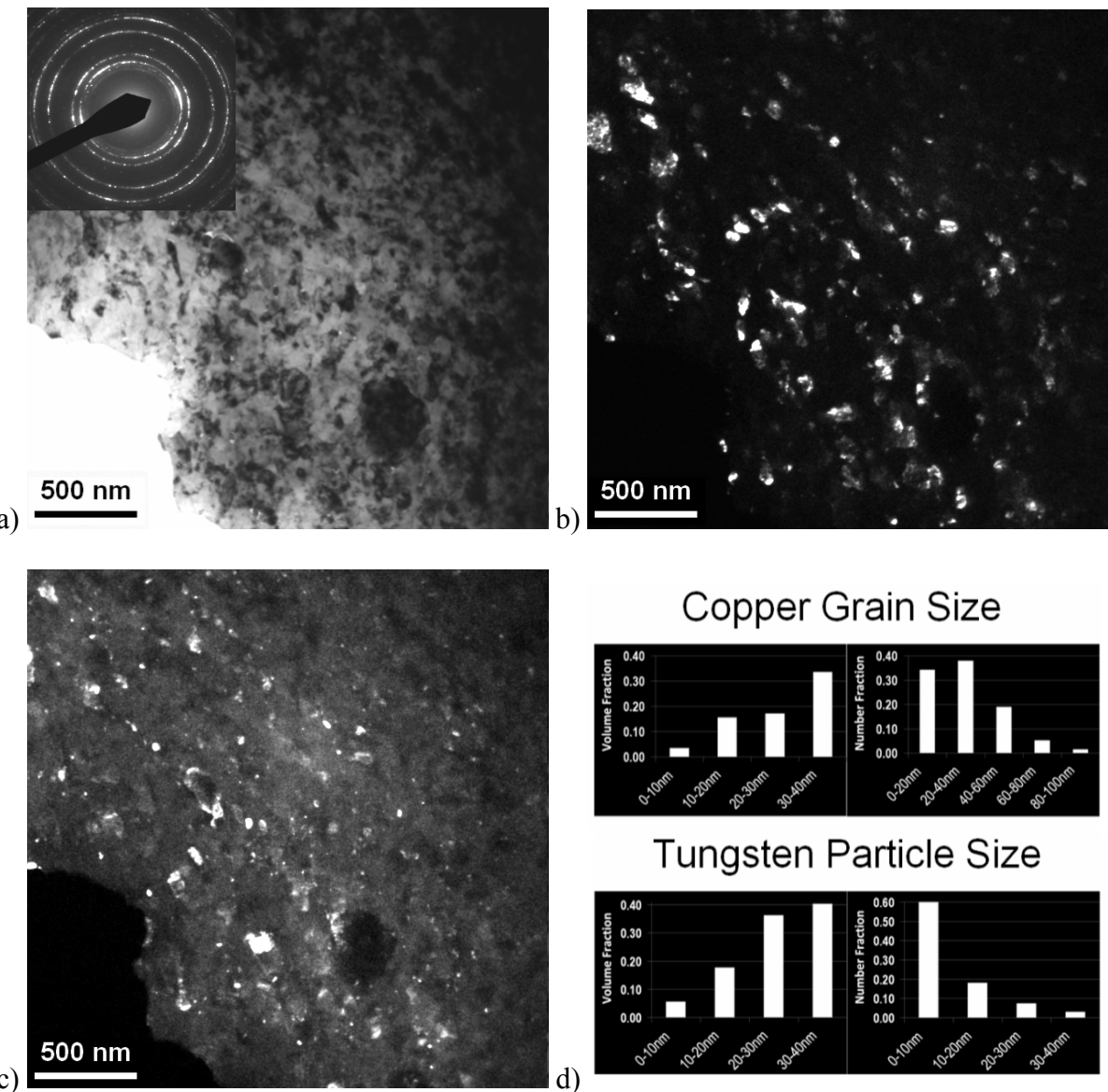


Figure 7.6 - Cu10W alloy milled for 8hr and annealed at 600 °C for 1 hr. (a) bright field image with SAD pattern inset top-left (b) dark field image using 111 and 200 Cu rings (c) dark field image using 110 W ring and (d) Cu grain size and W particle size distribution

According to XRD, after annealing at 800 °C the grains should grow significantly, and by previous experience the grains are expected to be well above the Scherrer estimate. This is indeed the case as the SAD pattern (Figure 7.7a) is now quite discontinuous and dark field of Cu grains (Figure 7.7b) reveals a rather large size with a volume average of 130.3 nm and a number average 110.3 nm. The W particles, highlighted in Figure 7.7c as they were above, have volume and number averages of 13.4 nm and 7.1 nm. Although the grains have grown significantly, the average particle size has actually decreased slightly. This result shouldn't be weighted too heavily due to potential error in software recognition of particles and the possibility of inhomogeneous distribution. It is more likely evidence that the particles have not grown significantly, and this is corroborated by the number fraction distribution. For the sample annealed at 600 °C, 60% of the particles are 10 nm or less, while after an 800 °C anneal only 36% are reported in that same range.

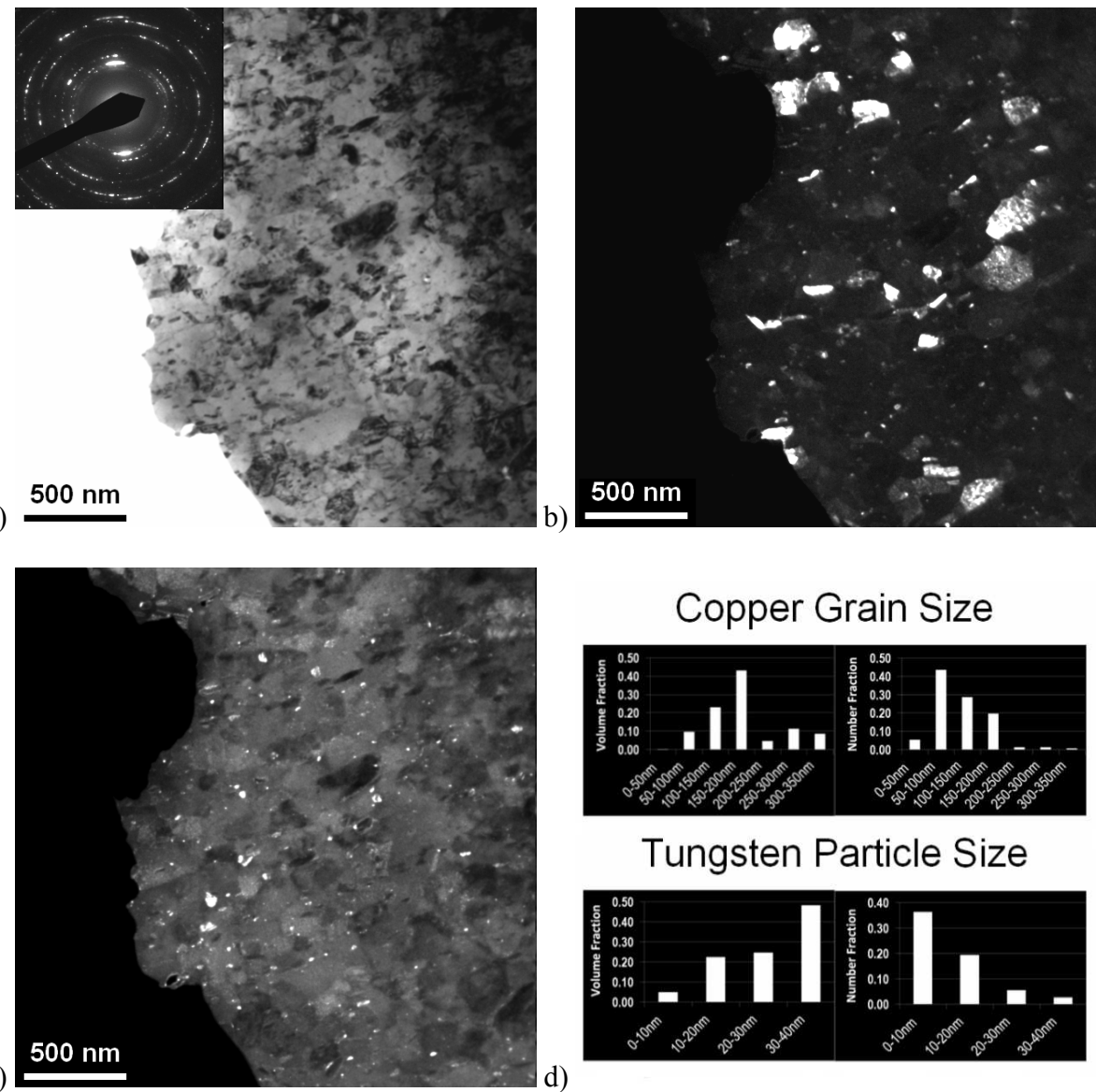
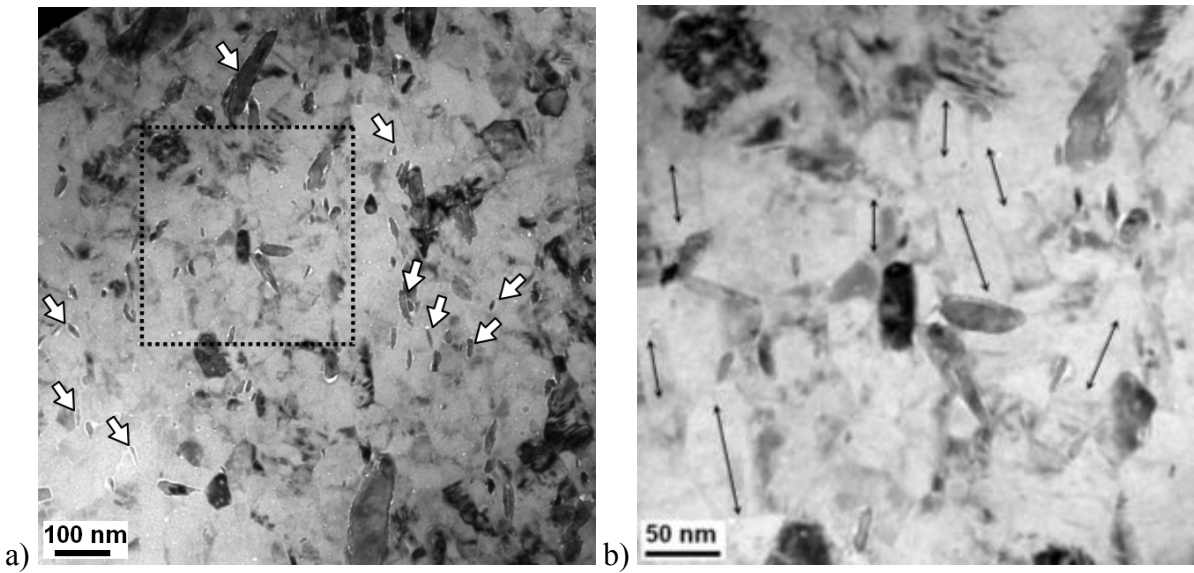


Figure 7.7 - Cu10W alloy milled for 8hr and annealed at 800 °C for 1 hr. (a) bright field image with SAD pattern inset top-left (b) dark field image using 111 and 200 Cu rings ring (c) dark field image using 110 W and (d) Cu grain size and W particle size distribution

Examination of the SAD pattern in Figure 7.7a indicates strong texturing. Though some degree of texturing was observed in many of the diffraction patterns at both 600 °C and 800 °C most were more subtle. Closer microstructural examination provides clues into why this may occur. As shown in Figure 7.8, the tungsten particles (some labeled with arrows) are elongated and have a preferred orientation. When this area is examined more closely (Figure 7.8b), there is evidence that the grains are generally following this preferred orientation with longitudinal axes in the same general direction as the W particles which may be attributed to the variation in pinning efficiency for the different particle orientations (more in the discussion). This orientation preference can also be seen in the SEM images, especially the 10% W alloys (Figure 7.5) where the W particles follows local “flow paths” so that, although randomized over a large scale, they are highly oriented on a smaller scale.



**Figure 7.8 – TEM images of Cu10W milled for 8 hr and annealed at 600 °C for 1 hr. (a)** Arrows indicate some of the tungsten particles **(b)** magnified view of boxed area in (a) with longitudinal axes of oblong grains labeled with arrows.

## 7.4 Discussion

In a general discussion of kinetic stabilization by Zener pinning, the pinning pressure,  $P_z$ , on a grain boundary with energy,  $\gamma$ , by a volume fraction,  $F$ , of spherical particles with radius,  $r$ , is given by [10, 12, 41] (see also Section 2.3.1):

$$P_z = \frac{3F\gamma}{2r} \quad (7.1)$$

This indicates that as the volume fraction of the pinning constituents increases and their size decreases, their efficacy in stabilization will improve. The results obtained here align to this concept well. For example, the 10% W alloy milled for 8 hr had better stability than that for 4 hr (smaller particle size expected) and performed better than 1% or 5% (higher volume fraction) when the same milling time was used. This result is expected, but it is complicated by the incomplete comminution of the W phase. Although the trends in stability are anticipated, deriving the actual material parameters is difficult since the particle size is non-uniform and the particles tended to be elliptically shaped. The deviation from sphericity will be twofold. For a moving boundary approaching the particle normal to its longitudinal axis, the drag force will be higher than for a spherical particle of equivalent volume [10]. If approaching parallel to that axis, the force will be lower, and the intensity of the effect is sensitive to the aspect ratio of the particle. Many of the smallest W particles had an aspect ratio of  $\sim 3:1$  which gives an effectiveness ratio for the elliptical particles to the spherical equivalents of  $\sim 1.5$  and 0.3 for the respective geometries. This in combination with the considerable local alignment of the particles gives adequate cause for the elongated grain growth after annealing since migrating grain boundaries could only be effectively pinned along one axis. However, it is conceivable texturing arises from high pressure compaction, but from the SEM results the tungsten lattice orientation is particle-defined and not in alignment with the pressing direction. Also, that other samples without this second phase character have not shown such strong texturing gives reason to believe that the W contributes.

A rough estimate of the area fraction for tungsten particles under 50 nm is ~4-6% using TEM such as that in Figure 7.8. This size range will be the most effect at pinning, but is only about half of the W added. The volume fraction penalty incurred by using this method of alloy preparation is likely unavoidable due to the tendency of nanocomposite materials to reach a lower limit for dispersoid size [150], though the size is expected to decease as a whole and increase in uniformity upon further milling. The use of cryogenic milling here optimizes second phase size reduction since W particle size in Cu increases as the temperature is increased [151] due to a balance of fracture and cold welding where, at saturation, the W is suggested to simply “swim” in the Cu matrix similar to oxide or carbide particles at saturation [152]. The thin film work on this system [53, 54] was found to be highly effective, but the W started in solution and remained below 10 nm even after annealing to 900 °C which is much more favorable toward stabilization than the conditions here. By starting with “nano” W powder in this work, the longer milling time was not necessary for similar properties, but the particle size distribution being well out of the nano range (up to several microns) significantly reduced the possible advantage. Also, the significant oxygen present in the powder made it unsuitable for close comparison with the conventional W and hence the TEM examination was focused on the “pure” system, though there is certainly some contamination present from routine sample preparation by these methods.

Despite the low volume fraction of nanoscale W, the stability is certainly an improvement over pure copper, though the alloying percentage (10%) is rather high to achieve it. Lower W

concentration would be preferable for increased conductivity [153] but higher W concentrations are useful in high stress and wear conditions such as electrical discharge machining (EDM) operations [154]. Based on maintaining a higher Cu content, W has limited effectiveness, but if a high W content is beneficial for the application, maintaining a nanocrystalline Cu matrix phase is reasonably expected.

## 7.5 Conclusions

The kinetic route to stabilization by way of Zener pinning relies on a large volume fraction of small, second phase particles homogeneously distributed in the matrix. This is a difficult proposition when starting with large particles of a hard metal (W) distributed in a soft metal (Cu). The nanocrystalline Cu grain size could be stabilized up to 400 °C by 1% W after milling for 8 hr, and to 600 °C by adding 10% W and milling for 8 hr. The W particles ranged widely in size with some being < 10 nm while others were > 5 µm. The percentage of nanoscale W was found to be approximately half of the total W concentration when milling the 10% W alloy for 8 hr. Though the addition of W improved the thermal stability of the Cu grains, the large volume fraction required by this method makes it most useful in applications where a high W content is also beneficial.

## **8 Conclusions**

---

---

There is good cause for studying nanocrystalline materials as their unique properties can be highly advantageous for a new generation of materials. The barriers to commercialization are rooted in processing, and the solutions will involve a more robust microstructure since processing variables (e.g. temperature, pressure, etc.) are somewhat limited. That is, techniques such as powder metallurgy require significant heat and pressure to fully consolidate most materials. If anything, nanocrystalline materials will likely require advances in manufacturing techniques as some of these materials are extremely strong and have limited ductility. Understanding fundamental microstructural processes in nanocrystalline systems is important to predicting their response to manufacturing procedures.

One of the unique features of nanocrystalline metals is the tendency for grain growth at temperatures well below the melting point. This propensity toward grain growth makes their use unreliable at elevated temperature. The basis of this work was to determine suitable solutes for improving the grain size stability. An ideal solute will be required in dilute quantities and bear no detriment to the mechanical, electrical, or other properties of the solvent into which it is placed. Depending on the intended use, this makes a one-size-fits-all

solute elusive, but generally it will have a large elastic misfit in the solvent lattice and low solubility even at high temperature.

In the first system, Zr was alloyed with Cu and the results were quite promising. The material was stabilized at the nanoscale to 900 °C which is approximately 86% of the melting point of pure copper. Zirconium has a large misfit in Cu, a negative heat of mixing, and based on the thermodynamic approximations detailed in Section 2.3.2.1 and applied in Section 4.4 is predicted to produce a stabilized grain structure. The negative enthalpy of mixing will lead to intermetallic formation and Zr has a strong affinity for oxygen which makes it sensitive to oxide formation. Both intermetallics and oxides were seen in the samples annealed at high temperature. The formation of these will reduce available Zr for grain boundary energy reduction but aid in kinetically pinning the boundaries. Because of the limited formation of these phases, it is unlikely their influence was sufficient to stabilize the microstructure, and the thermodynamic influence is though to be dominant. For only 1 at% Zr the grain size and hardness are nearly unaltered throughout the annealing range up to 900 °C. This system is an excellent example of the profound influence an appropriate solute can have.

The brass-Zr system was also well-stabilized, though brass was remarkably stable in “pure” form. The concept of purity is not strictly applicable as the large zinc content (30 at%) can actually be thought of a solute, albeit one that is expected to be a poor stabilizer. Solute drag may improve the stability, but there was also some limited ZnO formation seen in TEM which may have exerted a kinetic influence. The Zr formed more extensive intermetallic and

oxide phases which are attributed to the increased reactivity between Zn and Zr and for both Zn and Zr with oxygen. Nonetheless, the Zr had a positive influence on retaining the hardness at 800 °C. Though this system did not benefit to the degree that Cu did, it was also well-stabilized to a similar homologous temperature.

When using Sb as a solute there was a drastic reduction in effectiveness when compared to the Zr addition. Neither Cu nor brass saw any appreciable change in stability when 1% Sb was added, and brass performed slightly worse at high temperature. There is a large solubility of Sb in Cu which is thought to cause dissolution of the Sb back into the bulk even if it segregates at lower temperatures. These systems provided valuable insight into the importance of defining what the interfacial solute excess is when doing thermodynamic modeling. Sb possesses many favorable characteristics for stabilization purposes, but cannot deliver any more than modest improvement by using relatively large concentration (5 at%) which causes embrittlement of the material. That being said, Sb is regarded as a poor stabilization agent.

The final system, Cu-W, was the only one where kinetic means are the dominant mechanism for stability. The mutual insolubility of Cu and W results in W forming discrete particles, which, when sufficiently small, can be effective at pinning grain boundaries. The key to this route working is the particles being “sufficiently small,” and this size is a function of grain size (see Equation 2.7). Even after extensive milling (twice as long as the other alloys) there was a particle size range that spanned three orders of magnitude. The nanoscale particles

were present at only approximately half of the initial W addition which greatly reduced the effectiveness. W is a good candidate for kinetic pinning as it shows essentially no appreciable coarsening up to 800 °C, but the practicality of generating nanoscale dispersions is wanting. Despite the difficulties of reducing the W to a productive size, the stability was maintained up to 600 °C for the 10% W material after being milled for 8 hr. It is obvious, when compared to the Cu-Zr alloy that the return on investment in regard to solute addition and milling requirement is relatively low. Given its moderate stabilization effects, W may be useful in applications where a more wear-resistant material is desired.

The diversity of systems studied allows for a well-rounded look at the effectiveness of solutes toward the stabilization of nanocrystalline copper and brass. Indeed, brass itself is rarely investigated, but it proved to be an interesting alloy, retaining its strength even after significant heat treatment. The application of the modified Wynblatt-Ku model discussed in Section 2.3.2.1 proved useful in predicting and interpreting the experimental results. The extension of this model, in a simplified manner, to ternary systems was at least qualitatively consistent with experimental data.

The tailoring of nanocrystalline metals is bound to become more intricate with time. Binary alloys are generally studied for simplified analysis. Many important structural materials (e.g. steels) are fairly complicated with many minor alloying additions that serve various purposes. This may be the future for nanocrystalline materials as well. For example, in Cu, both Zr and W could be added, the Zr to stabilize boundaries in a dilute fashion and the W to

increase wear resistance and kinetically pin boundaries. The combination of solutes in a synergistic way may help extend the usefulness of nanocrystalline metals. Despite the obstacles to commercialization of nanocrystalline metals, the benefits are looming larger. Once there is a sufficient knowledge of these nanoscale systems, robust solutions can be formulated to withstand processing techniques required for industrial scaling. There are many advancements yet needed to see these materials brought into a commercial setting, but the intervening research is bound to improve the understanding and quality of the end product. That is to say, the best is yet to come.

## **9 References**

---

---

- [1]Hall EO. The Deformation and Ageing of Mild Steel: III Discussion of Results. Proceedings of the Physical Society B. 1951; 64:747-53.
- [2]Petch NJ. The cleavage of polycrystals. The Journal of the Iron and Steel Institute. 1953;174:25-8.
- [3]Youssef KM, Scattergood RO, Murty KL, Horton JA, Koch CC. Ultrahigh strength and high ductility of bulk nanocrystalline copper. *Appl Phys Lett.* 2005;87(9):091904--3
- [4]Youssef KM, Scattergood RO, Murty KL, Koch CC. Ultratough nanocrystalline copper with a narrow grain size distribution. *Appl Phys Lett.* 2004;85(6):929-31.
- [5]Schiøtz J, Jacobsen KW. A maximum in the strength of nanocrystalline copper. *Science.* 2003;301(5638):1357-9
- [6]Schiøtz J, Tolla FDD, Jacobsen KW. Softening of nanocrystalline metals at very small grain sizes. *Nature.* 1998;391(6667):561-3.
- [7]Conrad H, Narayan J. On the grain size softening in nanocrystalline materials. *Scripta Mater.* 2000;42(11):1025-30.
- [8]Suryanarayana C, Ivanob E, Boldyrev VV. The science and technology of mechanical alloying. *Mater Sci Eng, A.* 2001;304-306:151-8.

- [9]Ames M, Markmann J, Karos R, Michels A, Tschope A, Birringer R. Unraveling the nature of room temperature grain growth in nanocrystalline materials. *Acta Mater.* 2008;56(16):4255-66
- [10]Nes E, Ryum N, Hunderi. On the Zener drag. *Acta Metall.* 1985;33(1):11-22.
- [11]Porter DA, Easterling KE. Phase transformations in metals and alloys. 2nd ed. London: Chapman Hall 1992, p. 140-2.
- [12]Koch CC, Scattergood RO, Darling KA, Semones JE. Stabilization of nanocrystalline grain sizes by solute additions *J Mater Sci.* 2008;43(23-24):7264-72.
- [13]Cullity BD, Stock SR. Elements of X-Ray Diffraction. 3rd ed. Upper Saddle River: Prentice Hall 2001, p. 170.
- [14]Cao G, Wang Y. Nanostructures & nanomaterials: synthesis, properties & applications. 2 ed. Singapore: World Scientific; 2011.
- [15]Kelly KL, Coronado E, Zhao LL, Schatz GC. The Optical Properties of Metal Nanoparticles: The Influence of Size, Shape, and Dielectric Environment. *Journal of Physical Chemistry B.* 2003;107(3):668-77.
- [16]Callister WD. Materials science and engineering: an introduction. 7th ed. New York: John Wiley & Sons 2007, p. 39.
- [17]Meyers M, Chawla K. Mechanical behavior of materials. 2 ed. New York: Cambridge University Press 2009, p. 346.
- [18]Callister WD. Materials science and engineering: an introduction. 7th ed. New York: John Wiley & Sons 2007, p. 189.

- [19]Meyers M, Chawla K. Mechanical behavior of materials. 2 ed. New York: Cambridge University Press 2009, p. 347.
- [20]Hahn H, Mondal P, Padmanabhan KA. Plastic deformation of nanocrystalline materials. *Nanostructured Materials*. 1997;9(1-8):603-6.
- [21]Schiotz J, Vegge T, DiTolla FD, Jacobsen KW. Atomic-scale simulations of the mechanical deformation of nanocrystalline metals. *Phys Rev B*. 1999;60(17):11971-83.
- [22]Scattergood RO, Koch CC. A modified model for Hall-Petch behavior in nanocrystalline materials. *Scripta metallurgica et materialia*. 1992;27(9):1195-200.
- [23]Lu K, Sui ML. An explanation to the abnormal Hall-Petch relation in nanocrystalline metals. *Scripta metallurgica et materialia*. 1993;28(12):1465–70.
- [24]Meyers MA, Mishra A, Benson DJ. Mechanical properties of nanocrystalline materials. *Prog Mater Sci*. 2006;51(4):427-556.
- [25]Khan AQ, Brabers M, Delaey L. The Hall-Petch relationship in copper-based martensites. *Materials Science and Engineering*. 1974;15(2-3):263-74.
- [26]Shen TD, Schwarz RB, Feng S, Swadener JG, Huang JY, Tang M, et al. Effect of solute segregation on the strength of nanocrystalline alloys: Inverse Hall–Petch relation. *Acta Mater*. 2007;55(15):5007-13.
- [27]Koch CC. Intermetallic matrix composites prepared by mechanical alloying—a review. *Mater Sci Eng, A*. 1998;244(1):39-48.
- [28]Nieman GW, Weertman JR, Siegel RW. Mechanical behavior of nanocrystalline Cu and Pd. *J Mater Res*. 1991;6:1012-27

- [29]Folmanis GÉ, Uglov VA. Nanocrystalline copper powders produced by electrolysis. Soviet Powder Metallurgy and Metal Ceramics. 1991;30(2):95-6.
- [30]Koch CC, Cho YS. Nanocrystals by high energy ball milling. Nanostruct Mater. 1992;1(3):207-12.
- [31]Kim HS, Hong SI, Lee YS, Dubravina AA, Alexandrov IV. Deformation behavior of copper during a high pressure torsion process. J Mater Process Tech. 2003;142(2):334-7.
- [32]Liao XZ, Zhao YH, Srinivasan SG, Zhu YT, Valiev RZ, Gunderov DV. Deformation twinning in nanocrystalline copper at room temperature and low strain rate. Appl Phys Lett. 2004;84(4):592-4.
- [33]Gilman PS, Benjamin JS. Mechanical Alloying. Annu Rev Mater Sci. 1983;13:279-300.
- [34]Koch C, Pathak D, Yamada K. Mechanical alloying for structural applications. In: DeBarbadillo JJ, Froes FH, Froes JJ, Schwarz RB, eds. Conference on Structural Applications of Mechanical Alloying. Materials Park, OH: ASM International 1993.
- [35]Yamada K, Koch C. The influence of mill energy and temperature on the structure of the TiNi intermetallic after mechanical attrition. J Mater Res. 1993;8(6):1317-26.
- [36]Kim MS, Koch CC. Structural development during mechanical alloying of crystalline niobium and tin powders J Appl Phys. 1987;62(8):3450-3.
- [37]Goodwin PS, Hinder TMT, Wisbey A, Ward-Close CM. Recent progress in the clean mechanical alloying of advanced materials. Mater Sci Forum. 1998;269-272:53-62.
- [38]Koch CC. Materials synthesis by mechanical alloying. Annu Rev Mater Sci. 1989;19:121-43

- [39]VanLeeuwen BK, Darling KA, Koch CC, Scattergood RO. Novel technique for the synthesis of ultra-fine porosity metal foam via the inclusion of condensed argon through cryogenic mechanical alloying. *Mater Sci Eng, A*. 2011;528(4-5):2192–5.
- [40]Trelewicz JR, Schuh CA. Grain boundary segregation and thermodynamically stable binary nanocrystalline alloys. *Phys Rev B*. 2009;79(9):1-13.
- [41]Humphreys FJ, Hatherly M. Recrystallization and related annealing phenomena. 2nd ed. Amsterdam: Elsevier; 2004.
- [42]Liu F, Kirchheim R. Grain boundary saturation and grain growth. *Scripta Mater*. 2004;51(6):521–5.
- [43]Cahn JW. The impurity-drag effect in grain boundary motion. *Acta Metall*. 1962;10(9):789-98.
- [44]Mendelev MI, Srolovitz DJ. A regular solution model for impurity drag on a migrating grain boundary. *Acta Mater*. 2001;49(4):589-97.
- [45]Michels A, Krill CE, Ehrhardt H, Birringer R, Wu DT. Modelling the influence of grain-size-dependent solute drag on the kinetics of grain growth in nanocrystalline materials. *Acta Mater*. 1999;47(7):2143-52.
- [46]Krill CE, Klein R, Janes S, Birringer R. Thermodynamic stabilization of grain boundaries in nanocrystalline alloys. *Mater Sci Forum*. 1995;181: 443-8.
- [47]Waterstrat RM, Shapiro A, Jeremie A. The palladium–zirconium phase diagram. *J Alloys Compd*. 1999;290(46):63-70.
- [48]VanLeeuwen BK, Darling KA, Koch CC, Scattergood RO, Butler BG. Thermal stability of nanocrystalline Pd<sub>81</sub>Zr<sub>19</sub>. *Acta Mater*. 2010;58(12):4292-7.

[49]Driver JH. Stability of nanostructured metals and alloys. *Scripta Mater.* 2004;51(8):819-23.

[50]Bate P. The effect of deformation on grain growth in zener pinned systems. *Acta Mater.* 2001;49(8):1453-61.

[51]Botcharova E, Freudenberger J, Schultz L. Mechanical alloying of copper with niobium and molybdenum. *J Mater Sci.* 2004;39(16-17):5287-90.

[52]Mula S, Bahmanpour H, Mala S, Kang PC, Atwater M, Jian W, et al. Thermodynamic feasibility of solid solubility extension of Nb in Cu and their thermal stability. *Mater Sci Eng, A.* 2012;ACCEPTED.

[53]Zhang X, Vo NQ, Bellon P, Averback RS. Microstructural stability of nanostructured Cu–Nb–W alloys during high-temperature annealing and irradiation. *Acta Mater.* 2011;59(13):5332-41.

[54]Vo NQ, Chee SW, Schwen D, Zhang X, Bellon P, Averback RS. Microstructural stability of nanostructured Cu alloys during high-temperature irradiation. *Scripta Mater.* 2010;63(9):929-32.

[55]Liu F, Kirchheim R. Nano-scale grain growth inhibited by reducing grain boundary energy through solute segregation. *Journal of Crystal Growth.* 2004;264(1-3):385-91.

[56]Kirchheim R. Reducing grain boundary, dislocation line and vacancy formation energies by solute segregation. I. Theoretical background. *Acta Mater.* 2007;55(15):5129-38.

[57]Weissmuller J. Alloy thermodynamics in nanostructures. *J Mater Res.* 1994;9(1):4-7.

[58]Weissmuller J. Alloy effects in nanostructures. *Nanostruct Mater.* 1993;3(1-6):261-72.

- [59]Defay R, Prigogine I, Bellmans A, Everett DH. *Surface Tension and Adsorption*. New York, NY: Wiley; 1966.
- [60]McLean D. *Grain Boundaries in Metals*. London: Oxford Press; 1957.
- [61]Wynblatt P, Ku RC. Surface energy and solute strain energy effects in surface segregation. *Surf Sci*. 1977;65(2):511-31.
- [62]Wynblatt PW, Chatain D. Anisotropy of segregation at grain boundaries and surfaces. *Metall Mater Trans A*. 2006;37(9):2595-620.
- [63]Friedel J. Electronic structure of primary solid solutions in metals. *Adv Phys*. 1954;3(12):446-507.
- [64]VanLeeuwen BK, Darling KA, Liu Z-K, Koch CC, Scattergood RO. An approach to selecting grain boundary segregating solutes for stabilizing nanocrystalline alloys. *Acta Mater*. 2011;Submitted.
- [65]Darling KA, Chan RN, Wong PZ, Semones JE, Scattergood RO, Koch CC. Grain-size stabilization in nanocrystalline FeZr alloys. *Scripta Mater*. 2008;59(5): 530-3.
- [66]Darling KA, VanLeeuwen BK, Koch CC, Scattergood RO. Thermal stability of nanocrystalline Fe-Zr alloys. *Mater Sci Eng, A*. 2010;527(15):3572-80.
- [67]Darling KA, VanLeeuwen BK, Semones JE, Koch CC, Scattergood RO, Kecskesi LJ, et al. Stabilized nanocrystalline iron-based alloys: Guiding efforts in alloy selection. *Mater Sci Eng, A*. 2011;528(13-14):4365-71.
- [68]Kirchheim R. Grain coarsening inhibited by solute segregation. *Acta Mater*. 2002;50(2):413-9.

- [69]Kirchheim R. Reducing grain boundary, dislocation line and vacancy formation energies by solute segregation. II. Experimental evidence and consequences. *Acta Mater.* 2007;55(15):5139–48.
- [70]Millett PC, Selvam RP, Bansal S, Saxena A. Atomistic simulation of grain boundary energetics – effects of dopants. *Acta Mater.* 2005;53(13):3671-8.
- [71]Chen Z, Liu F, Wang HF, Yang W, Yang GC, Zhou YH. A thermokinetic description for grain growth in nanocrystalline materials. *Acta Mater.* 2009;57(5):1466-75
- [72]Lejcek P. *Grain Boundary Segregation in Metals.* 1 ed; 2010.
- [73]Li J, Wang J, Yang G. On the stagnation of grain growth in nanocrystalline materials. *Scripta Mater.* 2009;60(11):945-8.
- [74]Millett PC, Selvam RP, Saxena A. Molecular dynamics simulations of grain size stabilization in nanocrystalline materials by addition of dopants *Acta Mater.* 2006;54(2):297-303.
- [75]Seah MP. Segregation and the strength of grain boundaries. *Proc R Soc Lond A.* 1976;349(1659):535-54.
- [76]Meyers M, Chawla K. *Mechanical behavior of materials.* 2 ed. New York: Cambridge University Press 2009, p. 221.
- [77]Goldstein J, Newbury D, Joy D, Lyman C, Echlin P, Lifshin E, et al. *Scanning electron microscopy and x-ray analysis.* 3 ed. New York: Springer 2003, p. 427-36.
- [78]Williams DB, Carter CB. *Transmission electron microscopy: A textbook for materials science.* New York: Springer; 2009.

- [79]Lu L, Tao NR, Wang LB, Ding BZ, Lu K. Grain growth and strain release in nanocrystalline copper. *J Appl Phys.* 2001;89(11):3408-14.
- [80]Koch CC. Structural nanocrystalline materials: an overview *J Mater Sci.* 2007;42(5):1403-14.
- [81]Xu D, Lohwongwatana B, Duan G, Johnson WL, Garland C. Bulk metallic glass formation in binary Cu-rich alloy series – Cu<sub>100-x</sub>Zr<sub>x</sub> (x=34, 36, 38.2, 40 at.%) and mechanical properties of bulk Cu<sub>64</sub>Zr<sub>36</sub> glass. *Acta Mater.* 2004;52(9):2621–4.
- [82]Wang D, Li Y, Sun BB, Sui ML, Lu K, Ma E. Bulk metallic glass formation in the binary Cu-Zr system. *Appl Phys Lett.* 2004;84(20):4029-31.
- [83]Arnberg L, Backmark U, Backstrom N, Lange J. A new high strength, high conductivity Cu-0.5 wt.% Zr alloy produced by rapid solidification technology. *Materials Science and Engineering.* 1986;83(1):115-21.
- [84]Arias D, Abrilata JP. Cu-Zr (Copper-Zirconium). *Bull Alloy Phase Diagr.* 1990;11(5):452-9.
- [85]Okamoto H. Cu-Zr (Copper-Zirconium). *J Phase Equilib.* 2008;29(2):204.
- [86]deBoer FR, Boom R, Mattens WCM, Miedema AR, Niessen AK. Cohesion in metals: transition metal alloys. Amsterdam: Elsevier Scientific; 1988.
- [87]Turchanin MA, Porokhnya SV. Heat of formation of liquid copper alloys with 3d-transition metals. *Powder Metall Met Ceram.* 1996;35(7-8):378-88.
- [88]Abe T, Shimono M, Ode M, Onodera H. Thermodynamic modeling of the undercooled liquid in the Cu-Zr system. *Acta Mater.* 2006;54(4):909-15.

- [89]Zaitsev AI, Zaitseva NE. The thermodynamic properties of intermetallic compounds and solid solutions of Cu-Zr. *High Temp.* 2003;41(1):42-8.
- [90]Zhou SH, Napolitano RE. Phase stability for the Cu-Zr system: First principles, experiments and solution-based modeling. *Acta Mater.* 2010;58(6):2186-96
- [91]Kolyvanov EL, Koebelev NP, Estrin Y. Shear modulus and internal friction in a Cu-0.17% Zr alloy and pure copper subjected to equal-channel angular pressing. *Russ Metall.* 2010;2011(4):279-84.
- [92]Neishi K, Horita Z, Langdon TG. Achieving superplasticity in ultrafine-grained copper: influence of Zn and Zr additions. *Mater Sci Eng, A.* 2003;352(1-2):129-35.
- [93]Lou MY-W, Grant NJ. Identification of Cu<sub>5</sub>Zr Phase in Cu-Zr Alloys. *Metall Mater Trans A.* 1984;15 (7):1491-3.
- [94]Amouyal Y, Divinski SV, Estrin Y, Rabkin E. Short-circuit diffusion in an ultrafine-grained copper-zirconium alloy produced by equal channel angular pressing. *Acta Mater.* 2007;55(17):5968-79.
- [95]Saarivirta MJ. High conductivity copper-rich Cu-Zr alloys. *Trans Metall Soc AIME.* 1960;218(3):431-7.
- [96]Rajgarhia RK, Saxena A, Spearot DE, Hartwig KT, Moore KL, Kenik EA, et al. Microstructural stability of copper with antimony dopants at grain boundaries: experiments and molecular dynamics simulations. *J Mater Sci.* 2010;45(24):6707-18.
- [97]Seah MP. Grain boundary segregation. *J Phys F.* 1980;10(6):1043-64.

- [98]Azimi M, Akbari GH. Development of nano-structure Cu-Zr alloys by the mechanical alloying process. *J Alloys Compd.* 2011;509 (1):27-32.
- [99]Morris DG, Morris MA. Microstructure and strength of nanocrystalline copper alloy prepared by mechanical alloying *Acta Metall Mater.* 1991;39(8):1763-70.
- [100]Kowalski M, Spencer PJ. Thermodynamic Reevaluation of the Cu-Zn System. *J Phase Equilib.* 1993;14(4):432-8.
- [101]Oberg E, Jones FD, Horton HL, Ryffel HH. *Machinery's Handbook*. 26 ed. New York: Industrial Press Inc.; 2000.
- [102]Atwater MA, Scattergood RO, Koch CC. The stabilization of nanocrystalline copper by zirconium. *Mater Sci Eng, A.* 2012;SUBMITTED.
- [103]Feltham P, Copely CJ. Yielding and work hardening in alpha-brasses. *Acta Metall.* 1960;8(8):542–50.
- [104]Dalton WK. *The technology of metallurgy*. New York: Merrill; 1994.
- [105]Fisher JC. On the strength of solid solution alloys. *Acta Metall.* 1954;2(1):9-10.
- [106]Butt MZ, Ghaur IM. Effect of short-range order on the temperature dependence of plastic flow in  $\alpha$ -brasses. *Phys Status Solidi A.* 1988;107(1):187-95.
- [107]Reinhardt L, Schonfeld B, Kostorz G. Short-range order in  $\alpha$ -brass. *Phys Rev B.* 1990;41(4):1727-34.

- [108]Bahmanpour H, Youssef KM, Horky J, Setman D, Atwater MA, Zehetbauer MJ, et al. Deformation twins and related softening behavior in nanocrystalline Cu-30%Zn alloy. *Acta Mater.* 2012;SUBMITTED.
- [109]Nestorovic S, Markovic D, Markovic I. Influence of thermal cycling treatment on the anneal hardening effect of Cu-10Zn Alloy. *J Alloys Compd.* 2010;489(2):582-5.
- [110]Bader M, Eldis GT, Warlimont H. Mechanisms of Anneal Hardening in Cu-Al Alloys. *Metallurgical Transactions a-Physical Metallurgy and Materials Science.* 1976;7(2):249-55.
- [111]Sarma GMK, Ranganathan S. Changes in the Mechanical-Properties of an Alpha-Brass during Anneal-Hardening. *Zeitschrift Fur Metallkunde.* 1984;75(7):554-8.
- [112]Jia N, Zhao X, Song D, Zhou MH, Wang YD. On the anomalous hardening during annealing of heavily deformed f.c.c. metals. *Mater Sci Eng, A.* 2010;527(4-5):1143–50
- [113]Lu L, Chen X, Huang X, Lu K. Revealing the Maximum Strength in Nanotwinned Copper. *Science.* 2009;323(5914):607-10.
- [114]Lu L, Shen YF, Lu QH, Jin ZH, Lu K. Tensile properties of copper with nano-scale twins. *Scripta Mater.* 2005;52(10):989-94.
- [115]Youssef K, Sakaliyska M, Bahmanpour H, Scattergood R, Koch C. Effect of stacking fault energy on mechanical behavior of bulk nanocrystalline Cu and Cu alloys. *Acta Mater.* 2011;59(14):5758-64.

- [116]Sarma VS, Wang, J., Jian, W. W., Kauffmann, A., Conrad, H., Freudenberger, J., Zhu, Y. T. Role of stacking fault energy in strengthening due to cryo-deformation of FCC metals. Mater Sci Eng, A. 2010;527(29-30):7624-30.
- [117]Zhu YT, Liao XZ, Wu XL. Deformation twinning in nanocrystalline materials. Prog Mater Sci. 2012;57(1):1-62.
- [118]Wu XL, Zhu YT. Inverse Grain-Size Effect on Twinning in Nanocrystalline Ni. Phys Rev Lett. 2008;101(2):025503.
- [119]Zhang J-Y, Liu G, Wang RH, Li J, J.Sun, Ma E. Double-inverse grain size dependence of deformation twinning in nanocrystalline Cu. Phys Rev B. 2010;81(17):172104.
- [120]Miura H, Sakai T, Maruoka S, Jonas JJ. Production of recrystallized nano-grains in a fine-grained Cu-Zn alloy. Phil Mag Lett. 2010;90(2):93-101.
- [121]Saldana C, Murthy TG, Shankar MR, Stach EA, Chandrasekar S. Stabilizing nanostructured materials by coherent nanotwins and their grain boundary triple junction drag. Appl Phys Lett. 2009;94(2).
- [122]Mughrabi H, Hoppel HW, Kautz M, Valiev RZ. Annealing treatments to enhance thermal and mechanical stability of ultrafine-grained metals produced by severe plastic deformation. Z Metallkd. 2003;94(10):1079-83.
- [123]Gallagher PCJ. Influence of alloying, temperature, and related effectson stacking fault energy. Metall Trans. 1970;1(9):2429-61.
- [124]Krill CE, Ehrhardt H, Birringer R. Thermodynamic stabilization of nanocrystallinity. Z Metallkd. 2005;96(10):1134-41.

- [125] Dutkiewicz J. The Zn-Zr (Zinc-Zirconium) System. *J Phase Equilib.* 1992;13(4):430-3.
- [126] Okamoto H. Zn-Zr (Zinc-Zirconium) *J Phase Equilib Diffus.* 2007 28(2):236-7.
- [127] Williams ME, Boettinger WJ, Kattner UR. Contribution to the Zr-rich part of the Zn-Zr phase diagram. *J Phase Equilib Diffus.* 2004;25(4):355-63.
- [128] Rieger W, Nowotny H, Benesovsky F. Phasen mit oktaedrischen Bauelementen des Übergangsmetalls. *Montash Chem.* 1965;96(1):232-41.
- [129] Hofer G, Stadelmaier HH. Kobalt-, Nickel- und Kupfer-Phasen vom ternären MnCu<sub>2</sub>Al-Typ. *Montash Chem.* 1967;98(2):408-11.
- [130] Ganglberger E, Nowotny H, Benesovsky F. Neue G-Phasen. *Montash Chem.* 1966;97(3):829-32.
- [131] Arroyave R, Liu ZK. Thermodynamic modelling of the Zn-Zr system. *Calphad.* 2006;30(1):1-13.
- [132] Vitos L, Ruban AV, Skriver HL, Kollar J. The surface energy of metals. *Surf Sci.* 1998;411(1-2):186-202.
- [133] Rajgarhia RK, Spearot DE, Saxena A. Plastic deformation of nanocrystalline copper-antimony alloys. *J Mater Res.* 2010;25(3):411-21.
- [134] Rajgarhia RK, Spearot DE, Saxena A. Behavior of dopant-modified interfaces in metallic nanocrystalline materials. *JOM.* 2010;62(12):70-4.
- [135] Liu XJ, Wang CP, Ohnuma I, Kainuma R, Ishida K. Thermodynamic assessment of the phase diagrams of the Cu-Sb and Sb-Zn systems. *J Phase Equilib.* 2000;21(5):432-42.

- [136]Predel B, Gust W. Discontinuous precipitation processes in supersaturated copper-antimony solid solutions Metall Mater Trans A. 1975;6(6):1237-44.
- [137]Atwater MA, Bahmanpour H, Scattergood RO, Koch CC. Grain size stability of nanocrystalline copper 30% zinc alloy and the effect of zirconium addition. Mater Sci Eng, A. 2012;SUBMITTED.
- [138]Okamoto H. Sb-Zn (Antimony-Zinc) J Phase Equilib Diffus. 2008;29(3):290.
- [139]MSIT®, Bätzner C, Ferro R, Lebrun N, Perrot P, Rokhlin L, et al. Cu-Sb-Zn (Copper-Antimony-Zinc). In: Ilyenko GES, ed. Non-Ferrous Metal Ternary Systems Selected Copper Systems: Phase Diagrams, Crystallographic and Thermodynamic Data: Springer-Verlag 2007.
- [140]DeWitt B, Seltz H. A Thermodynamic Study of the Zinc-Antimony System. The Thermodynamic Properties of the Intermetallic Compounds: ZnSb, Zn<sub>3</sub>Sb<sub>2</sub> and Zn<sub>4</sub>Sb<sub>3</sub>. J Am Chem Soc. 1939;61(11):3170-3.
- [141]Miedema AR, Chatel PFd, Boer FRd. Cohesion in alloys - fundamentals of a semi-empirical model. Phys B+C. 1980;100(1):1-28.
- [142]Staley JT, Saxena A. Mechanisms of creep crack growth in 1 wt% antimony-copper: Implications for fracture parameters. Acta Metall Mater. 1990;38(6):897-908.
- [143]Inman MC, McLean D, Tipler HR. Interfacial free energy of copper-antimony alloys. Proc R Soc Lond A. 1963;273(1355):538-57.
- [144]Porter DA, Easterling KE. Phase transformations in metals and alloys. 2nd ed. London: Chapman Hall; 1992.

[145]Subramanian PR, Laughlin DE, eds. The Cu-W (Copper-Tungsten) System. Calcutta: Indian Institute of Metals 1991.

[146]Shewmon P. Diffusion in solids. 2 ed. Warrendale, PA: The Minerals, Metals & Materials Society; 1989.

[147]C.-S. Xiong, Y.-H. Xiong, H. Zhu, Sun T-F, E. Dong, Liu G-X. Synthesis and structural studies of the Cu-W alloys prepared by mechanical alloying. *Nanostruct Mater*. 1995;5(4):425-32.

[148]Raghu T, Sundaresan R, Ramakrishnan P, Mohan TRR. Synthesis of nanocrystalline copper-tungsten alloys by mechanical alloying. *Mater Sci Eng, A*. 2001;304-306:438-41.

[149]Gaffet E, Louison C, Harmelin M, Faudot F. Metastable phase transformations induced by ball-milling in the Cu-W system. *Mater Sci Eng, A*. 1991;134(1):1380-4.

[150]Zhang DL. Processing of advanced materials using high-energy mechanical milling. *Prog Mater Sci*. 2004;49(3-4):537-60.

[151]Sabirov I, Pippan R. Formation of a W-25%Cu nanocomposite during high pressure torsion. *Scripta Mater*. 2005;52(12):1293-8.

[152]Pippan R, Scheriau S, Taylor A, Hafok M, Hohenwarter A, Bachmaier A. Saturation of fragmentation during severe plastic deformation. *Ann Rev Mater Res*. 2010;40:319-43.

[153]Hong S-H, Kim B-K, Munir ZA. Synthesis and consolidation of nanostructured W-10-40 wt.% Cu powders. *Mater Sci Eng, A*. 2005;405(1-2):325-32.

[154]Lee SH, Li X. Study of the surface integrity of the machined workpiece in the EDM of tungsten carbide. *J Mater Process Tech*. 2003;139(1-3):315-21.